# OPTIMIZATION AND EVALUATION OF VEHICLE DYNAMICS AND POWERTRAIN OPERATION FOR CONNECTED AND AUTONOMOUS VEHICLES

A DISSERTATION
SUBMITTED TO THE FACULTY OF THE
UNIVERSITY OF MINNESOTA
BY

Yunli Shao

IN PARTIAL FULFILLMENT OF THE REQUIERMENTS
FOR THE DEGREE OF
DOCTOR OF PHILOSOPHY

Professor Zongxuan Sun, Advisor

November, 2019

# Acknowledgements

First and foremost, I would like to express my deepest gratitude to my advisor, Professor Zongxuan Sun. In my view, he is the best advisor I could ever have. His guidance and support are throughout all aspects of how to become an outstanding researcher: technical capabilities on research, invaluable non-technical skills, and work-life balance. I was most beneficial from his insightful and strategic vision of the research direction, his sharp and thoughtful advice on specific research, and his passion, dedication and consistency on pursuing the highest-standard research outcomes. His inspiration and influence on me are beyond what have been made over the past years, and will be a treasure for a lifelong time.

Second, I would like to thank all professors served on my preliminary and/or defense committee: Professor Kim Stelson, Professor Rajesh Rajamani, Professor Michael Levin, and Professor John Hourdos, for their helpful suggestions and critical feedback to my research and their instrumental guidance and supports.

Besides, I would like to thank my collaborators: Professor Jia Hu from Tongji University, Dr. Peter Huang and Dr. Joe Bared from Federal Highway Administration (FHWA), and Professor Meng Wang from Delft University, for their insightful comments and constructive suggestions that have encouraged me over the years.

Also, I would like to thank all current and previous members from our research group. They are always willing to help and discuss, and I learned a lot from all these smart minds. I would also like to thank all my friends who have supported and helped me over the years.

Last but not the least, I would like to thank my family, especially my parent and my wife. I feel grateful and fortunate to have them with me. Their love and support are always the motivation and encouragement in my life.

This research was supported by the Federal Highway Administration (FHWA) under grant DTFH6114H00005 and under contract DTFH6117P00009, and by the University of Minnesota Doctoral Dissertation Fellowship (DDF).

*To my family*

## Abstract

Recently, connected and autonomous vehicle (CAV) technology is gaining attentions around the world. A connected vehicle (CV) is equipped with sensors to collect real-time vehicle data and communication devices to 'talk' with other surrounding vehicles and/or infrastructures (such as traffic signals). With the communication capability, a CV can obtain real-time traffic information that was not available today, such as preceding vehicles' speeds, locations, and signal phase and timing (SPaT). This newly available information enables a CV to anticipate future driving conditions. With partial or full vehicle automation, the vehicle's motion (acceleration, speed, etc.) can be controlled in real-time. With both connectivity and automation, the vehicle can respond to traffic conditions proactively and operate in the most energy efficient manner. This is achieved by an effective prediction of future driving conditions enabled by connectivity and being able to plan and adapt vehicle speed and powertrain operation in a more flexible and optimal fashion enabled by the vehicle automation. The target CAV can accelerate and decelerate smoothly, avoid unnecessary braking and idling, and operate the powertrain system more efficiently.

This dissertation aims to explore the potential of energy savings through vehicle automation and connectivity. Real-time implementable optimal control strategies are developed for energy savings of CAVs with three most common powertrain types today: internal combustion engine based vehicles (ICVs), hybrid electric vehicles (HEVs), and electric vehicles (EVs). Both the vehicle speed trajectory and powertrain operation (e.g. transmission gear position or engine-battery power-split) are optimized to maximize the energy benefits. The optimization is designed for each specific powertrain type considering impacts of powertrain operation, constraints and dynamics on the energy consumption. This ensures the optimal control law is realistic and can be potentially implemented on an actual vehicle. A systematic control framework, which combines both traffic prediction and energy optimization, is developed to implement the optimal control in the model predictive control (MPC) fashion. The traffic prediction method can be applied to scenarios where both connected and non-connected vehicles are on the road. A traffic flow model is used to describe dynamics of the traffic states (traffic density and

traffic speed). Current traffic states are estimated using an observer based on real-time information communicated from connected vehicles and signal lights. Future traffic states can be predicted by propagating the traffic flow model forward in time. Uncertainties in the traffic prediction are systematically quantified and considered during the optimization to ensure the performance of the optimal control.

To experimentally validate the optimal control strategies, a hardware-in-the-loop (HIL) testbed developed previously in our group has been enhanced. The HIL testbed has an actual engine loaded by a hydrostatic dynamometer and emulates a virtual target vehicle with simulated vehicle dynamics. To increase the fidelity of the testbed, the same type of engine as the actual vehicle is installed and both vehicle and powertrain models are calibrated using actual vehicle testing data. The resulting HIL testbed matches well with the performance of the actual testing vehicle with only about 1% error. In addition, a living lab is developed with instrumented on-road testing vehicles and intersection at TH55 in Minnesota. This brings in real-world traffic data and enables the HIL testbed to interact with real traffic. The results significantly improve the credibility of the HIL testbed. The inclusion of real-world traffic information extends the capabilities of the HIL testbed to evaluate the real-time capability and robustness of various CAV applications in realistic roadway conditions.

For ICVs, the optimal control problem is a hybrid one with both continuous (vehicle speed, braking force) and discrete (gear position) control inputs. The problem is formulated and simplified to a mixed integer programming problem with a convex quadratic objective function and linear constraints. The optimal control solutions are obtained in real-time using an efficient numerical solver. Two traffic scenarios are studied in both simulation and experiment: 1) a rolling terrain scenario without a nearby preceding vehicle. The target vehicle anticipates the future roadway slopes and cruises with the optimal speed and gear position. The results have shown that the fuel benefit is 16.1% compared to a baseline vehicle using constant speed cruising control. 2) a vehicle platooning scenario on a signalized urban road. The target vehicle is at the end of a vehicle platoon and follows the preceding vehicle. The target vehicle can achieve 10.6% fuel benefits compared to the immediate preceding vehicle.

For HEVs, the vehicle speed and powertrain operation optimization algorithms are developed and solved in a consecutive order. The vehicle level optimization solves an optimal vehicle speed trajectory. The optimal speed profile is then sent to the powertrain controller to optimize both engine operating points and the power-split (engine power vs battery power). Again, the control is evaluated in both a rolling terrain scenario and an urban driving scenario. In the rolling terrain scenario, the energy benefits from the proposed optimal controller are 5.0% to 8.9% on major arterials and 15.7% to 16.9% on collector roads, compared to a regular HEV cruising at constant speed. In the urban driving scenario, the target vehicle can achieve 17.3% fuel benefit with vehicle level optimization alone. With both vehicle and powertrain optimization, the fuel benefit is 22.8% comparing to the preceding vehicle.

For EVs, the efficiencies of the electrical powertrain (including the electric motor, battery, etc.) are considered during the vehicle speed trajectory optimization. The battery aging effects are considered to ensure a satisfactory battery life and several regenerative braking constraints are included to make the optimal control strategy realistic for practical implementation. The optimal control strategy is evaluated in a vehicle platooning scenario on a signalized roadway with two intersections. For a vehicle platoon of 16 vehicles, with 50% penetration rate of connectivity, the target vehicle can achieve 9.1% energy improvement. The performance is satisfactory compared to the 14.3% energy saving with perfect traffic prediction. This demonstrates the effectiveness of the proposed optimization method.

# Table of Contents

# List of Tables

# List of Figures

# Chapter 1

# Introduction

## 1.1. Motivations

Transportation sector accounts for about 30 percent of greenhouse gas emissions in the United States [1] and for 26 percent of the total energy consumption worldwide [2]. There have been increasing concerns about its impact on the environment and human health. Reducing emissions and improving the energy efficiency of the transportation sector have become a challenging and urgent issue. From 1980 to 2014, the averaged mile per gallon (MPG) of a light-duty passenger vehicle has increased by about 50% [3]. Vehicles have become more efficient with many technologies that have improved aerodynamic design, reduced vehicle weight, and increased powertrain efficiency (e.g. direct injection, variable valve timing, turbochargers and superchargers). Recently, connected and autonomous vehicle (CAV) technology is gaining attentions around the world. This dissertation aims to explore the potential of energy savings through vehicle automation and connectivity.

A connected vehicle (CV) is equipped with sensors to collect real-time vehicle data and communication devices to 'talk' with other surrounding vehicles, through vehicle-to-vehicle (V2V) communication, and infrastructures (such as traffic signals), through vehicle-to-infrastructure (V2I) communication. With the communication capability, a CV can obtain real-time traffic information that was not available today, such as preceding vehicles' speeds, locations, and signal phase and timing (SPaT). This newly available information enables a CV to anticipate future driving conditions. With partial or full vehicle automation, the vehicle's motion (acceleration, speed, etc.) can be controlled in real-time. With both connectivity and automation, the vehicle can respond to traffic conditions proactively and operate in the most energy efficient manner. This is

achieved by an effective prediction of future driving conditions enabled by connectivity and being able to plan and adapt vehicle speed and powertrain operation in a more flexible and optimal fashion enabled by the vehicle automation. The target CAV can accelerate and decelerate smoothly, avoid unnecessary braking and idling, and operate the powertrain system more efficiently. There are many emerging CAV applications for energy savings [4] such as eco-approach and departure (Eco-AD), eco-cooperative adaptive cruise control (Eco-CACC), and eco-routing. It is complicated to develop such CAV applications as it involves many aspects including communication/perception, optimization, prediction, implementation, and evaluation. There needs studies on developing systematic approaches for solving this complex problem.

## 1.2. Vehicle Dynamics and Powertrain Operation Optimization for CAVs

In CAV applications, energy efficiency can be improved at two levels [5]: vehicle level and powertrain level. Co-optimization of both levels offers the maximum potential for energy savings. At the vehicle level, based on predicted future driving conditions, the target CAV can adjust its vehicle speed and car-following distance to operate with the most energy efficient vehicle power demand. At the powertrain level, for the same power demand, the powertrain system can be operated in the most efficient regions. The optimal control strategy is different for vehicles of different powertrain architectures as energy consumption depends on both the vehicle states (e.g. vehicle speed, acceleration) and the powertrain states (e.g. engine speed and torque or electric motor speed and torque). The most energy efficient control strategy can be obtained by solving a model-based optimal control problem with the objective to minimize the energy consumption while maintaining satisfactory mobility and driving comfort. For vehicles of different powertrain types, the specific powertrain model, powertrain operation control means, and energy consumption model are different. But the vehicle longitudinal dynamics, vehicle state equations and traffic constraints (e.g. safe car-following distance constraint or pass

the intersection only on green light) remain the same. Currently, most literature on CAV applications focuses on the vehicle level optimization only [6–9]. During the optimization, the effects of powertrain operation and powertrain constraints on the energy consumption are either greatly simplified or neglected. Without considering the characteristics and dynamics of different powertrain types, the resulting optimal control strategies might not be realistic for implementation and energy savings may not be maximized. There lacks a systematic study on vehicle dynamics and powertrain operation co-optimization for vehicles of different powertrain types.

### 1.2.1. Internal Combustion Engine Based Vehicles (ICVs)

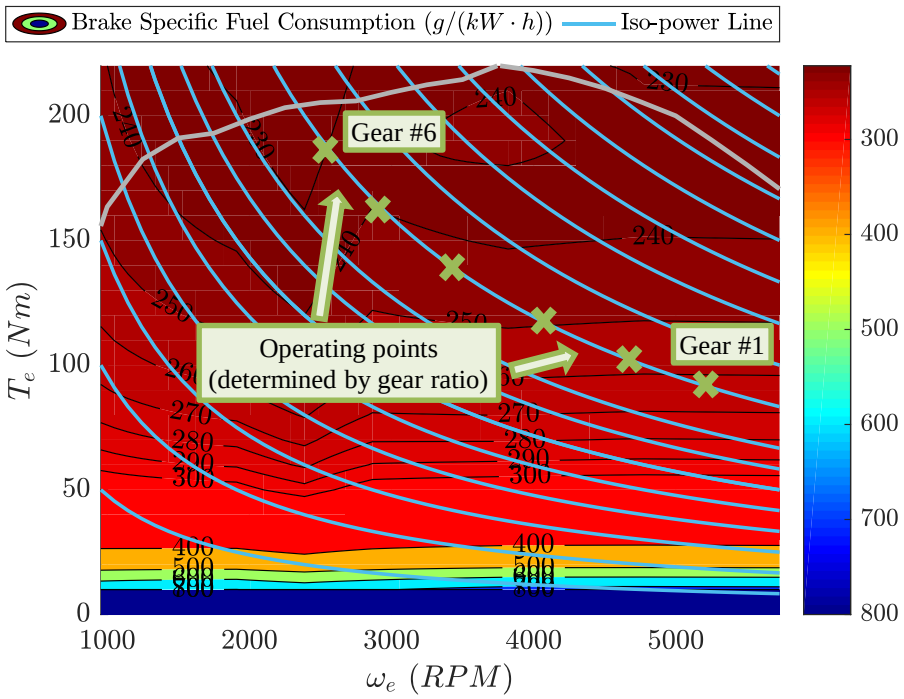


Figure 1.1 Brake specific fuel consumption (BSFC) map of an engine.

For an ICV, which is still today's most common type of passenger or commercial vehicle, both the vehicle speed and the transmission gear position can be optimized to maximize energy benefits. Figure 1.1 shows the brake specific fuel consumption (BSFC)

contours of a typical internal combustion (IC) engine. BSFC measures how many grams of fuel the engine will consume per hour to generate one unit of power. A smaller BSFC means a more efficient operating condition. The blue curves are iso-power lines. The vehicle power request is the same on each blue curve. For a given vehicle power request, the engine operating points are determined by the gear ratio and usually it is more efficient to operate the engine at a higher gear position. The engine will thus be operated around high efficiency regions (usually low speed and high torque regions near the maximum engine torque line). It is preferable to keep the engine operating points in these regions if considering fuel economy alone. However, these high efficiency regions are not always favorable if considering drivability criteria such as satisfying acceleration requirement and avoiding shift busyness [10]. When operating the engine near the maximum torque line, a downshift may be needed before responding to an increased vehicle power demand. This is a slower process and can cause an engine lugging feeling. Also, frequent gear shifts may occur (known as shift busyness) if keeping operating the powertrain system around the most energy-efficient regions. Today, the transmission gear position is usually determined by a fixed gear shift schedule [10,11] which is developed through calibrations to balance the energy efficiency and drivability. Hysteresis rules are calibrated to separate upshift points and downshift points to avoid shift busyness. The fixed gear shift schedule is conservative and is calibrated to satisfy the most demanding performance requirement. In normal driving conditions, the engine will operate on partial load conditions and the operating points may be away from the most efficient regions (known as torque/power reserve [10]) and this can sacrifice energy efficiency. With connectivity, a CAV can anticipate future driving conditions and intelligently adapt the gear shift to reduce unnecessary torque reserves. For example, a CAV can shift to higher gears and operate the engine in more efficient regions if it is anticipated that the target vehicle will be cruising in the future (power demand will be low).

### 1.2.2. Hybrid Electric Vehicles (HEVs)

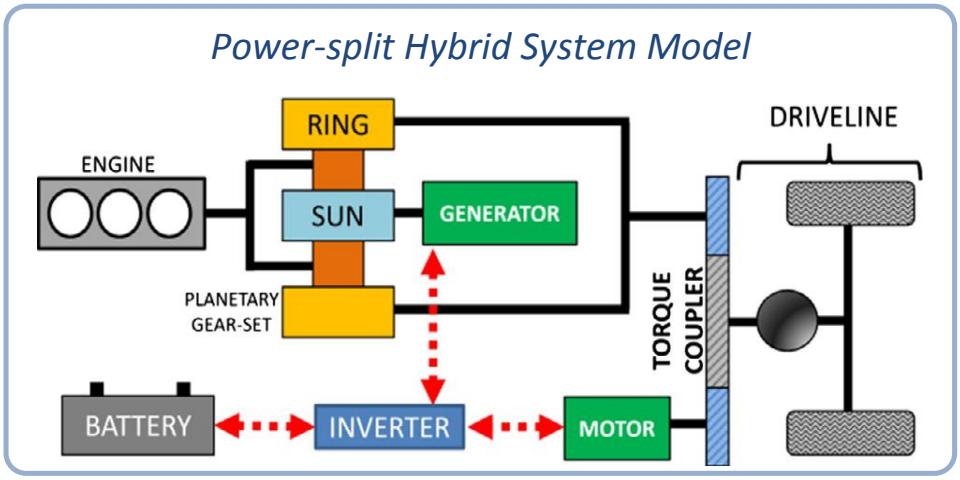


Figure 1.2 Power-split hybrid electric vehicle powertrain architecture.

For HEVs, an alternative power source (battery) is equipped and works together with the engine to provide the power needed for driving. With this additional degree of freedom, the engine and the battery can operate at different power output to achieve the same vehicle power request. Both the vehicle speed and the power split between the engine and the battery can be optimized to maximize the energy efficiency. There are different architectures of HEVs including [11]: series HEVs, parallel HEVs and power-split HEVs. In this dissertation, the power-split HEV is studied (a typical architecture is shown in Figure 1.2). Power-split HEVs are also known as series-parallel HEVs and combines the advantages of both the series and parallel HEVs. A planetary gear set is used to split the engine power into two parts. Part of the power is used to propel the driveline directly, and the other part goes through the electrical path to the driveline. With the specific mechanical architecture of the planetary gear set and the alternative electric power source, the engine operating condition can be independently controlled from the vehicle power demand. To fully realize the energy saving potentials

of HEVs, the power management control of the hybrid powertrain must be carefully designed.

The current HEVs in the market usually employ heuristic or ad-hoc power management strategies which may not be optimal under a real driving scenario. These strategies use the electrical power source conservatively to prevent depleting the battery. The 'best' power-split ratio can be determined if the future vehicle speed trajectory and vehicle power demand can be anticipated a priori. This becomes feasible with the real-time traffic information from the connectivity and the vehicle speed control enabled by automation. The optimal controller can thus anticipate the upcoming vehicle speed trajectories and then select the appropriate power split intelligently. For example, when approaching an intersection, if the vehicle knows the traffic signal will turn red shortly and a stop is necessary, the controller can choose to use more electrical power to drive the vehicle approaching the intersection. This way, the engine will work less hence use less fuel, while the battery will be replenished through regenerative braking when the vehicle decelerates to a stop.

### 1.2.3. Electric Vehicles (EVs)

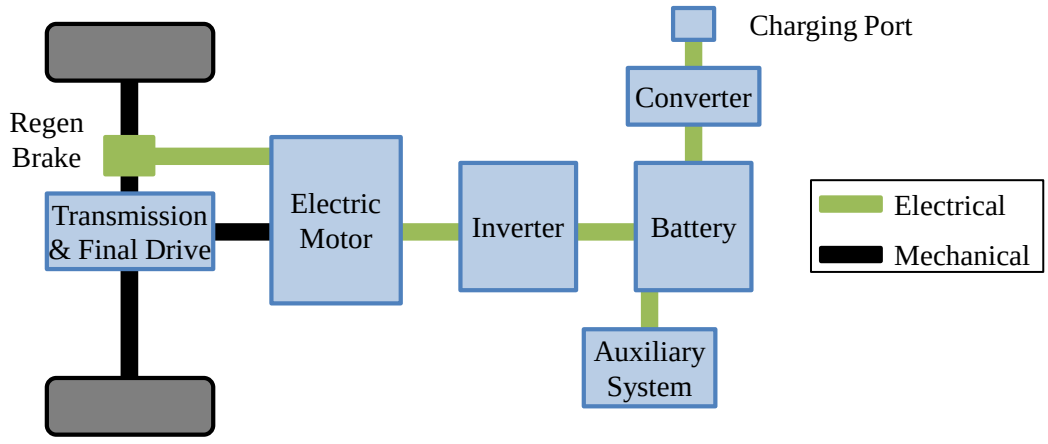


Figure 1.3 Architecture of a typical battery electric vehicle.

Recently, EVs have become more popular in both the market and academia research due to the advancement of battery and power electronics technologies, and the stricter regulations on energy efficiency and emissions. A typical mass production EV is propelled by an AC electric motor (EM) with a battery pack and a DC\AC inverter, as shown in Figure 1.3. The output shaft of the motor is mechanically connected to the vehicle wheels through a gearbox (transmission) and a final drive with a fixed gear ratio. The vehicle speed and traction force are directly linked to the motor speed and torque of the EM. The energy savings for an EV can be obtained by optimizing the vehicle speed to reduce power demand and operate the EM at more efficient operating points. Comparing to IC engines, EMs generally have higher efficiencies. But the efficiency losses still depend on the operating conditions of the EMs (such as current, rotational speed and loads). The battery efficiency depends on the operating conditions as well (such as current, state-of-charge, temperature). In addition, EVs are usually equipped with both frictional braking and regenerative braking for deceleration. With regenerative braking, part of the kinetic energy can be converted to electrical energy rather than wasted to heat. With connectivity and automation, a target EV can schedule the vehicle speed intelligently considering the electric powertrain efficiency (including the EM, battery, etc.) and regenerative braking, hence reduces losses of the powertrain and avoids wastes of kinetic energy from frictional braking.

## 1.3. Traffic Prediction using Information from Connectivity

During a CAV application, there are usually several traffic constraints that need to be satisfied. These constraints usually require the knowledge of future traffic conditions. For example, when following a preceding vehicle, the target CAV has to adjust its car-following distance between a minimum and maximum bound to avoid collision and negative impacts to vehicles behind. This car-following distance constraint depends on the knowledge of the preceding vehicle's future trajectories. Also, on a signalized

roadway, the vehicle is constrained by the traffic signal and can only pass the intersection during green lights. This requires knowledge of future signal phase and timing. The above examples show that prediction of future driving conditions essentially determines the constraints of the energy optimization problem. Due to the inter-connection between traffic prediction and energy optimization, it is crucial to develop a reliable prediction approach. An inaccurate traffic prediction can deteriorate energy savings or cause safety concerns [12–14]. The prediction of future traffic conditions becomes feasible using the real-time information enabled by connectivity.

It is challenging to develop a precise short-term traffic prediction for the next 10-15 seconds and for 300-500 meters (typical range of communication). The prediction of driver's behaviors [15] may be reasonable for the next second or two, but it is difficult to predict next 10-15 seconds. Fundamentally, even an individual vehicle is controlled by the driver, the driver's action is significantly constrained by the traffic dynamics in front. For example, at a red signal light, every driver has to follow the rule and decelerate to a stop. Therefore, prediction of traffic is crucial to determine individual vehicle's motion. In literature, most traffic prediction approaches focus on the modeling of traffic states (traffic flow and traffic density) for next several minutes and for a roadway of several kilometers. This is because typically, traffic prediction is of interest for traffic operations and planning. Examples include ramp metering at highway or advanced signal control at urban roads. Several researchers have developed CAV applications based on prediction of queue length [12,16] at intersections. However, researchers usually assume all vehicles are CVs. It is challenging to apply these methods for mixed traffic scenarios where both connected vehicles CVs and non-CVs share the road. Without knowing the numbers and locations of all vehicles on the road, it is difficult to estimate the formulation and dissipation of the queue.

Generally, traffic modeling methods can be divided into three types: car-following models, data-driven models, and traffic flow models. Car-following models have been

widely used in traffic simulation software [17]. Several researchers have used these models to predict future traffic for 100% CV penetration rate scenarios [18,19]. It is challenging to apply car-following models in a mixed traffic scenario since the number of non-CVs in front of the target vehicle is unknown. Data-driven models are derived based on traffic data rather than physical behaviors of the traffic. These models have gained lots of attention due to their flexibility and ease-of-use [20–22]. Data-driven models usually perform well for scenarios within their calibration dataset (or training set). But they may fail for scenarios that are outside of the training set or with uncertainties. It is also difficult to interpret these models and gain physical insights from the model structures or parameters. A potential solution is to consider the entire traffic dynamics as continuum fluid using traffic flow models. These models are derived based on physical traffic behaviors and have the potential to perform traffic prediction for scenarios with even low penetration rates of connectivity. Flow models include first-order models (Lighthill–Whitham–Richards (LWR) model) [23,24] and second-order models [25,26]. First-order models assume a one-to-one relationship between traffic speed and traffic density (veh/meter) determined by a fundamental diagram. Second-order models use an additional equation to describe the traffic speed dynamics that are not at the equilibrium in the fundamental diagram. Flow models have been widely used by researchers to estimate traffic performance (in quantity of traffic density or traffic flow). Usually, traffic flow measured from loop detectors can be used as feedback to correct the traffic estimation. With CVs, individual vehicle's trajectory becomes available and can be used as additional feedback. Researchers have investigated using probing vehicles' data to estimate traffic flow and density [27,28]. In these works, the traffic prediction horizon is typically in the unit of minutes and the roadway of interest is usually a corridor of several kilometers. This is different than the requirement of CAV applications where a short-term traffic prediction, typically 10-15 seconds, is of interest, and the roadway of interest is

300-500 meters. It is unclear how well these flow models will perform for predicting individual vehicle's trajectory.

### 1.4. Real-time Optimal Control for CAVs

Since the traffic conditions are highly dynamic, the optimal control strategy needs to be real-time solvable and implemented together with the traffic prediction. The control strategy needs to be recalculated as the target vehicle getting new information from the preceding CVs and signal lights, and updating the prediction of future driving conditions. It is challenging since the energy consumption model, vehicle model, and powertrain model are usually nonlinear and complex, and depend on both vehicle states and powertrain states. Traffic constraints (e.g. car-following distance bounds) are essentially state constraints which bring in additional complexities to the optimal control problem. The controller should be robust to maintain a satisfactory performance even with traffic prediction uncertainties. For control strategies developed from pre-calculated (offline) or historical data, it is difficult to ensure a safe car-following distance as the actual traffic conditions can be significantly different from the data. The optimal control problem can be simplified using rule-based control strategies [16,29] but energy benefits are not maximized. Some researchers attempted to either simplify or neglect the effects of powertrain states on the energy consumption to simplify the problem [6,18,30]. These assumptions may not hold since powertrain states will significantly affect the energy efficiency. The optimal vehicle speed is different for vehicles of different powertrain architectures due to their different energy consumption models (depends on powertrain states) and different powertrain constraints. The computational burden of the optimal control problem usually depends on the size of the system states and inputs, how nonlinear the system is, the number of constraints and their complexities, and whether there are discrete variables or state switching. The computational cost can often be

reduced significantly through an alternative problem formulation or a better selection of optimization variables.

There are generally two approaches [31] to solve the optimal control problem in real-time: indirect methods and direct methods. Dynamic programming (DP) is another solving method but generally it is not suitable for real-time application due to the computational burden. Indirect methods are based on the calculus of variations and the Pontryagin's minimum principle (PMP). PMP gives optimality conditions for the original optimal control problem to formulate a boundary-value problem (BVP). The BVP consists of differential equations that satisfy initial point, end point and interior point constraints (if any). The optimal control can be obtained by solving the BVP. For direct methods, the original optimal control problem is first discretized and transformed to a nonlinear programming (NLP) problem. All the state equations and boundary conditions are converted as constraints and are satisfied at each discretization point. Then the optimality conditions are developed and the NLP is solved using efficient NLP solvers (such as [32–35]). The indirect and direct methods are essentially 'commutative' by the virtue of 'Covector Mapping Theorem' [31,36]. Essentially, the solution to the optimality conditions for the discretized problem (from direct method) approximately satisfies the optimality conditions for the continuous problem (from indirect method). The indirect method is usually more effective for problems without complex constraints. An advantage is that sometimes analytical solutions can be found using the PMP necessary conditions (a classical example is the linear quadratic regulator (LQR) problem). For nonlinear systems, the differential equations may not be able to be solved analytically. For problems with state path constraints, the optimal control may switch on several arcs as the constraints become active/inactive. This makes the PMP analysis more complex [37]. It is not trivial to numerically solve the BVPs due to the unknown initial values of co-states and limited numerical tools. For direct method, the NLP solvers are more mature and computationally efficient by taking advantage of the sparsity of the

discretized problem. State trajectories and optimal controls are solved straightforwardly and there is no need to derive the optimality conditions. It is flexible and relatively easy to modify and adapt the optimal control problem.

## 1.5. Evaluation of CAV Applications for Energy Savings

Once the optimal control strategies are developed, it is not trivial to evaluate the effectiveness and energy benefits of these controllers. There are many technical challenges. Interacting with other vehicles in real-world traffic scenarios may cause safety concerns. It can be time-consuming and expensive to instrument a testing vehicle as it may require major modifications of the vehicle [38,39]. In addition, it is challenging to equip precise energy consumption and emissions instruments on a passenger vehicle considering their sizes. Therefore, most studies on energy focused CAV applications were conducted in simulations [40–43]. A simulation-based approach evaluates the performance of a virtual CAV that interacts with other virtual vehicles and infrastructures in a simulated traffic network. There is no real traffic information involved and the actual powertrain dynamics of the vehicle is replaced with steady-state energy consumption and emission maps. These steady-state maps may be inaccurate during powertrain transients [44,45] and it is difficult to model emissions such as nitrogen oxides and soot accurately [46,47]. Several researchers have investigated hardware-in-the-loop (HIL) simulations to allow an actual testing vehicle to interact with simulated traffic [48,49]. However, to avoid safety concerns, these HIL experiments don’t allow interactions between the actual testing vehicle and the real traffic, and are limited to proving grounds. There lacks a systematic evaluation approach for CAV applications that is economic, effective and without safety concerns.

## 1.6. Contributions of the Dissertation

Enlighted by the current state-of-the-art research on CAV applications for energy savings, this dissertation aims to develop real-time implementable optimal control that integrates traffic prediction with vehicle speed trajectory and powertrain operation optimization for energy savings of CAVs with different powertrain types. Then a safe, economic, and effective experimental evaluation platform is developed and enhanced to validate the optimal controller. The contributions are:

1. *Development of a systematic control framework that combines traffic prediction and energy optimization for CAVs* [13]. The control is implemented in the MPC fashion and updated when new traffic information is available. Prediction uncertainties are considered during the optimization to ensure robust performance and to satisfy constraints. The traffic prediction method can be applied to mixed traffic scenarios where both CVs and non-CVs are on the road.
2. *Development and evaluation of real-time vehicle dynamics and powertrain operation optimization for different types of vehicles (ICVs* [13,50–52]*, HEVs* [5,7] *and EVs* [53]*) and CAV applications.* Different optimal control strategies are designed considering the characteristics of specific powertrain types and the effects of powertrain operation on energy consumption. The control strategies are evaluated for different traffic scenarios: with or without nearby preceding vehicles, urban drive on signalized intersections or free speed cruising, flat roadways or hilly roadways. Significant energy savings (10-20%) have been shown in experiment and/or simulation with the co-optimization.
3. *Development of a living lab and enhancement of a HIL testbed to provide a safe, effective, and economical platform for evaluating CAVs* [54,55]. The HIL testbed has an actual engine loaded by a hydrostatic dynamometer and emulates a virtual target vehicle with simulated vehicle dynamics. The same engine as the actual testing vehicle

is installed and the vehicle models are calibrated using testing data from the actual vehicle. The performance of the target vehicle (HIL testbed) can thus match the actual testing vehicle at FHWA with about 1% error [54]. The living lab brings in real traffic information through communication with instrumented on-road testing vehicles and intersection at TH55 in Minnesota (with support from MnDOT). The HIL testbed can thus evaluate the performance of a target CAV that follows an on-road testing vehicle driven on real-world roadway conditions to evaluate different CAV applications.

## 1.7. Overview of the Dissertation

The dissertation is organized as follows:

**Chapter 2 Optimal Control Framework:** In this chapter, the overall control framework is presented. The optimal vehicle dynamics and powertrain operation control strategies are solved and implemented with a traffic prediction (based on traffic flow theory) to provide a complete solution to CAV applications for energy savings. Essentially, prediction of future traffic conditions determines traffic constraints (e.g. car-following distance constraint) of the optimization problem. This control framework is in the model predictive control (MPC) fashion and is applied to vehicles of different powertrain types in the following chapters.

**Chapter 3 Optimization for Internal Combustion Engine Based Vehicles:** In this chapter, a real-time implementable optimal control method is developed to solve optimal vehicle speed trajectory and gear position simultaneously while maximizing both energy efficiency and drivability. The optimization problem is formulated and carefully simplified to a mixed integer programming with a convex quadratic objective function and linear constraints without sacrificing the accuracy. The problem is then discretized using the pseudo-spectral method and solved by an efficient state-of-the-art mixed-integer solver. The optimal control is evaluated for two traffic scenarios: a rolling terrain scenario where the target vehicle is not following a nearby preceding vehicle, and

a vehicle platooning scenario on a signalized urban roadway. Significant fuel reductions, 10.6%-16.1% have been demonstrated in both simulation and experiment (using the hardware-in-the-loop testbed presented in Chapter 6).

**Chapter 4 Optimization for Hybrid Electric Vehicles:** This chapter presents a real-time vehicle dynamics and powertrain operation co-optimization controller for hybrid electric vehicles. The controller determines optimal vehicle speed trajectory, engine-battery power-split and engine operating point all together to maximize the energy savings. The problem was solved using Pontryagin's minimum principle and nonlinear programming. Efforts were made to reduce the computational burden of the optimization process so that it can be solved in real-time. The optimal control is evaluated in two scenarios in simulation and 5%-23% energy benefits are obtained: 1) a rolling terrain scenario with no nearby preceding vehicle; 2) an eco-approach scenario where the target vehicle follows a preceding vehicle to pass an intersection. The eco-approach scenario is based on real-world traffic data collected from instrumented testing vehicle and real-world intersection using the living lab presented in Chapter 6.

**Chapter 5 Optimization for Battery Electric Vehicles:** This chapter develops a real-time vehicle speed trajectory optimization for connected and autonomous EVs considering battery aging effects and realistic regenerative braking constraints. The target vehicle intelligently controls the vehicle speed and car-following distance based on predicted traffic conditions using real-time information enabled by connectivity. The optimal control problem is formulated with carefully selected optimization variables. Then the problem is simplified and discretized without sacrificing the accuracy and is solved by a state-of-the-art numerical solver. The control is evaluated in simulation for a traffic scenario where the target vehicle follows a vehicle platoon to pass a signalized roadway, and 9.1%-14.3% energy benefits are achieved.

**Chapter 6 Evaluating Connected and Autonomous Vehicles Using a Hardware-in-the-loop Testbed and a Living Lab:** The hardware-in-the-loop (HIL)

testbed has an actual engine loaded by a hydrostatic dynamometer whose loading torque is controlled in real-time based on the simulated vehicle dynamics. The HIL testbed emulates the performance of a target vehicle and the dynamometer generates the same load as the target vehicle. The same engine as the actual testing vehicle was installed and the vehicle models were calibrated using testing data from the actual vehicle. The results have shown that the performance of the HIL testbed matches very well with the actual testing vehicles with about 1% error. In addition, a living lab is developed with instrumented vehicles and signalized roadway to enable the HIL testbed to interact with real-world traffic and extend the testing capabilities of the HIL testbed. The HIL testbed could provide an effective and economical way for the testing of fuel consumption and emissions on various roadway conditions for CAVs and other types of vehicles.

**Chapter 7 Conclusion and Future Work:** This chapter concludes the dissertation and discusses potential future work.

# Chapter 2

# Optimal Control Framework

In this chapter, the overall control framework is presented. As discussed in Chapter 1, the optimal control can be determined based on predicted future traffic conditions using real-time information from other CVs and signal lights. It is complicated to integrate the traffic prediction with the energy optimization. Many existing researches on CAV energy optimization assume known future traffic conditions, such as in [6,56–60]. There are several studies that consider queue length or signal information during the energy optimization [12,16], but they did not explicitly consider traffic prediction or realistic car-following distance constraints. Very few researchers developed energy optimization with traffic prediction [18,19]. They typically use car-following models and assume all vehicles on the road are connected vehicles (100% penetration rate). Meanwhile, the existing literatures on traffic prediction mostly focus on estimating the traffic states for optimizing traffic operations and planning [20,27,61,62], rather than energy optimization of individual vehicles. There is a need for a systematic and comprehensive study on integrating real-time traffic prediction and energy optimization for connected and autonomous vehicles, which is the focus of this chapter.

In the proposed control framework, the optimal vehicle dynamics and powertrain operation control strategies are solved and implemented with a traffic prediction to provide a complete solution to CAV applications for energy savings. Essentially, prediction of future traffic conditions determines traffic constraints of the optimization problem. Predicted future location of the preceding vehicle formulates the car-following constraint for the target vehicle. The future signal phase and timing determines when the target vehicle can pass the intersection. These constraints are included during the optimization. The proposed control framework can be applied to vehicles of different powertrain types as will be shown in Chapters 3-Chapters 5.

## 2.1. Overall Control Framework

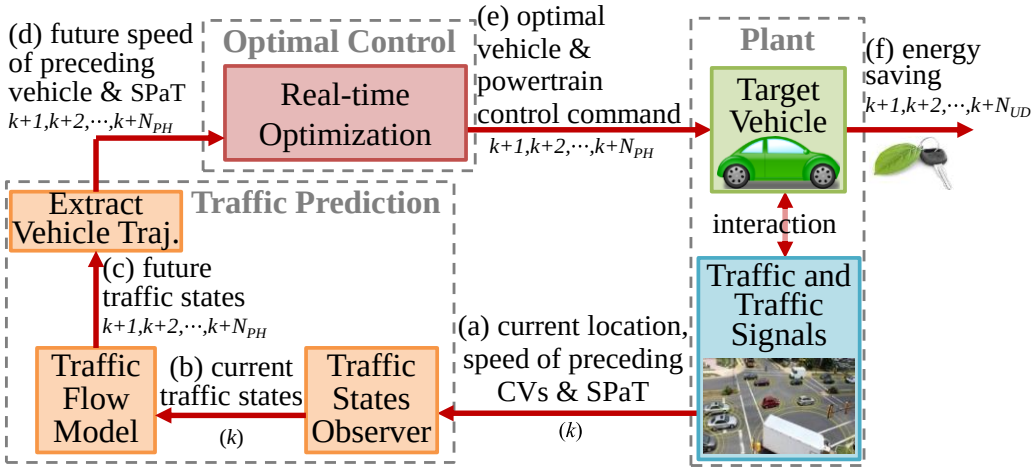


Figure 2.1 Flowchart of the proposed overall control framework.

The optimal control will be solved and implemented in a model predictive control (MPC) fashion. The control will be updated every $N_{UD}$ time step (for example 1 second) as new traffic information becomes available. Optimal control strategy will be solved for the next $N_{PH}$ time steps (optimization horizon, typically 15-20 seconds). Figure 2.1 shows the flowchart of the process: (a) At the beginning of each update instance $k$, new information is obtained through connectivity, including preceding connected vehicles' location and speed, signal phase and timing (SPaT). (b) Based on knowledge of partial traffic states from those CVs, a state observer is used to estimate the current traffic states (including traffic speed and traffic density) of the entire roadway. (c) Once the traffic states of the entire roadway are known, future traffic states are predicted by propagating a traffic flow model forward in time for the prediction horizon (next $N_{PH}$ time steps, same as the optimization horizon). (d) Using these future traffic states, future trajectory of the preceding vehicle is obtained. (e) The energy efficient optimal control strategy is developed for the target CAV. Future trajectory of the preceding vehicle is used to define the car-following distance constraint and future SPaT is used to define the signal

constraint (see the problem formulation of following chapters). Then the optimization problem (depend on the powertrain types of the CAV) is solved to obtain the optimal control (both vehicle and powertrain control command) of the target CAV for the optimization horizon (next $N_{PH}$ time steps). (f) The first $N_{UD}$ steps of the optimal control are implemented on the target vehicle to achieve energy savings then the entire process will be repeated again.

The details of the traffic prediction will be presented in the next section. The solutions to the optimization problem depend on the specific powertrain types of the CAV. For three most common vehicle powertrain types today, ICVs, HEVs and EVs, the control strategies are developed in Chapter 3, Chapter 4, and Chapter 5 respectively.

## 2.2. Traffic Prediction

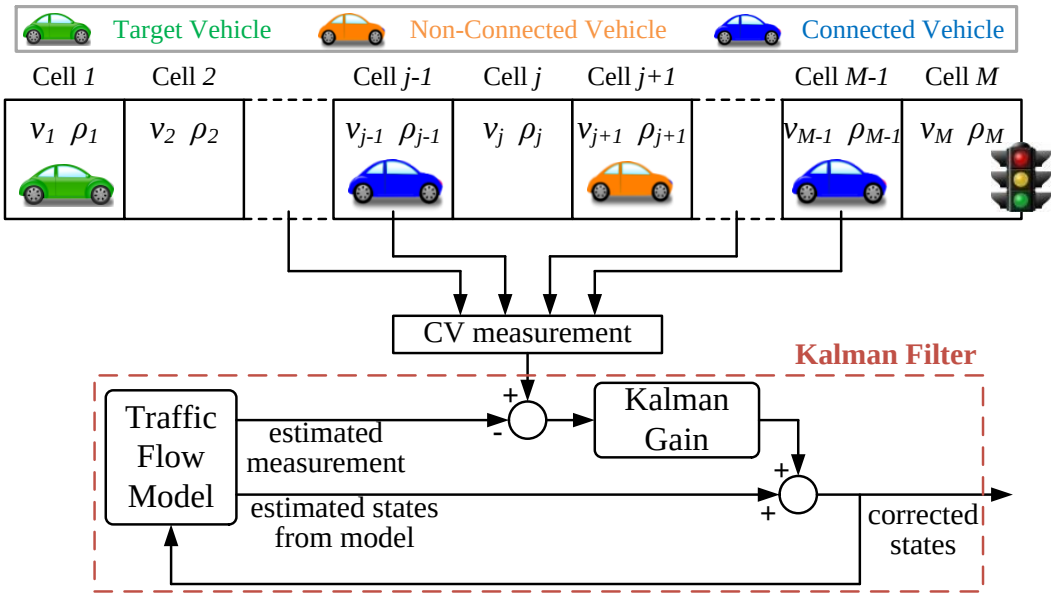


Figure 2.2 Diagram of the traffic states observer (Kalman filter).

In this section, the traffic prediction scheme is developed. The goal is to predict future traffic conditions of the roadway segment from the current location of the target

vehicle to the location of the intersection. As discussed in Section 1.3, the prediction method is developed based on traffic flow theory so that it can be applied to traffic scenarios with different CV penetration rates. The traffic prediction method is illustrated as in Figure 2.2. The roadway segment of interest is modeled from the current location of the target vehicle to the location of the intersection. At first, the roadway segment is divided into $M$ cells. Traffic states of each cell $j$ are described by traffic speed $v_j$ and traffic density $\rho_j$ $(vehicle/meter)$. To model individual vehicle behavior that may deviate from the equilibrium states, second-order traffic flow model is used to describe the state dynamics. Typical second-order flow model includes Payne-Whitham (PW) model [25,62] and Aw-Rascle-Zhang (ARZ) model [26,63]. In this dissertation, the ARZ model is used:

$$\begin{aligned} \rho_t + (\rho v)_x &= 0 \\ v_t + \big(v - \rho p'(\rho)\big)v_x &= \frac{V_e(\rho) - v}{\tau} \end{aligned} \tag{2.1}$$

where $(\cdot)_x$ is the partial derivative with respect to the location; $(\cdot)_t$ is the partial derivative with respect to the time; $V_e(\rho)$ is the equilibrium speed defined by the fundamental diagram; $\tau$ is the speed adaptation rate; $p(\rho)$ is the traffic pressure term; $p'(\rho)$ is the derivative of the traffic pressure term with respect to density $\rho$; $c_0$ and $\gamma$ characterizes the traffic pressure; $v_0$ is the free driving speed; $\rho_{max}$ is the density of stationary traffic; $c$ defines the slope of density drop of congested traffic flow. The two function $V_e(\rho)$ and $p(\rho)$ can be chosen to be either dependent [26,64,65] or independent [66–68]. In this dissertation, two independent functions are chosen:

$$\begin{aligned} p(\rho) &= c_0^2 \cdot \rho^\gamma \\ V_e(\rho) &= \begin{cases} v_0 & \rho < \rho_c \\ c\left(\frac{\rho_{max}}{\rho} - 1\right) & \rho \geq \rho_c \end{cases}; \qquad \rho_c = \rho_{max}/(v_0/c + 1) \end{aligned} \tag{2.2}$$

To numerically solve the traffic flow model, the partial differential equations (2.1)(2.2) are discretized using the finite volume method (FVM). Traffic states of each cell are solved using the analytical solution from each sub-Riemann problem. The details

can be referred to literature [26,65,69] and are omitted here. With the analytical solution, the traffic states can be propagated with low computational burden and high accuracy. During the discretization, the discretized time step $dt$ is select to be the same as the time step of the optimization. The selection of cell length $dx$ is based on: 1) the Courant–Friedrichs–Lewy (CFL) criteria for numerical stability [70]; 2) computational efficiency to ensure real-time implementation capability. When the signal light is red, there will be no flow going out of the cell where the signal is located. When solving the flow model, both traffic density and traffic speed are bounded to avoid negative state values.

The model parameters in the traffic flow model are usually unknown and can vary with traffic conditions. These parameters are considered as additional states. Gaussian random variables are used to consider modeling uncertainties as part of the observer design (will be presented shortly). The lumped state model can be summarized as:

$$\begin{cases} \boldsymbol{z}(k+1) = f[\boldsymbol{z}(k), \boldsymbol{p}(k)] + \boldsymbol{w_z}(k) \\ \boldsymbol{p}(k+1) = \boldsymbol{p}(k) + \boldsymbol{w_p}(k) \end{cases} \tag{2.3}$$

$$\boldsymbol{z}(k) = [\rho_1(k)\ \rho_2(k) \cdots \rho_M(k)\ v_1(k)\ v_2(k) \cdots v_M(k)]^T \tag{2.4}$$

$$\boldsymbol{p}(k) = [c_0(k)\ \tau(k)\ v_0(k)\ \rho_{max}(k)\ c(k)]^T \tag{2.5}$$

where $f$ is the discretized traffic flow model (2.1)(2.2); $w_z(k)$ and $w_p(k)$ describe model uncertainties; $z(k)$, $p(k)$ are stacked traffic states and model parameters.

At every time instance, vehicle speed and location of CVs are obtained through vehicle-to-vehicle communication. The CVs may be distributed in several cells and their vehicle speed is directly linked to the traffic speed at their locations. Therefore, traffic speed of the cells that contain CVs is known and is considered as measurement of partial traffic states. For example, in Figure 2.2, traffic speed of cell $j-1$ and $M-1$ can be known using the vehicle speed of CVs in the cells. It is assumed that $v_j$ is the traffic speed at the center of each cell. The location of the CVs will not always coincide with the center of a cell. The following approximation is used to describe each preceding CV's

speed as the linear interpolated speed of two cells that are adjacent to the preceding vehicle's location:

$$y_i(k) = \alpha_i(k) v_{j_{adj}+1}(k) + [1 - \alpha_i(k)] v_{j_{adj}}(k) + w_{v_i} \quad (2.6)$$

where $y_i$ is the speed of the $i$-th preceding CV; $j_{adj}$ is the index of the last cell the preceding vehicle passed; $\alpha_i(k) = d_i/dx - j_{adj}$ is the interpolation coefficients; $d_i$ is the location of the $i$-th preceding CV; $w_{v_i}$ is the Gaussian random variable to model measurement uncertainties.

On the roadway of interest, there could have a loop detector installed near the intersection that broadcasts traffic flow to the target vehicle. The measurement model is:

$$y_{det}(k) = \rho_{j_{det}}(k) \cdot v_{j_{det}}(k) + w_{det} \quad (2.7)$$

where $j_{det}$ is the index of the cell that the detector is installed; $w_{det}$ is the Gaussian random variable to model the measurement uncertainty.

Once partial traffic states are 'measured' by preceding CVs, the rest unknown traffic states can be estimated using an observer. The unscented Kalman filter (UKF) [71,72] is used since it can handle the non-smooth nonlinearities and consider modeling and measurement uncertainties. Essentially, UKF provides a systematic approach to use the partial traffic states obtained from CVs (measurement) to correct the state estimation and the model parameters (including $c_0, \tau, v_0, \rho_{max}, c$) from the traffic flow model (2.1)(2.2). Standard UKF method is implemented to update the state estimation and the details follows [71]. All the covariance matrices of the UKF are designed based on confidence level of each measurement, traffic states and model parameters, and referred to [62]. Initial values and model parameters are determined based on the specific traffic scenario. The estimated states are bounded to avoid negative traffic density and speed.

Once all traffic states are estimated, the traffic flow model is propagated forward in time (for the next $N_{PH}$ time steps) to predict the future traffic conditions. As part of the UKF, the variance of the speed is estimated. In Section 3.2.5, a systematic approach will

be developed to estimate the prediction uncertainties using the speed variances. Then the prediction uncertainties will be considered explicitly during the optimization to improve the robustness of the optimal control design. This robust optimization approach is critical for the proposed control framework as it ensures that the controller can maintain satisfactory performance even with prediction uncertainties.

# Chapter 3

# Optimization for Internal Combustion Engine Based Vehicles

## 3.1. Introduction

As discussed in Section 1.2.1, for internal combustion engine based vehicles (ICVs), both the vehicle speed and the transmission gear position can be optimized to maximize energy benefits. In addition, when determining the optimal gear position, it is necessary to consider both energy efficiency and drivability (such as satisfying acceleration requirement and avoiding shift busyness). To satisfy drivability, not only current but also future vehicle speed and power demand need to be considered when determining the optimal gear position. At the same time, selecting different gear positions will operate the engine with different efficiencies and affect the selection of optimal vehicle speed. The optimal vehicle speed and optimal gear position are coupled and should be determined simultaneously. This leads to a hybrid optimal control problem as the vehicle speed is continuous and the gear position is discrete. The objective of the optimal control problem is to minimize the energy consumption while satisfying drivability requirement. This is achieved by proactively controlling the vehicle speed and gear position based on predicted future driving conditions using real-time information communicated from other vehicles and signal lights. In literature, several researchers have investigated optimizing vehicle speed and gear position. In [73,74], the most fuel-efficient gear shift schedule was determined based on an engine map. The optimal vehicle speed was then solved for a simplified traffic scenario and roadway slope profile. Future power demand is not considered when generating the shift scheduling and thus it cannot ensure drivability. Researchers in [50,75–77] developed co-optimization methods for vehicle speed and gear position. The traffic scenarios were either simplified without considering following a preceding vehicle, or were predicted using heuristic approaches. Drivability was not

ensured and shift busyness can occur under certain scenarios. Ad-hoc rules may be applied to avoid shift busyness, but gear position will no longer be optimal. In [78,79], the authors assume a known sequence of future gear position to avoid solving a hybrid control problem. The vehicle speed and optimal gear shift timing are optimized for a cruising scenario and an eco-departure scenario. However, in a real traffic scenario, it can be difficult to know the gear position sequence ahead of time.

To obtain optimal vehicle speed and gear position simultaneously with the consideration of both energy efficiency and drivability, a hybrid optimal control problem has to be solved. The hybrid optimal control problems can still be solved by the two approaches mentioned in Section 1.4: indirect methods and direct methods. For indirect methods, hybrid PMP conditions [80,81] can be applied which usually assume a known sequence of the discrete control and the optimal switching time from one discrete control to another is solved. Additional combinatorial optimization is necessary to search for the optimal discrete control sequence [82]. The problem becomes bi-level and there lacks computationally efficient tools to solve the problem. For direct methods, the hybrid optimal control problem is discretized as a mixed integer nonlinear programming (MINLP) problem (there are many solvers such as [83,84]). The optimal discrete control is usually solved using efficient branching techniques [85] (e.g. branch-and-bound and branch-and-cut) and it involves solving multiple sub-NLP problems. A MINLP can be intractable considering potential difficulties in solving sub-NLP problems. However, a mixed integer linear programming (MILP) problem can be potentially solved in real-time (solvers such as [86–88]) as sub-problems will be linear programming (LP) and may be solved efficiently.

In this chapter, a real-time implementable optimal control method is developed to solve optimal vehicle speed trajectory and gear position simultaneously while considering both energy efficiency and drivability. To the best of the authors' knowledge, no current study investigated such kind of control strategy. The optimal control is evaluated for: 1) a

rolling terrain scenario where the target vehicle is not following a nearby preceding vehicle; 2) a vehicle platooning scenario on a signalized urban roadway where the target vehicle is at the end of the vehicle platoon and follows a preceding vehicle. The proposed control method can be potentially applied to other CAV applications and traffic scenarios as well. The future driving conditions are anticipated using the traffic prediction method presented in Chapter 2.2. To reduce the computational burden, optimization variables are carefully selected so that simplification techniques can be applied to transform the original nonlinear hybrid optimal control problem to a mixed integer problem with a convex quadratic objective function and linear constraints. The simplification techniques are carefully selected to avoid sacrificing the accuracy of the vehicle and powertrain models. The problem is then discretized using the pseudo-spectral method [31,89,90] and solved by an efficient state-of-the-art mixed-integer solver.

The rest of this chapter is organized as follows: Section 3.2 formulates the hybrid optimal control problem; Section 3.3 presents the approaches to solve the optimal control including the traffic prediction method, problem simplification, and discretization; Section 3.4 demonstrates the effectiveness of the control in both simulation and experiment for a vehicle platooning scenario; Section 3.5 concludes the chapter.

## 3.2. Problem Formulation

In this section, the fuel efficient vehicle speed and transmission gear position optimal control problem is formulated. The objective is to minimize the fuel consumption while maintaining satisfactory drivability, mobility and driving comfort. The control inputs are vehicle acceleration (engine torque), vehicle braking force, and gear position (discrete). The state equations depend on the vehicle and powertrain models. The constraints include traffic constraints (maintain a safe car-following distance and pass the intersection only when the signal is green), physical limitations (e.g. maximum engine torque constraint), and drivability constraints (avoid engine lugging and shift busyness).

### 3.2.1. State Equation

Point mass vehicle model is used. Denote state vector as $\boldsymbol{x}$, target vehicle's location, speed, and acceleration as $d, v, a$, then

$$\dot{\boldsymbol{x}}(t) = \begin{bmatrix} \dot{d}(t) \\ \dot{v}(t) \end{bmatrix} = \begin{bmatrix} v(t) \\ a(t) \end{bmatrix} \tag{3.1}$$

### 3.2.2. Vehicle and Powertrain Models

The vehicle and powertrain models are [11,13]:

$$\omega_e(t) = n(t) \cdot v(t), \qquad n(t) = r_t(t) r_f / r_r \tag{3.2}$$

$$T_e(t) \cdot n(t) = \underbrace{f_\varphi(t) + C_{wind}\, v(t)^2 + m \cdot a(t) + F_b(t)}_{F_r(t)} \tag{3.3}$$

and

$$f_\varphi(t) = \mu m g \cdot cos[\varphi(d(t))] + mg \cdot sin[\varphi(d(t))] \tag{3.4}$$

where $n$ is the lumped gear ratio (discrete); $r_t$ is the transmission gear ratio (discrete); $r_f$ is the final drive ratio; $r_r$ is the wheel radius; $f_\varphi$ is the sum of rolling and grade resistance; $\varphi$ is the roadway slope angle, which is a function of the target vehicle's location; $\mu$ is the rolling friction constant; $m$ is the vehicle mass; $g$ is the gravity constant; $C_{wind} = 0.5 C_d \rho_a A$ is the wind resistance constant; $C_d$ is the drag coefficient; $\rho_a$ is the density of air; $A$ is the vehicle frontal area; $F_b$ is the vehicle braking force. All units are in SI.

### 3.2.3. Objective Function

The following objective function is used:

$$J = \underbrace{\phi\left(\boldsymbol{x}(t_f)\right)}_{J_{final}} + \int_{t_0}^{t_f} \left[ \underbrace{\dot{m}_f(t)}_{J_{fuel}} + \underbrace{w_1 \cdot (v(t) - v_{lim})^2}_{J_{mobility}} + \underbrace{w_2 \cdot a(t)^2}_{J_{comfort}} \right] dt \tag{3.5}$$

$$\phi\left(\boldsymbol{x}(t_f)\right) = \psi_1 \cdot \left(d(t_f) - d_f\right)^2 + \psi_2 \cdot \left(v(t_f) - v_f\right)^2 \tag{3.6}$$

where $\dot{m}_f$ is the fuel consumption rate; $v_{lim}$ is the speed limit; $t_0$ and $t_f$ are the initial and final time of the optimization horizon; $J_{comfort}$ ensures ride comfort; $J_{mobility}$ ensures mobility; $w_1$ and $w_2$ are two positive weighting factors; $\psi_1, \psi_2$ are

two large positive numbers; $d_f, v_f$ are desired final location and speed of the target vehicle which equal to the final location and speed of the baseline vehicle (see Section 3.4). Penalties on the final states not only ensure a fair comparison between the target vehicle and the baseline vehicle but also ensure that the target vehicle maintains the same mobility as the baseline vehicle. Therefore, the target vehicle can achieve the most fuel efficient control among all vehicle trajectories with the same mobility. The fuel consumption model is fitted using the engine map of a GM 3.6L V-6 engine (the one used in the experiments in Section 3.4)

$$\dot{m}_f(t) = p_{00} + p_{10} \cdot \omega_e(t) + p_{11} \cdot \omega_e(t) \cdot T_e(t) \tag{3.7}$$

where $p_{00}$, $p_{10}$, $p_{11}$ are coefficients of the fitted polynomial. The order of the polynomial is selected to ensure both low computational burden and high accuracy (coefficient of determination $R^2$ is 0.98 for the fitting).

### 3.2.4. Physical Constraints

*Engine Torque Dynamics Constraint* The powertrain and vehicle models (3.2)-(3.4) are algebraic. To account for the engine torque dynamics, the torque change rate is constrained:

$$-\Delta T_{e_{max}} \leq \dot{T}_e(t) \leq \Delta T_{e_{max}} \tag{3.8}$$

*Physical Bounds* The engine speed and engine torque cannot be less than the idling speed $\omega_{e_{idle}}$ and idling torque $T_{e_{idle}}$ (assume the engine will not shut off), and the engine speed cannot be more than the maximum engine speed $\omega_{e_{ub}}$. The vehicle speed is positive and acceleration is bounded:

$$\omega_{e_{idle}} \leq \omega_e(t) \leq \omega_{e_{ub}}, \qquad T_{e_{idle}} \leq T_e(t) \tag{3.9}$$

$$0 \leq v(t), \qquad a_{min} \leq a(t) \leq a_{max} \tag{3.10}$$

### 3.2.5. Traffic Constraints

The traffic constraints depend on the specific CAV application such as whether there is a nearby preceding vehicle or a signalized intersection.

*Car-following Distance Constraint* If the target vehicle is following a preceding vehicle, the car-following distance constraint should be satisfied (if there is no preceding vehicle, this constraint can be relaxed):

$$d_{min} + h_{min} \cdot v(t) \leq d_p(t) - d(t) \leq d_{max} \tag{3.11}$$

where $d_p$ is the estimated location of the immediate preceding vehicle (predicted from the traffic prediction in Section 2.2); $d_p - d$ is the following distance; $d_{max}$ is the upper bound to ensure a satisfactory and realistic traffic throughput; $h_{min}$ is the time headway in seconds; $d_{min}$ is the minimum following distance when the target vehicle is standstill.

To improve the robustness of the control, a systematic approach is developed to consider prediction uncertainties during the optimization. Essentially, uncertainties come from the prediction of future immediate preceding vehicle's location $d_p(k)$. First, uncertainty levels of the prediction are estimated using variance from the traffic prediction observer. Then the optimization is solved with conservative car-following distance constraints (3.14)(3.15) that depend on the uncertainties (variance of prediction). The variance of $d_p(k)$ can be found as:

$$\mathrm{Var}\left(d_p(k)\right) = \mathrm{Var}\left(d_p(1)\right) + dt \cdot \mathrm{Var}\left(\sum_{i=1}^{k-1} v_p(i)\right), k = 2,3,\cdots,N \tag{3.12}$$

$$\mathrm{Var}\left(\sum_{i=1}^{k-1} v_p(i)\right) = \sum_{i=1}^{k-1} \mathrm{Var}\big(v_p(i)\big) + \sum_{i \neq j} \mathrm{Cov}(v_p(i), v_p(j)) \tag{3.13}$$

where (3.12) is based on state dynamics of the immediate preceding vehicle; (3.13) is from statistics [91]. Using (3.12) (3.13), variance of $d_p$ at any time instance $k$ can be found given the variance of each $v_p(i)$ and the covariance between each $v_p(i)$. At each update instance, variance and covariance of the first $v_p(1)$ are known from the observer.

The variance and covariance of future $v_p(i)$ can be estimated by propagating the traffic model forward in time. However, this is computational expensive. It is observed that changes of $v_p(i)$ is small during the optimization horizon. Therefore, it is assumed that the variance and covariance of all $v_p(i)$ approximately equal to the variance and covariance of $v_p(1)$. Once the variance of $d_p(k)$ is calculated, the following conservative car-following distance constraints are implemented:

$$d(k) \geq d_p(k) + \beta \cdot \sigma\left[d_p(k)\right] - d_{max} \tag{3.14}$$

$$d(k) \leq d_p(k) - \beta \cdot \sigma\left[d_p(k)\right] - \left(d_{min} + h_{min} \cdot v(k)\right) \tag{3.15}$$

where $\sigma\left[d_p(k)\right]$ is the standard deviation of the estimated immediate preceding vehicle's location and equals to the square root of the variance $Var(d_p(k))$; $\beta$ determines the confidence level and is selected to be 1 in this work.

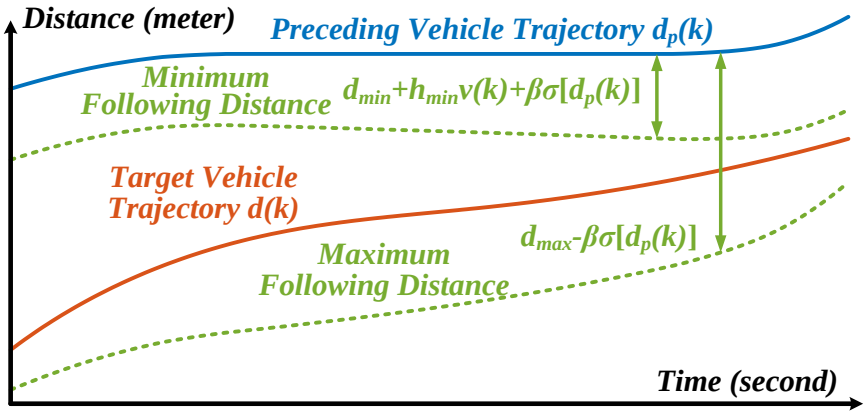


Figure 3.1 Illustration of car-following constraints considering uncertainties.

(3.14)(3.15) are illustrated in Figure 3.1. These constraints essentially enforce a conservative following distance range. A higher variance indicates lower confidence on the prediction and will result in narrower bounds. In Figure 3.1, gap between bounds is decreasing. This is because uncertainties in the prediction will increase when predicting traffic further away from the target vehicle. These boundaries keep the optimization

realistic. The lower bound ensures a safe following distance and the upper bound ensures a satisfactory traffic throughput, i.e. number of vehicles can pass the intersection per unit time. Therefore, the target CAV can maintain a realistic car-following distance that is safe and other vehicles will not likely to cut-in.

*Signal Constraint* If the target vehicle is on an urban roadway with signalized intersections, the target vehicle should pass the intersection only when the signal is green:

$$d(t_r) \geq d_{sig}, \qquad d(t_g) \leq d_{sig} \tag{3.16}$$

where $t_r$ and $t_g$ are the time instances of the beginning of 'next' red light and green light; $d_{sig}$ is the location of the intersection. The definition of 'next' red light or green light is with respect to the signal window which the preceding vehicle is predicted to pass or stop. If based on traffic prediction, the preceding vehicle will pass the intersection within green light cycle (window) number $i$, the target vehicle should generally follow the preceding vehicle to pass the intersection within the same green cycle. That is the target vehicle should pass before the beginning of the $(i+1)$-th red signal cycle and not pass the intersection unless the $i$-th green signal cycle begins. Here yellow light duration is lumped together with the red light, i.e. the target vehicle should not pass the intersection during yellow light for safety. There could be extreme circumstances that the preceding vehicle is predicted to pass the intersection at the very end of a green light cycle. Then the target vehicle has to stop and not to pass the intersection until the $(i+1)$-th green signal cycle begins. If there is no preceding vehicle, the signal cycle number $i$ is obtained by finding when a vehicle cruising at constant speed limit will pass the intersection from the current location of the target vehicle.

### 3.2.6. Drivability Constraints

The following constraints are enforced to ensure a satisfactory drivability performance:

$$T_e(t) + T_{rsrv}(t) \leq T_{e_{max}}(\omega_e(t)) \tag{3.17}$$

$$n(t + t_i) = n(t), \forall t \in [t_0, t_f - t_g], \forall t_i \in [0, t_g) \tag{3.18}$$

where $T_{e_{max}}$ describes the maximum torque line and is a nonlinear function of engine speed; $T_{rsrv}$ is the torque reserve. Essentially, (3.17) ensures a satisfactory acceleration performance by keeping the engine torque away from the maximum torque line by a certain amount of torque reserve. The torque reserve can be determined based on uncertainty levels in the prediction of future traffic and driving conditions. A higher uncertainty level requires a larger torque reserve so that the performance requirement can be achieved. (3.18) ensures that the minimum time duration between two gear shifts is $t_g$ seconds to avoid shift busyness.

### 3.2.7. Initial and Final Conditions

*Initial Conditions* At each update instance, the initial vehicle location, speed and gear position are known:

$$d(t_0) = d_0;\ v(t_0) = v_0;\ g(t_0) = g_0 \tag{3.19}$$

*Final Conditions* Final location and speed of the target vehicle are bounded to the neighborhood of the predicted final location and speed of the preceding vehicle. This ensures that the optimization will have appropriate initial conditions in the next update horizon of the model predictive control (MPC) (the optimal control is implemented in the MPC fashion as presented in Section 2.2):

$$\begin{gathered} d_p(t_f) - \delta_d \le d(t_f) \le d_p(t_f) + \delta_d \\ v_p(t_f) - \delta_v \le v(t_f) \le v_p(t_f) + \delta_v \end{gathered} \tag{3.20}$$

## 3.3. Control Design

In this section, the hybrid optimal control problem formulated in the previous section is solved. Future traffic conditions are predicted by the method presented in Section 2.2 using real-time information communicated from preceding CVs and traffic signal. This traffic prediction method can be applied to mixed traffic scenarios where both CVs and non-CVs are on the road. The output of the traffic prediction is used to formulate the

car-following constraints (3.14)(3.15). To solve the optimal control problem in real-time, the problem is simplified with appropriate approximations. Then it is discretized using the pseudo-spectral method. An efficient numerical solver (Gurobi [86]) is applied to solve the discretized mixed integer programming problem.

### 3.3.1. Problem Simplification

The nonlinear hybrid optimal control problem formulated in Section 3.2 has both continuous and discrete control inputs and can be challenging to solve in real-time. To reduce the computational burden and not to sacrificing the accuracy of the control, simplifications are made with carefully selected optimization variables. The optimization variables include: a) states $x(t)$: target vehicle's location $d(t)$ and speed $v(t)$; b) control variables $u(t)$: target vehicle's acceleration $a(t)$ and braking force $F_b(t)$ (continuous), and gear ratio $n(t)$ (discrete); and c) three additional variables: engine speed $\omega_e(t)$, engine torque $T_e(t)$ and engine power $P_e(t)$. Engine speed $\omega_e(t)$ and engine torque $T_e(t)$ are not independent and are function of states and control variables as shown in (3.2)(3.4). By choosing them as additional variables and considering (3.2)(3.4) as additional equality constraints, the optimization problem can be kept in relatively simple form without introducing complex nonlinearities. This can help keep a low computational burden. The engine power $P_e(t)$ is considered as an additional variable to convexify the objective function as will be presented shortly. For convenience, in the following discussions, the states $x(t)$ and the three additional variables together will be referred as 'generalized states'. The problem simplifications include the following steps:

*1) Objective Function* Both the comfort and mobility terms in the objective function are convex quadratic functions. Only the fuel term is non-convex due to term $\omega_e(t)T_e(t)$. This bilinear term is convexified using the McCormick relaxation which ensures a sufficiently tight convex bounds [92]:

$$\dot{m}_f(t) = p_{00} + p_{10} \cdot \omega_e(t) + p_{11} \cdot P_e(t) \tag{3.21}$$

$$\begin{matrix} T_{e_{idle}} \cdot \omega_e(t) + \omega_{e_{idle}} \cdot T_e(t) - \omega_{e_{idle}} \cdot T_{e_{idle}} \leq P_e(t) \\ T_{e_{ub}} \cdot \omega_e(t) + \omega_{e_{ub}} \cdot T_e(t) - \omega_{e_{max}} \cdot T_{e_{ub}} \leq P_e(t) \end{matrix} \tag{3.22}$$

where $T_{e_{ub}}$ is the upper bound of the right-hand-side of (3.17). $\omega_{e_{idle}}, T_{e_{idle}}, \omega_{e_{ub}}$ are defined in (3.9). Essentially, engine power $P_e$ is an additional variable that replaces the bilinear term and is bounded from below using two hyperplanes in the linear inequality constraints (3.22).

*2) Powertrain Model* The powertrain model (3.2) is a bilinear function involves both continuous and discrete variables. It is converted to linear inequality constraints using the big-M technique [93]. Suppose there are total of $d_g$ gears with ratios: $n_1, n_2, \cdots, n_{d_g}$, and using a binary variable to indicate whether a gear position is activated: $g_i(t) \in \{0,1\}, i = 1,2, \cdots, d_g$, and $\sum_{i=1}^{d_g} g_i(t) = 1$ (only one gear can be activated at any time). Then for each $i = 1,2, \cdots, d_g$:

$$\begin{matrix} \omega_e(t) + (1 - g_i(t)) \cdot (n_i v_{max}) \geq n_i \sum_{i=1}^{d_v} \lambda_i(t) v_i \\ \omega_e(t) + (1 - g_i(t)) \cdot \left(-\omega_{e_{ub}}\right) \leq n_i \sum_{i=1}^{d_v} \lambda_i(t) v_i \end{matrix} \tag{3.23}$$

Essentially, when gear $i$ is engaged ($g_i(t) = 1$), enforcing (3.23) is the same as enforcing the engine speed $\omega_e(t)$ to equal to $n_i v(t)$. When another gear is engaged ($g_i(t) = 0$), (3.23) is not an active constraint and it can be satisfied for any reasonable engine speed and vehicle speed.

*3) Vehicle Model* The vehicle model (3.3) also has a bilinear function with both continuous and discrete variables. Similarly, the big-M technique [93] is used:

$$\begin{matrix} T_e(t) n_i + \left(1 - g_i(t)\right) \cdot \left(F_{r_{max}} + F_{b_{max}}\right) \geq F_r(t) + F_b(t) \\ T_e(t) n_i + \left(1 - g_i(t)\right) \cdot \left(F_{r_{min}} + F_{b_{min}} - T_{e_{max}} n_i\right) \leq F_r(t) + F_b(t) \end{matrix} \tag{3.24}$$

where $F_r$ is the resistance force on the right-hand-side of (3.3); $F_{r_{min}}, F_{r_{max}}, F_{b_{min}}, F_{b_{max}}$ are the upper and lower bound of resistance force and braking force respectively.

The resistance force $F_r$ has two types of nonlinearities and is further simplified. First, the wind resistance term has a quadratic term $v^2(t)$. It is approximated with piecewise linear functions using special ordered sets of variables of type 2 (SOS2) [94]. The SOS2 can be defined in most commercial mixed-integer solvers and solved efficiently [86,87]. An ordered set of non-negative variables $(\lambda_1, \lambda_2, \cdots, \lambda_{d_v})$ is SOS2 if at most two variables are non-zero and the two are adjacent. Let $(v_1, v_2, \cdots, v_{d_v})$ be the break points of each piecewise linear function, then the followings hold [85]:

$$\begin{gathered} v(t) = \sum_{i=1}^{d_v} \lambda_i(t) v_i\,; \quad v^2(t) = \sum_{i=1}^{d_v} \lambda_i(t) v_i^2\,; \\ \sum_{i=1}^{d_v} \lambda_i(t) = 1; \quad \lambda_i \geq 0, \ \ \lambda_i \text{ is SOS2}, \ \ \forall i = 1,2,\cdots,d_v \end{gathered} \tag{3.25}$$

Second, the resistance $f_\varphi(t)$ is nonlinear and depends on the roadway slope angle. Usually, slope of a road will not change aggressively within the optimization horizon (which equals to the traffic prediction horizon and is typically 15-20 seconds). Within this short time period, differences on the grade angle experienced by the target vehicle and the preceding vehicle would be small. Therefore, it is assumed that $f_\varphi(t)$ is known and equals to what the preceding vehicle will experience.

*4) Drivability Constraints* The maximum torque line (3.17) is nonlinear and is approximated using piecewise linear functions:

$$T_e(t) + T_{rsrv}(t) \leq \max_{i=1,2\cdots,dT_e} \left\{ k_{T_e}^i \cdot \omega_e(t) + b_{T_e}^i \right\} \tag{3.26}$$

equivalently

$$\forall i, \ T_e(t) + T_{rsrv}(t) \leq k_{T_e}^i \omega_e(t) + b_{T_e}^i \tag{3.27}$$

The shift busyness constraint (3.18) can be difficult to solve as it must be satisfied for all time instances. It is approximated as:

$$n(t+t_i) = n(t), \forall t_i \in [0, t_g), \ \forall t \in \{t_0, t_0+t_g, t_0+2t_g, \cdots\} \tag{3.28}$$

Essentially, the optimization horizon is partitioned into time intervals of length $t_g$. The constraint (3.28) enforces that the gear shift can only occur when move from one interval to another (see Section 3.3.2).

*5) Car-following Distance Constraints* The car-following distance constraints (3.14)(3.15). depend on the predicted location of the preceding vehicle. Uncertainties in the prediction can result in an actual car-following distance that is near the constraints or even violates the constraints. This brings in challenges to exactly satisfy the constraints at all time. In this work, 'soft constraints' [95] are considered rather than enforcing 'hard constraints'. 'soft constraints' allow violation of the constraints (3.14)(3.15) with additional slack variables:

$$d(t) \geq d_p(t) + \beta \cdot \sigma_{d_p}(t) - d_{max} - s_1 \tag{3.29}$$

$$d(t) \leq d_p(t) - \beta \cdot \sigma_{d_p}(t) - \left(d_{min} + h_{min} \cdot v(t)\right) + s_2 \tag{3.30}$$

and

$$s_1(t) \geq 0, s_2(t) \geq 0 \tag{3.31}$$

where $s_1, s_2$ are two slack variables. In the objective function (3.5), additional terms (convex) are added to penalize the sum of violations at each time step:

$$\begin{aligned} J = \phi\left(\boldsymbol{x}(t_f)\right) + \int_{t_0}^{t_f} \big[\dot{m}_f(t) + w_1 \cdot (v(t) - v_{lim})^2 \\ + w_2 \cdot a(t)^2 + w_3 \cdot s_1^2(t) + w_4 \cdot s_2^2(t)\big] dt \end{aligned} \tag{3.32}$$

where $w_3, w_4$ are two positive weighting factors.

With all the above simplifications, the optimal control problem now has a convex objective function and linear constraints. To justify the simplifications, approximations errors analyzed for the specific vehicle and engine studied in the simulation and experiment (see Section 3.4). The results are summarized in Table 3-1. For the objective function, the average error of the engine power approximation (3.22) is 3.2 kW (corresponds to 0.17 g/s fuel consumption rate). With linearized wind resistance term (3.25), the average approximation error is 5.4 N. This corresponds to about 0.6 Nm engine torque difference. For the approximated maximum torque line constraint (3.26), the average difference is 7.0 Nm. This is reasonable considering that the maximum engine torque is more than 200 Nm. The errors from the roadway slope approximation vary for different roads. For the hilly road of 8 percent maximum slope studied in Section

3.4.1, the average error in the road slope is less than 0.3 degree of grade angle which is relatively a small angle. There are no errors for reformulating the bilinear terms in the powertrain and vehicle model as the simplifications are exact using the big-M method. The above analysis validates that the simplifications are reasonable and will not significantly sacrifice the accuracy of the solution.

Table 3-1 Summary of simplification errors

| | ***Average Simplification Error*** |
|---|---|
| Objective Function | 0.17 g/s |
| Wind Resistance Force | 5.4 N |
| Maximum Torque Line | 7.0 Nm |
| Grade Angle | 0.3 degree |

### 3.3.2. Discretization

In this section, the hybrid optimal control problem is discretized so that it can be solved numerically. The pseudo-spectral method is used as can generally give better accuracy with low computational burden [31] compared to Euler or Runge-Kutta methods. The trajectories of 'generalized states' (see definition in Section 3.3.1) and the continuous control inputs (target vehicle's acceleration and braking force) are parameterized using Lagrange polynomials. The integral of the objective function is calculated using the Legendre–Gauss–Lobatto (LGL) quadrature [96]. After a gear shift, the engine operating point will 'jump' to a different point and causes non-smoothness. To handle these 'jumps', the optimization horizon is divided into $M$ small intervals as shown in Figure 3.2. The gear position is illustrated in purple lines and gear shift can only occur when move from one interval to another. By setting the interval as $t_g$, the shift

busyness constraint (3.28) is naturally ensured after the discretization. In each interval, controls and 'generalized states' are continuous and are parameterized with low-order Lagrange polynomials. The 'jump' of 'generalized states' or controls can be allowed between two intervals (e.g. 'jump' of engine speed). This multi-interval pseudo-spectral method also improves computational accuracy and efficiency [97]. The basic steps of the discretization are presented as below and detailed derivations can be referred to [97,98]

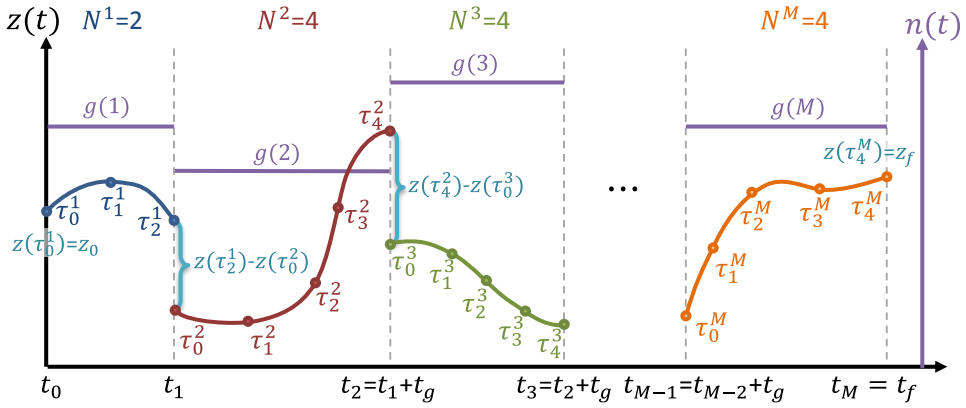


Figure 3.2 Illustration of the discretization. The left axis $z(t)$ and the curves represent the parameterized trajectory of a 'generalized state' or a continuous control. The right axis and the purple lines represent the gear position.

*Step 1 Normalize time* Suppose the $M$ intervals of the discretization are separated at time instances $t_0, t_1, \cdots, t_M$. $t_M$ equals to the final time of the optimization horizon $t_f$. $t_M - t_0$ equals to the optimization horizon $t_{PH}$. Then the time interval between two consecutive break points equals to $t_g$, except for the first and the last intervals. For the first interval $[t_0, t_1]$, if it has been more than $t_g$ seconds since the last gear shift, $t_1 - t_0$ is set to be a small value (e.g. 0.1 seconds); if otherwise, $t_1 - t_0$ is set to be $t_g - t_{shift}$, where $t_{shift}$ is the time elapsed since the last gear shift. This is to avoid shift busyness between two MPC update instances since $t_{UD}$ is typically shorter than $t_g$. Since the optimization horizon might not be divisible by $t_g$, the length of the last time

interval $t_M - t_{M-1}$ equals to $mod\left(t_{PH} - (t_1 - t_0), t_g\right)$, where $mod$ returns the remainder after division. In each interval $i$, the polynomial is of order $N^i$ and passes nodes at the normalized time $\tau^i = \tau_0^i, \tau_1^i, \cdots, \tau_{N^i}^i$ (see Figure 3.2). The normalized time $\tau$ is defined as:

$$\tau = \frac{2}{t_i - t_{i-1}} t - \frac{t_i + t_{i-1}}{t_i - t_{i-1}}, t \in [t_{i-1}, t_i], \tau \in [-1,1] \tag{3.33}$$

*Step 2 Discretize 'Generalized States' and Controls* All 'generalized states' and continuous controls are discretized at the nodes $\tau^i = \tau_0^i, \tau_1^i, \cdots, \tau_{N^i}^i$ for all intervals. Essentially, their values at these nodes are solved.

*Step 3 Discretize State Equations* The dynamic state equation $\dot{x}(t) = f(x, u, t)$ is discretized as

$$\underbrace{\begin{bmatrix} \dot{\mathcal{L}}_0(\tau_0^i) & \dot{\mathcal{L}}_1(\tau_0^i) & \cdots & \dot{\mathcal{L}}_{N^i}(\tau_0^i) \\ \vdots & \vdots & \ddots & \vdots \\ \dot{\mathcal{L}}_0(\tau_{N^i}^i) & \dot{\mathcal{L}}_1(\tau_{N^i}^i) & \cdots & \dot{\mathcal{L}}_{N^i}(\tau_{N^i}^i) \end{bmatrix}}_{D^i} \begin{bmatrix} x(\tau_0^i) \\ x(\tau_1^i) \\ \vdots \\ x(\tau_{N^i}^i) \end{bmatrix} = \begin{bmatrix} f(\tau_0^i) \\ f(\tau_1^i) \\ \vdots \\ f(\tau_{N^i}^i) \end{bmatrix} \left(\frac{t_i - t_{i-1}}{2}\right) \tag{3.34}$$

and

$$\mathcal{L}_k(\tau) = \prod_{m=0, m \neq k}^{N^i} \frac{\tau - \tau_m}{\tau_k - \tau_m}, \qquad i = 1,2, \cdots, M \tag{3.35}$$

where $\mathcal{L}_k(\tau)$ is the Lagrangian basis polynomial; $D^i$ matrix consists of the derivative of the Lagrangian basis polynomials $\dot{\mathcal{L}}_k(\tau_j^i)$ evaluated at node point $\tau_j^i$. The left-hand-side of (3.34) is essentially a linear transform from a state to the derivative of the state $\left[\dot{x}(\tau_0^i) \;\; \dot{x}(\tau_0^i) \;\; \cdots \;\; \dot{x}(\tau_0^i)\right]^T$.

*Step 4 Discretize Objective Function* The integral of the objective function is approximated as summation of the function value evaluated at each node point with weights $w^i = w_0^i, w_1^i, \cdots, w_{N^i}^i$ for each time interval

$$J = \int_{t^{i-1}}^{t^i} h(x,u)dt \approx \frac{t^i - t^{i-1}}{2} \sum_{k=0}^{N^i} w_k^i \, h\left(x\left(\tau_k^i\right), u(\tau_k^i)\right) \tag{3.36}$$

*Step 5 Discretize Constraints* All constraints except for the engine torque dynamics constraints (3.8) must be satisfied at all node points

$$c\big(x(t), u(t)\big) \le 0 \Longrightarrow c\left(x\left(\tau_j^i\right), u\left(\tau_j^i\right)\right) \le 0, \qquad \forall \tau_j^i \tag{3.37}$$

The engine torque rate constraints (3.8) contain derivative terms and are discretized using the $D^i$ matrix:

$$\begin{aligned} D^i \cdot \left[T_e\left(\tau_0^i\right) T_e\left(\tau_0^i\right) \cdots T_e\left(\tau_0^i\right)\right]^T &\le \Delta T_{e_{max}} \cdot \left(\frac{t_i - t_{i-1}}{2}\right) \\ -D^i \cdot \left[T_e\left(\tau_0^i\right) T_e\left(\tau_0^i\right) \cdots T_e\left(\tau_0^i\right)\right]^T &\le \Delta T_{e_{max}} \cdot \left(\frac{t_i - t_{i-1}}{2}\right) \end{aligned} \tag{3.38}$$

*Step 6 Enforce Continuity Constraints* The vehicle location and vehicle speed should be continuous between two consecutive intervals. Therefore, for all $i = 1,2,\cdots,M$:

$$d\left(\tau_{N^{i-1}}^{i-1}\right) - d\left(\tau_0^i\right) = 0, \;\; v\left(\tau_{N^{i-1}}^{i-1}\right) - v\left(\tau_0^i\right) = 0 \tag{3.39}$$

The continuity constraint is not enforced for other 'generalized states' such as engine speed to allow it to 'jump' after a gear shift which reflects what will occur in reality.

### 3.3.3. Obtain Numerical Solution of the Optimal Control

After the simplification and discretization, the hybrid optimal control problem is converted to a mixed integer programming problem with convex quadratic objective and linear equality and inequality constraints. The update horizon is 1 second ($t_{UD} = 1$), the optimization horizon is 15 seconds ($t_{PH} = 15$) and is divided into 5 intervals ($t_g = 3$). In total, if assuming all traffic constraints (car-following distance and signal constraints) are implemented, there will be 394 optimization variables (364 continuous variables and 30 binary variables) with 123 linear equality constraints and 938 linear inequality constraints. The matrices that formulate these constraints are sparse as the result from the pseudo-spectral discretization. This mixed integer programming problem can be solved and implemented in real-time using the Gurobi optimization toolbox, which is considered to be one of the fastest

state-of-the-art mixed integer solver [86,99]. For the 30 binary variables, there could be $6^5$=7776 valid combinations that satisfy constraints on the integer variables. On average, the solver explored about 460 nodes, which is 6% of all possible combinations. When applying the optimal control, for all MPC update instances, the average solving time of the optimization is 0.33 seconds for the rolling terrain scenario, and 0.44 seconds for the vehicle platooning scenario (on a computer with i7 CPU@3.4 GHz). This validates the efficiency of the numerical solution and the real-time potential of the proposed controller. It is expected that the computational burden of the vehicle platooning scenario is higher since it considers additional car-following distance constraints and signal constraints.

### 3.4. Simulation and Experimental Results

In this section, the hybrid optimal control problem is numerically solved and applied to a target CAV in two different roadway scenarios. The first scenario is a rolling terrain scenario where the target vehicle is not following any preceding vehicle. The second scenario is an urban driving vehicle platooning scenario where the target vehicle follows a preceding vehicle to pass signalized intersections. The effectiveness of the optimal control is validated in both simulation and experiment. Experimental validation was conducted on a hardware-in-the-loop testbed [54,55] (see Chapter 6). An actual engine (a GM 3.6L V6 LFX engine) is loaded by a hydrostatic dynamometer whose loading torque is controlled in real-time to match the simulated vehicle dynamics using high-fidelity automatic transmission model and vehicle model. The HIL testbed has been calibrated to match the performance of a 2013 Cadillac SRX [35] (see Chapter 6). It can accurately emulate the performance of the target vehicle for different traffic scenarios in an effective, safe and economical way [54,55]. During the HIL experiments, During the HIL experiments, both the fuel consumption and emissions of the target vehicle can be measured accurately using laboratory instruments (AVL P402 fuel measurement cabinet and AVL SESAM-FTIR exhaust measurement system). The HIL experiment can reflect

unmodeled dynamics and realistically evaluate the performance of the proposed vehicle speed optimization and traffic prediction.

### 3.4.1. Rolling Terrain with No Preceding Vehicle

*3.4.1.1. Traffic Scenario*

In this application, the target vehicle drives on a rolling terrain and receives real-time roadway slopes and speed limits information through communication with the roadside devices [50]. The preceding vehicle is far from the target vehicle and the car-following constraints (3.29)(3.30) are not activated. The baseline vehicle performance was recorded (such as vehicle speed, engine speed) from an actual testing vehicle (a six-speed 2013 Cadillac SRX) using commercial cruise control on an actual roadway in Virginia [100]. The slope and speed limit of this roadway is recorded as well and sent to the optimal controller of the target vehicle. The actual vehicle speed is not perfectly constant but it reflects the realistic performance of an actual vehicle's constant speed cruise controller on a specific roadway.

*3.4.1.2. Simulation Results*

The proposed optimal control is implemented in the MPC fashion to update the roadway slopes and speed limit information, as well as to update the actual vehicle and powertrain states. Figure 3.3 shows the comparison between the baseline vehicle and a target vehicle running the optimal control. In general, the target vehicle tends to accelerate later when going downhill. It has a higher speed when entering the uphill and requires less power to maintain its speed. The baseline vehicle has to spend more efforts to maintain its speed when climbing up and consumes more fuel. Besides a more fuel efficient speed profile, the gear position is optimized as well. The baseline vehicle remains at gear five for the entire duration while the target vehicle alternates between gear five and gear six. It tends to upshift to a higher gear when it anticipates that the upcoming power request is not high (roadway grade is not high). Overall, by optimizing both vehicle speed and gear position, the target vehicle achieves 16.1% fuel benefits. If

considering a vehicle driving with the optimal speed but using the same gear shift strategy as the baseline vehicle (stay at gear five), the total fuel consumption is 139.14 grams and the fuel benefits is reduced to 8%. This shows the effectiveness of the gear position optimization. The gear position optimization can obtain about additional 8% energy saving on top of the vehicle speed trajectory optimization.

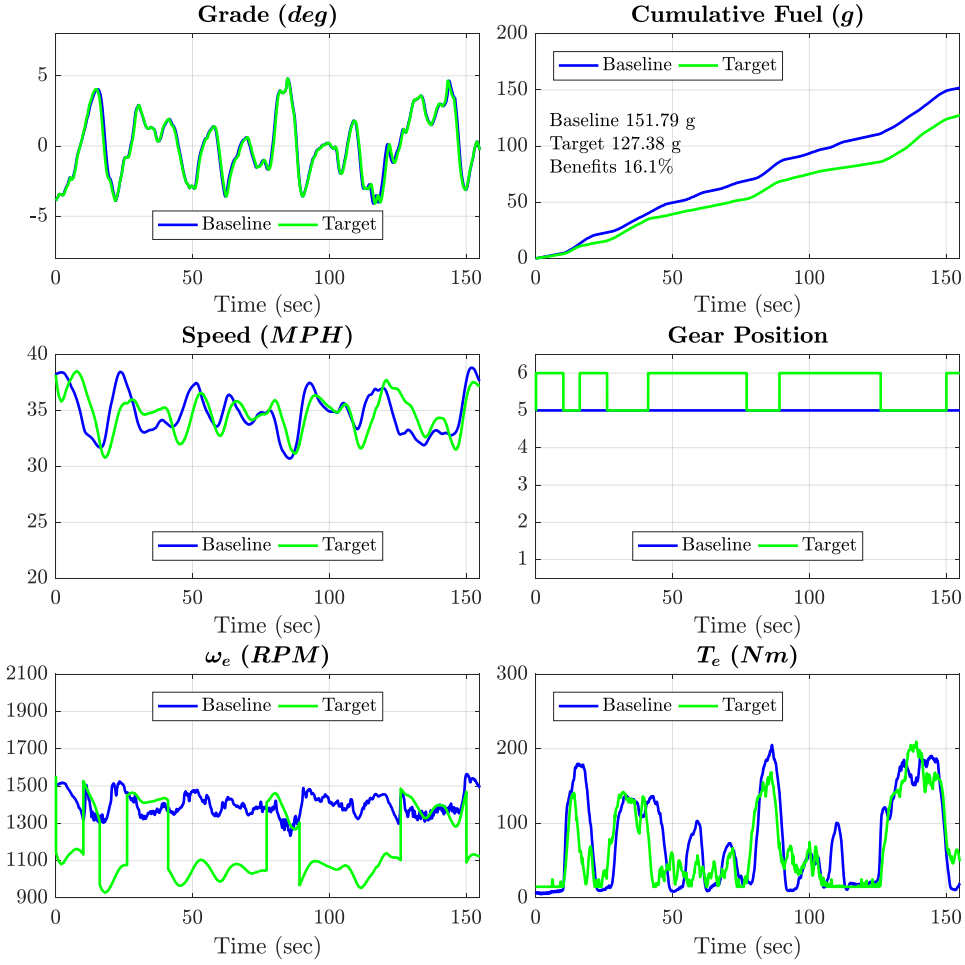


Figure 3.3 Simulation results: baseline vehicle versus target vehicle

*3.4.1.3. Experimental Results*

The optimal control is further validated in hardware-in-the-loop (HIL) experiment. Both the fuel consumption and emissions can be measured using accurate laboratory

instruments. Through the HIL experiment, unmodeled dynamics can be reflected to validate that whether the optimal control can be implementable in an actual vehicle.

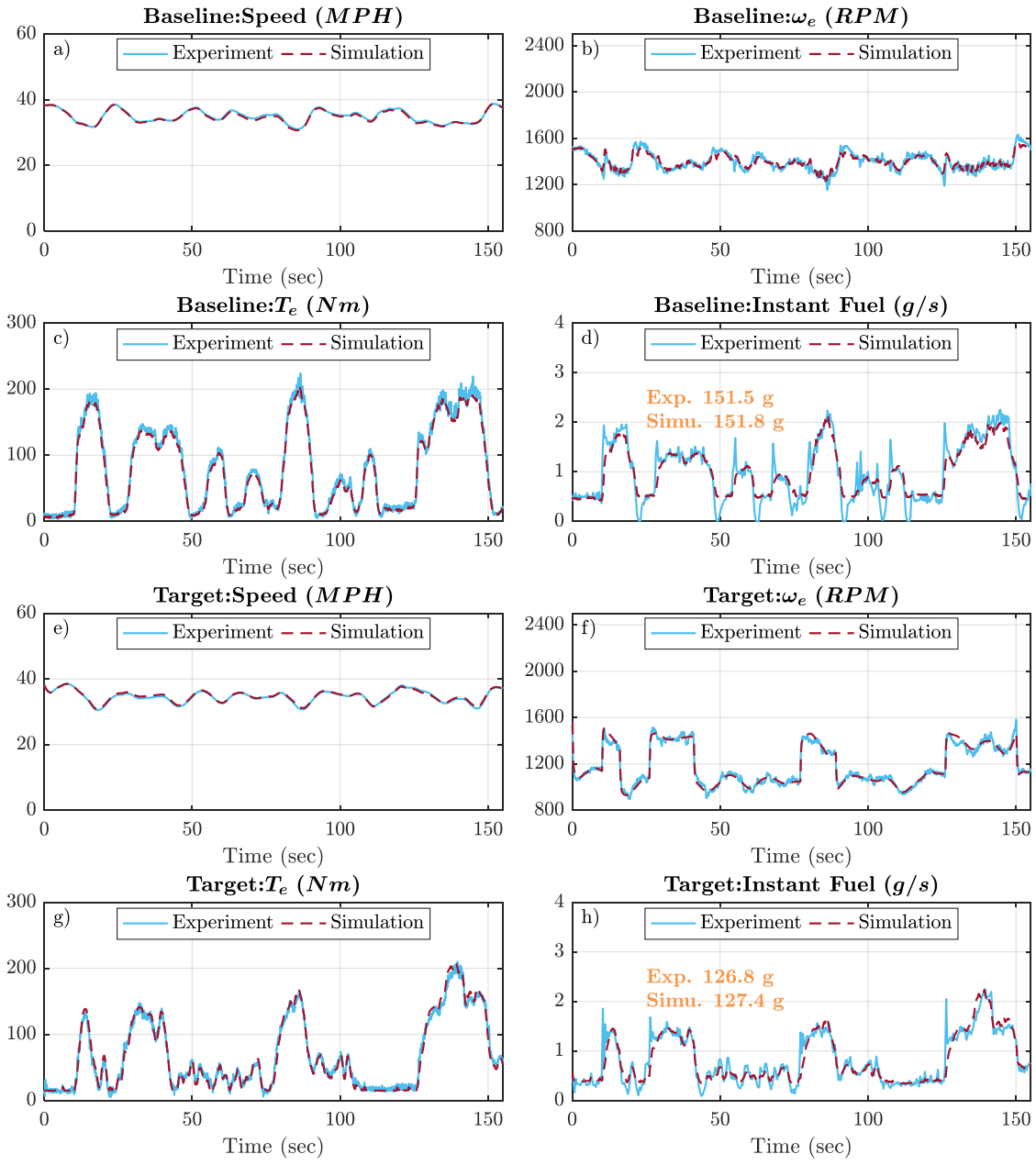


Figure 3.4 Experimental and simulation results comparison: target vehicle

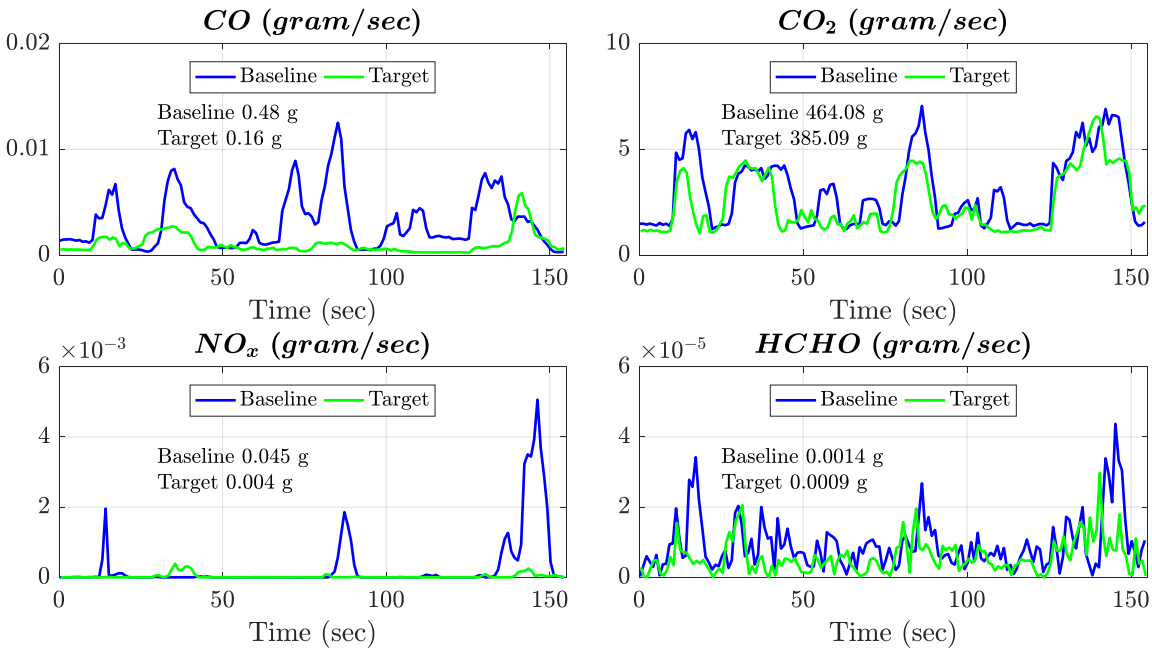


Figure 3.5 Measured emissions: baseline vehicle versus target vehicle

Figure 3.4 shows the comparison between the experimental and simulation results for the target vehicle. The two results match well and this validates the proposed optimal control. Figure 3.5 shows the measured emissions comparison between the baseline vehicle and the target vehicle using the AVL SESAM-FTIR (see Chapter 6). Emissions are not explicitly optimized, however, it can be seen that with reduced fuel consumption, CO2 emissions of the target vehicle are reduced. This is because CO2 emissions are directly linked to the fuel consumption for a gasoline engine. Also, as a consequence of reduced fuel consumption and smoothed vehicle trajectory, pollutes such as CO, NOx and HCHO are significantly reduced with the optimal control strategy. This shows that the proposed optimal control method can bring additional environmental benefits as well.

### 3.4.2. Vehicle Platooning with Preceding Vehicle

*3.4.2.1. Traffic Scenario*

The traffic scenario is generated using the microscopic traffic simulator VISSIM. The roadway is assumed to be an urban roadway of single-lane (assume no lane-change)

with two intersections. The first intersection is at 800 meters and the second one is at 2000 meters. The target vehicle follows the last vehicle in a 12-vehicle platoon. As a case study, it is assumed that 8 vehicles of the platoon are CVs (penetration rate of connectivity is about 70%). The target vehicle uses location and speed information broadcast from all CVs and future signal information to predict future traffic conditions. Perfect communication is assumed without delays and packet drops for simplicity. Information of all non-CVs in the platoon is unknown to the target vehicle. The total travel distance of the target vehicle is 2800 meters and travel time is 176 seconds. All the model parameters of the target vehicle follow a 2013 Cadillac SRX with a 3.6L V6 engine [35].

*3.4.2.2. Simulation Results*

Table 3-2 Fuel consumption of all simulation scenarios

| | ***Baseline*** | ***Target-Speed Optimization*** | ***Target*** | ***Target-Ideal*** |
|---|---|---|---|---|
| Fuel Consumed (grams) | 250.6 | 236.3 | 224.0 | 205.9 |
| Energy Benefits (%) | - | 5.7 | 10.6 | 17.9 |

Table 3-2 shows the fuel consumption comparison of all four simulation scenarios. The ‘Baseline’ vehicle is the immediate preceding vehicle (last vehicle in the 12-vehicle platoon). The gear position of the baseline vehicle is determined by a shift schedule obtained from actual vehicle testing data [54]. The ‘Target’ vehicle is with the proposed optimal vehicle speed and gear position control and traffic prediction. The ‘Target-Ideal’ vehicle is controlled with the proposed co-optimization method but it is assumed to perfectly know the future traffic conditions. The ‘Target-Speed Optimization’ vehicle is driven with the optimal speed profile and the same shift schedule as the baseline vehicle.

In the following discussions, performance of each scenario will be compared and analyzed.

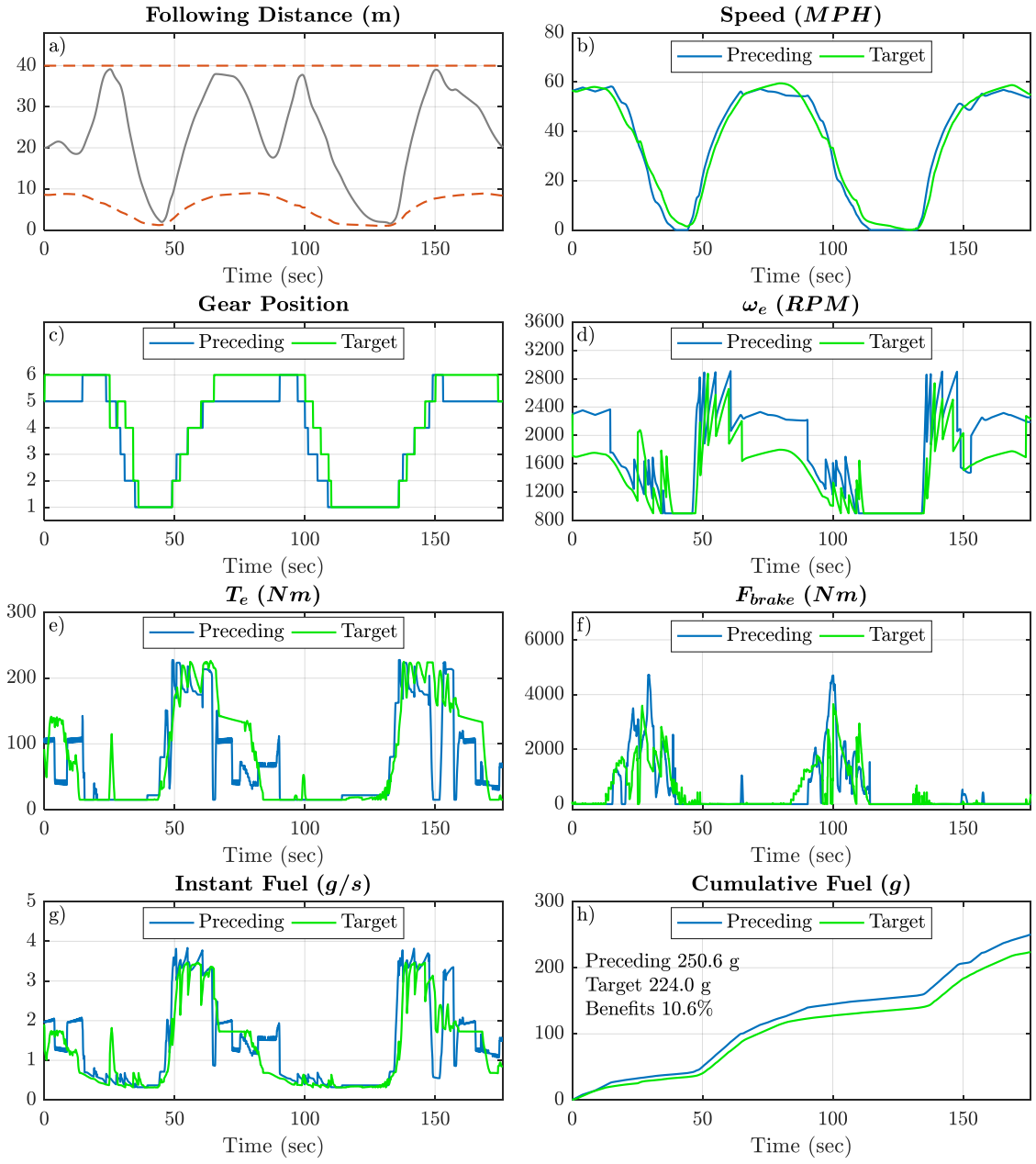


Figure 3.6 Comparison of preceding vehicle (baseline) and target vehicle

Figure 3.6 shows the comparison between the target vehicle and the preceding vehicle (baseline). With co-optimization of vehicle speed and gear position, the target

vehicle achieves 10.6% benefits. The majority of energy benefits come from less deceleration when approaching the intersections and smoother acceleration when leaving the intersections. Figure 3.6a) and Figure 3.6b) show the car-following performance. The preceding vehicle has to slow down and stop completely at both of the two intersections during red signals. The target vehicle intelligently adjusts the car-following distance by anticipating the speed changes of the preceding vehicle. It receives signal phase and timing from the signal lights and knows when the signal will change to red or green. The target vehicle avoids stops by decelerating earlier and glides to pass the intersections. This reduces the amount of braking and avoids idling waste. As shown in Figure 3.6f), the total braking force of the target vehicle is 6.6% less than the preceding vehicle. The following distance between the two vehicles reaches maximum as the target vehicle starts to decelerate during the red signal, and reaches minimum when the target vehicle starts to accelerate again after the signal changes to green. When leaving the two intersections, the preceding vehicle has a more dynamic and aggressive acceleration. For example, due to traffic flow 'disturbances' from the upstream, the preceding vehicle has to decelerate around 150 seconds and then accelerate rapidly to reach the free driving speed. The target vehicle is able to anticipate and smooth out the disturbance and operates the vehicle more efficiently with a smoother acceleration profile. When the target vehicle passes the first intersection and approaches the second intersection (60 seconds to 90 seconds), it first accelerates to reach the maximum speed and then glide. This kind of 'pulse-and-glide' behavior is known to bring in maximum energy efficiency for ICVs [78].

Besides benefits from the optimized vehicle speed trajectory, the gear position is optimized. As shown in Figure 3.6c), the target vehicle stays longer at the highest gear (gear six) to operate the engine in more efficient operating points. The target vehicle shifts to higher gears earlier as it anticipates that the future power request will remain to be low and the drivability will not be deteriorated. The fixed gear shift schedule of the preceding vehicle is conservative and only shifts to the highest gear when the vehicle

acceleration is small or vehicle is deceleration. Without knowing the future power request, the fixed gear shift schedule always prepares the engine for potential accelerations to satisfy the performance request. Figure 3.7 shows the comparison of engine operating points between the preceding vehicle and the target vehicle. The figure further reveals the benefits from gear position optimization. The brake specific fuel consumption (BSFC) contours indicate the efficiency of each engine operating points as unit of fuel consumption rate per unit of power output. In general, the target vehicle tends to operate the engine in more efficient regions, which is around 1600-2000 RPM and 150-200 Nm. The preceding vehicle only operates the engine in higher efficient regions when the power request is high and thus the total fuel consumption is high even the efficiency is high. In general, the preceding vehicle tends to operate the engine more often in higher speed and lower torque regions which are less efficient.

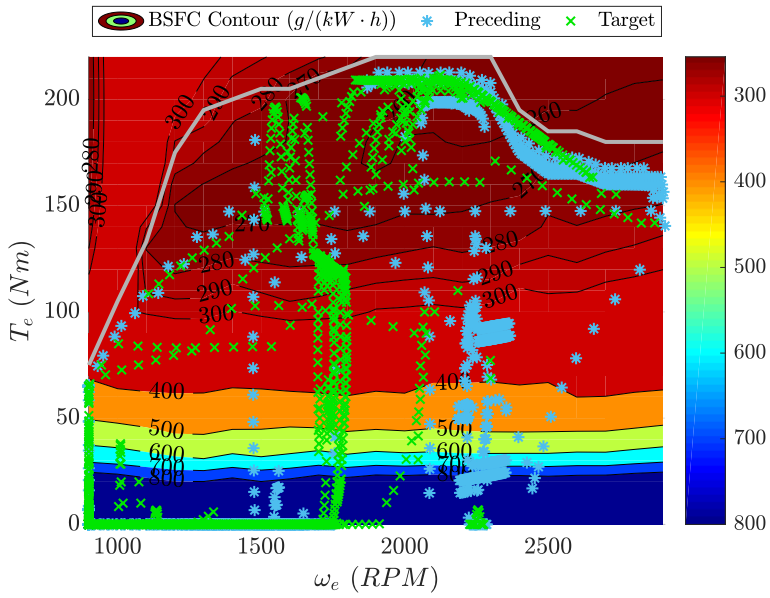


Figure 3.7 Comparison of engine operating points

Considering the ‘Target-Speed Optimization’ vehicle that is driven with the optimal vehicle speed of the target vehicle and the fixed shift schedule of the preceding vehicle,

the fuel consumption is 236.3 grams. In other words, 5.7% fuel benefit is achieved with vehicle speed optimization only. This shows that with co-optimization of vehicle speed and gear position, an additional 4.9% benefit is achieved. This is almost half of the total energy benefits (10.6%).

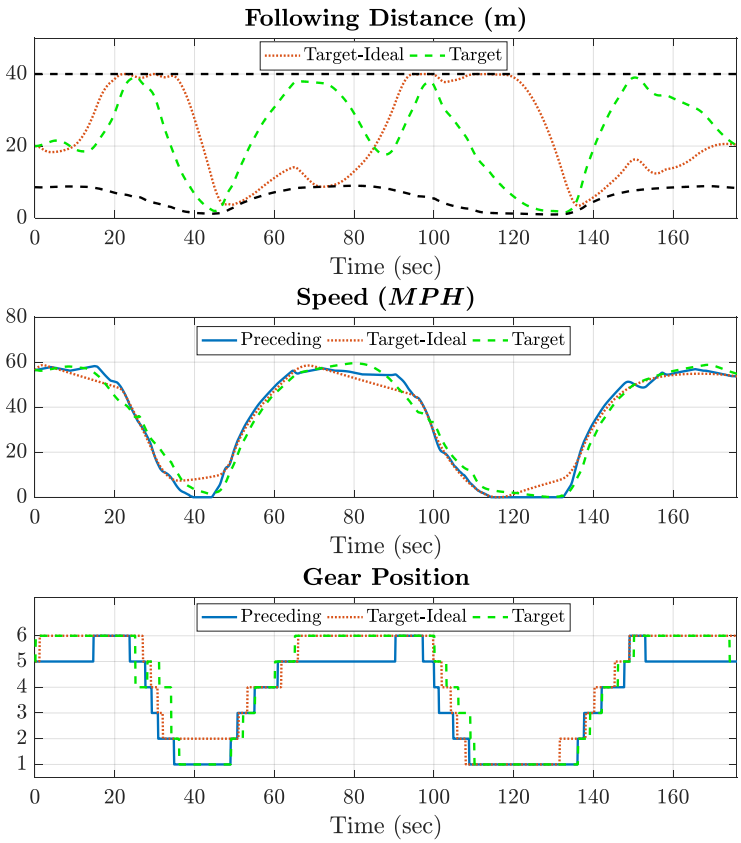


Figure 3.8 Comparison of target vehicle with perfectly known future traffic conditions (Target-Ideal) and target vehicle with predicted future traffic condition (Target)

The optimal control of the target vehicle is solved with the traffic prediction algorithm (Section 2.2). To evaluate the effects of uncertainties in the traffic prediction, the 'Target-Ideal' scenario is simulated where it is assumed that the vehicle can have perfect future traffic information. The results are shown in Figure 3.8. The fuel consumption of the 'Target-Ideal' vehicle is 205.9 grams and the energy benefit is 17.9%.

The ‘Target-Ideal’ vehicle again saves energy through less deceleration and smoother acceleration. Comparing to the target vehicle with prediction, the ‘Target-Ideal’ vehicle uses the freedom in the car-following distance more aggressively and tends to stay closer to the upper and lower bounds and for longer period. The ‘Target-Ideal’ vehicle decelerates earlier and has longer period of gliding and lower maximum speed. This is due to a better coordination of the vehicle speed with the future traffic conditions and a further reduction in the vehicle power demand. For the gear position, the ‘Target-Ideal’ vehicle stays on gear six even longer than the target vehicle with prediction. At the first intersection, the ‘Target-Ideal’ vehicle completely avoids the downshift to the first gear which improves energy efficiency.

*3.4.2.3. Experimental Results*

Both the performance of the ‘Baseline’ vehicle and the ‘Target’ vehicle are evaluated on the HIL testbed. The HIL experiments can reflect unmodeled vehicle and powertrain dynamics and realistically evaluate the performance of the proposed optimal control.

Figure 3.9 shows the powertrain dynamics of the target vehicle and the preceding vehicle (baseline) recorded on the HIL testbed. It can be seen that both the measured engine speed and engine torque match well with the simulation profiles. The average difference between simulated engine speed and measured engine speed is 29 RPM and the difference between engine torques is 5.6 Nm. The simulated vehicle speed matches the reference vehicle speed profile as well. The measured fuel consumption benefit is 10.0% which validates the fuel benefits from vehicle speed and gear position co-optimization (in the simulation, the fuel benefits is 10.6%). All these HIL experimental results validate that the proposed optimal control can be potentially implemented on an actual vehicle and the energy benefits can be obtained.

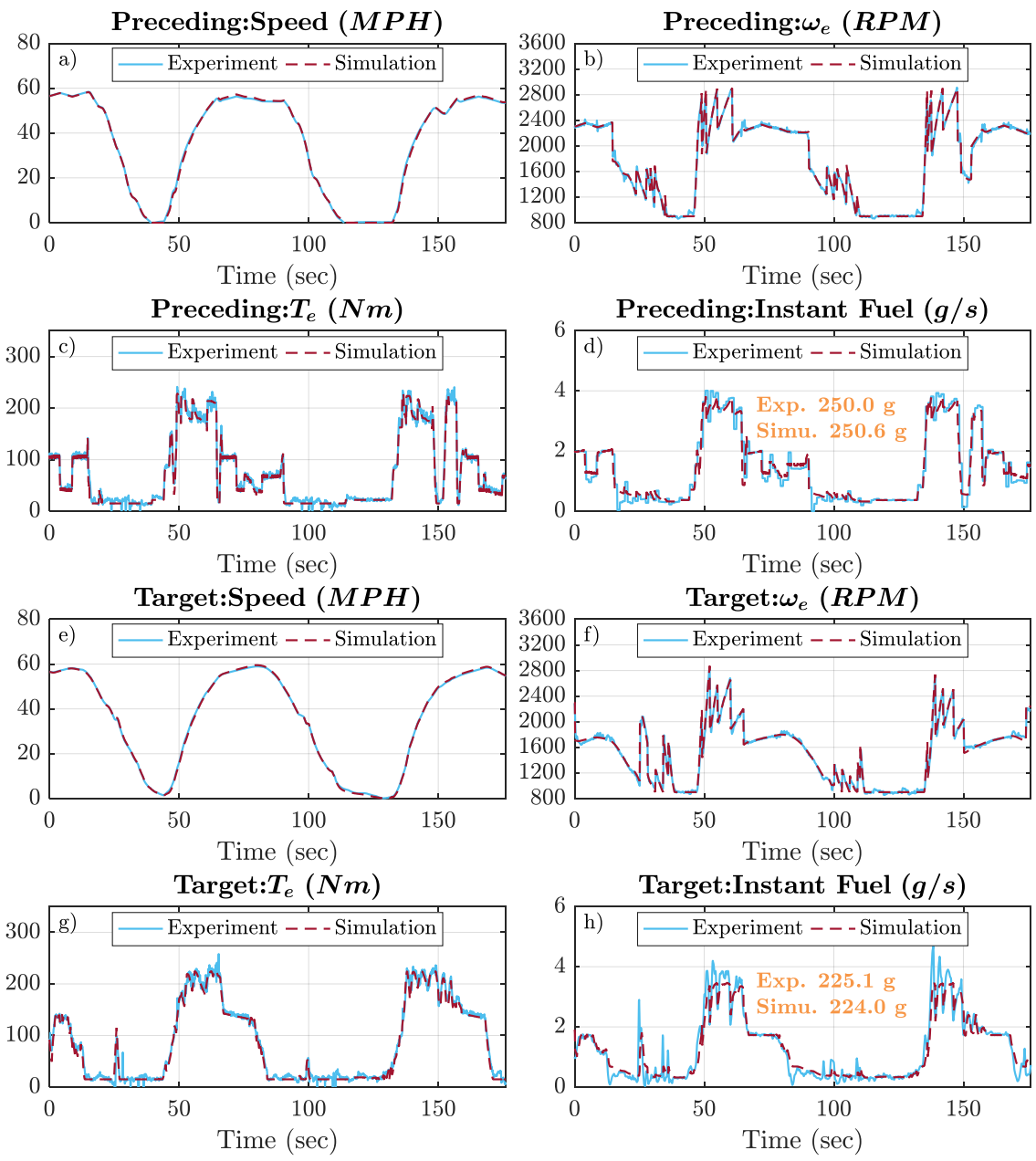


Figure 3.9 Experimental results of the powertrain dynamics: preceding vehicle (baseline) versus target vehicle

## 3.5. Conclusion

In this chapter, a real-time implementable optimal control method is proposed for ICVs to simultaneously optimize vehicle speed and gear position. During the optimization, both fuel efficiency and drivability are considered to ensure that the optimal control strategy is realistic and implementable. The optimization problem is formulated and transformed to a mixed integer programming with a convex quadratic objective function and linear constraints so that it can be solved in real-time. The effectiveness of the proposed control strategy was evaluated for two traffic scenarios in both simulation and experiment. In the rolling terrain scenario, there is no nearby preceding vehicle. The target vehicle anticipates the future roadway slopes and cruises with the optimal speed and gear position. The average computational time of the optimization is 0.33 seconds. The results have shown that the fuel benefit is 16.1% compared to a baseline vehicle using constant speed cruising control. In addition, the optimal control can significantly reduce emissions. In a vehicle platooning scenario on an urban roadway, the target vehicle follows the last vehicle in the platoon and uses the traffic prediction method to anticipate future traffic conditions based on information enabled by connectivity. The average computational time of the optimization is 0.44 seconds. The results have shown that the target vehicle can achieve 10.6% fuel benefits compared to the immediate preceding vehicle.

# Chapter 4

# Optimization for Hybrid Electric Vehicles

## 4.1. Introduction

Hybrid electric vehicles (HEVs) have different powertrain architecture than internal combustion engine based vehicles (ICVs). As discussed in Section 1.2.2, for power-split HEVs, besides the vehicle speed optimization, the powertrain operation can be optimized in two folds, one is the engine operating points, and the other is the power-split between the engine and the battery. Previous studies have investigated eco-oriented HEVs and they can typically be classified into two categories. The first category focuses on the optimization of powertrain operation and control to maximize fuel efficiency (also known as 'hybrid vehicle power management' in literature). Several approaches have been proposed such as dynamic programming (DP) [101,102], equivalent consumption minimization strategy (ECMS) [103,104], and Pontryagin's minimum principles (PMP) [105,106]. The second category focuses on the vehicle speed trajectory optimization taking advantage of connectivity and automation. The vehicle level optimal control is designed to operate with minimized energy consumption and maximized mobility [107–110]. There needs a systematic study on real-time integrated optimization of vehicle dynamics and powertrain operation for HEVs.

In addition, most of the aforementioned studies only deal with CAV applications on a level road. This is not always a reliable assumption. For example, the intelligent merging application may require a ramp vehicle to accelerate rapidly to join a platoon on an uphill. Instead of saving fuel from reducing waiting time and unnecessary stop-and-go, due to the high grade resistance on an uphill, this rapid acceleration maneuver can actually cause excessive energy consumption. Hence, it is essential to take account of the road topography information. In addition, there is more room to improve fuel efficiency

on rolling and mountainous terrain. Past research demonstrated that a 6 percent increase in a roadway grade leads to 40 to 94 percent increase in fuel consumption [111] . Another study confirmed that the fuel economy on flat routes is superior to that on rolling or mountainous routes by approximately 15 to 20 percent [112].

To summarize, past studies suggest that fuel efficiency can be improved at two levels: vehicle level and powertrain level. The majority of the previous studies focused on only the vehicle level. Seldom did researchers conduct combined optimization for two levels. Nevertheless, it is expected that the integrated optimization on a hybrid vehicle would produce the highest fuel efficiency than individual level optimization. It is also crucial to consider road topography information when developing such optimization strategies.

The reminder of the chapter is organized as follows: Section 4.2 'Control structure' provides the high-level description of the control structure; Section 4.3 'Problem Formulation and Control Design' presents the optimization problem formulation and the associated solution; Section 4.4 'Simulation Evaluation' identifies all the specifics of the simulation and presents its results and findings; and finally, Section 4.5 'Conclusion' discusses the conclusions.

## 4.2. Control structure

In this section, the structure of the integrated optimization controller is presented in Figure 4.1. The system considered from the perspective of an individual HEV vehicle, of which the state $\boldsymbol{x}$ can be described by the vehicle's position, speed and battery state-of-charge (SOC). The control structure is based on the assumption that the vehicle is equipped with vehicle-to-infrastructure (V2I) and vehicle-to-vehicle (V2V) communication devices. Communication is assumed to be reliable, that is no communication issues such as delay and data packet loss. At the beginning of the optimization (time instant $t_0$), the controller obtains the following real-time traffic information depending on whichever is available: future road altitude, dynamic speed

limit, signal phase and timing (SPaT) and predicted preceding vehicle location (from the traffic prediction presented in Chapter 2). The current states $\boldsymbol{x}$ can be obtained from GPS and on-board sensors. The control inputs (vehicle acceleration $a$ and the battery power $P_{batt}$) are optimized to achieve the control objectives. The control objectives include minimizing fuel consumption, optimizing mobility and maximizing comfort, under the constraints of traffic rules. The balance among different objectives is realized via weighting factors.

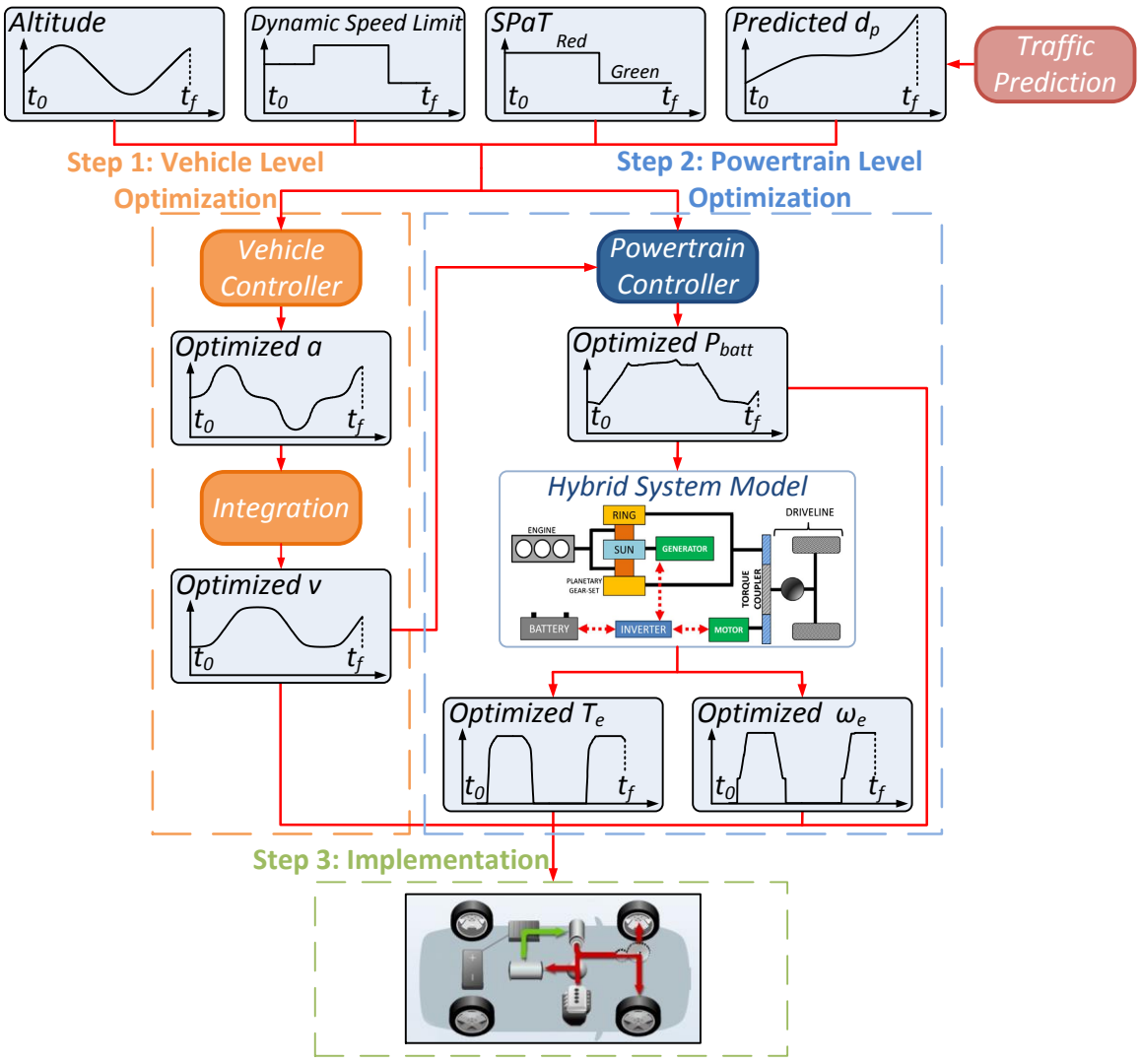


Figure 4.1 Control structure of the optimization.

Under the ideal condition, both control inputs should be solved within one optimal control problem. In this work, in order to simplify the problem for potential real-time and practical applications, the two control inputs are solved separately. In other words, there are two optimal control problems that are solved consecutively (i.e., vehicle level optimization and powertrain level optimization). For each time horizon from $t_0$ to $t_f$, the optimization follows the process as shown in Figure 4.1. The integrated optimization of vehicle dynamics and powertrain operation (steps 1 to 3) is performed in a consecutive order. Each optimization level takes the output from the previous level as input. The process can be summarized as:

Step 1 *Vehicle Level Optimization*. Future roadway information (road altitude and dynamic speed limit) and traffic conditions information (SPaT and preceding vehicle location) is sent to the vehicle level controller for optimizing the vehicle acceleration trajectory (details in Section 4.3.1).

Step 2 *Powertrain Level Optimization.* Future roadway information, traffic conditions information, optimal vehicle speed and acceleration trajectories are sent to the controller from step 1. The controller optimizes engine operating point (engine torque $T_e$ and engine speed $\omega_e$) and power-split ($P_{batt}$) simultaneously (details in Section 4.3.2).

Step 3 *Implementation*. Optimal control commands $P_{batt}$, $T_e$, and $\omega_e$ are calculated and sent to control the vehicle.

## 4.3. Problem Formulation and Control Design

This section presents the optimization problem formulation and the associated solution. The vehicle level and powertrain level optimization are formulated and solved consecutively. For the vehicle level optimization, when there is no nearby preceding vehicle, the car-following distance constraints are not enforced. The optimal control problem is solved using the Pontryagin Minimum Principle (PMP) [113]. When following a preceding vehicle, the optimal control is discretized first and then solved

using nonlinear programming (NLP). For the powertrain level optimization, the optimal power-split is always solved using the PMP. Detailed formulation of the vehicle level optimization and the powertrain level optimization is presented in the following sections (Section 4.3.1 and Section 4.3.2).

### 4.3.1. Vehicle Level Optimization

As shown in Figure 4.1, this is the first step of the optimization process. The input of the vehicle level optimization is the future roadway information (road altitude and dynamic speed limit) and traffic conditions information (SPaT and preceding vehicle location). This optimization is for minimizing fuel consumption, optimizing mobility and maximizing comfort. This optimization generates an optimal acceleration trajectory. It is the most fuel efficient among all vehicle trajectories with the same mobility (travel same distance within same time).

*4.3.1.1. State Equation*

On the vehicle level, the state vector $\boldsymbol{x_v}$ is the same as ICVs described in Section 3.2.1 (states are distance $d$ and speed $v$ of the target vehicle). The state equation is

$$\dot{\boldsymbol{x}}_v(t) = \underbrace{\begin{bmatrix}\dot{d}(t)\\ \dot{v}(t)\end{bmatrix}}_{\dot{\boldsymbol{x}}_v} = \underbrace{\begin{bmatrix}v(t)\\ a(t)\end{bmatrix}}_{f(\boldsymbol{x}_v,a)} \tag{4.1}$$

*4.3.1.2. Objective Function*

The objective function takes the same form as ICVs (Section 3.2.3) with a different fuel consumption model:

$$J = \phi\left(\boldsymbol{x}(t_f)\right) + \int_{t_0}^{t_f} \underbrace{\left[\dot{m}_f(t) + w_1 \cdot (v(t) - v_{lim})^2 + w_2 \cdot a(t)^2\right]}_{L(\boldsymbol{x}_v,a)} dt \tag{4.2}$$

$$\phi\left(\boldsymbol{x}(t_f)\right) = \psi_1 \cdot \left(d(t_f) - d_f\right)^2 + \psi_2 \cdot \left(v(t_f) - v_f\right)^2 \tag{4.3}$$

$$\dot{m}_f(t) = \beta_1 \cdot P_{req}(t) + \beta_0 \tag{4.4}$$

where all variables follow the same definitions as in Section 3.2. The fuel consumption model is based on vehicle power request $P_{req}$:

$$P_{req}(t) = \left[\underbrace{\mu mg \cdot \cos\big(\varphi(t)\big) + mg \cdot \sin\big(\varphi(t)\big)}_{f_{\varphi}(t)} + C_{wind}\, v(t)^2 + m \cdot a(t)\right] \cdot v(t) \quad (4.5)$$

When positive, $P_{req}$ represents the summation of power spent on vehicle state change. When negative, $P_{req}$ describes the power charged into battery. The values of the coefficients in this model (4.5) are listed in the Section 4.4.

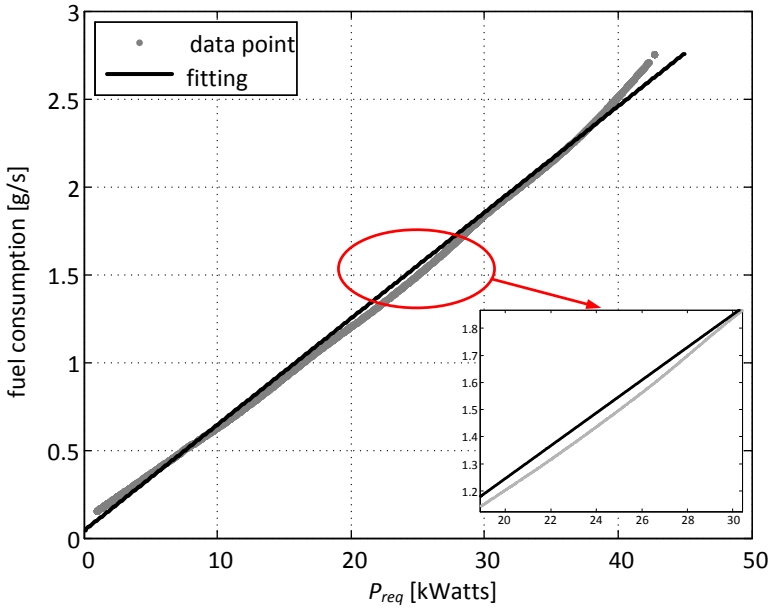


Figure 4.2 Fitting vehicle power request vs. fuel consumption.

The coefficients ($\beta_0$ and $\beta_1$) were acquired by fitting a linear equation of power request against fuel consumption, as in Figure 4.2. Power requests were bounded between the two extreme engine operating points. When fitting the model, the battery power was assumed to be zero to eliminate its effect on the fuel consumption. The fuel consumption for different engine operating points was found by referring to an engine map [105]. The enlarged portion of Figure 4.2 shows the most efficient engine operating region. The fuel consumption model can take forms other than the power request based on the engine map, for example, considering models of the hybrid electric powertrain. However, the

computational time will increase significantly if a complicated powertrain model is used. To make it possible for real-time implementation, in this work, fuel consumption is modeled as a linear function of the vehicle power demand based on the IC engine map.

*4.3.1.3. Vehicle Model*

The longitudinal vehicle dynamics model is

$$ma(t) = F_t(t) - (\mu mg \cdot \cos(\varphi(t)) + mg \cdot \sin(\varphi(t)) + C_{wind}\, v(t)^2) \quad (4.6)$$

where $F_t$ is the thrust force and all other variables follow the same definitions as in Section 3.2. The thrust force depends on the combined output of the IC engine and the electric motor. The complete model is referred to [101,105]. Here, the dynamic model is simplified to keep the clarity and help readers understand the core part of the proposed optimal controller.

*4.3.1.4. Constraints and initial conditions*

When solving for the optimal vehicle speed profile, the following state constraints are considered:

*Acceleration Constraint*: To ensure that all acceleration solutions are feasible provided the engine maximum power and brake condition, the maximum acceleration is set as $(F_{t_{max}} - F_r)/m$, and maximum deceleration is set as $-5\ m/s^2$. $F_{t_{max}}$ is the maximum thrust force of the powertrain, $F_r$ is the summation of the three resistant forces (on the right-hand-side of (4.6)). To be noted, this acceleration range is solely for eco-drive optimal controller which is one of the many applications that would be installed on CAVs and could be over-ruled by collision prevention applications. In other words, vehicles are able to brake much faster than $-5\ m/s^2$ when safety hazard arises. This constraint can be expressed as the following:

$$\mathcal{A}_v = \{a | a_{\min} \le a(t) \le a_{\max}, \forall t \in [t_0, t_f]\} \quad (4.7)$$

*Speed constraint:* The vehicle speed has physical limitations. For example, the speed should be non-negative and follow the speed limit. This constraint can be specified as:

$$\mathcal{V}_v = \left\{ v \middle| v_{\min} \le v(t) \le v_{\max}, \forall t \in [t_0, t_f] \right\} \tag{4.8}$$

*Initial Conditions*: The initial conditions are

$$d(t_0) = d_0, v(t_0) = v_0; \tag{4.9}$$

*Car-following Distance Constraint* If there is a preceding vehicle, the car-following distance constraint should be satisfied (otherwise, this constraint can be removed).

$$d_{min} + h_{min} \cdot v(t) \le d_p(t) - d(t) \le d_{max} \tag{4.10}$$

*Signal Constraint* If the target vehicle is on an urban roadway with signalized intersections, the target vehicle should pass the intersection only when the signal is green:

$$d(t_r) \ge d_{sig}, \qquad d(t_g) \le d_{sig} \tag{4.11}$$

All variables follow the same definitions as in Section 3.2 and future location of the preceding vehicle can be predicted using the method presented in Section 2.2. As will be shown in the next section, depends on whether or not a preceding vehicle exists, two different methods are used to solve the optimal control problem.

*4.3.1.5. No Preceding Vehicle: Solution Based on Pontryagin's Minimum Principle*

The PMP based method is more suitable to solve optimal control problems without state constraints. The optimality conditions of these problems can be obtained relatively straightforward. When considering a rolling terrain scenario, the target vehicle is not following a preceding vehicle. Constraint (4.10) is not active and constraint (4.8) can be 'automatically' satisfied by penalizing the mobility in the objective function (4.2). With the mobility cost, the optimal vehicle speed cannot have large deviation from the speed limit. Hence it is unlikely to violate constraint (4.8). Therefore, the optimal control problem will have no state constraints when not following a preceding vehicle. To solve the optimal control, the state equation can be considered as a constraint argument with the objective function using a Lagrange multiplier (also known as co-state). The following Hamiltonian $\mathcal{H}_v$ is defined:

$$\mathcal{H}_v(\boldsymbol{x_v}, a, \boldsymbol{\lambda_v}) = \boldsymbol{\lambda}_v^T \cdot f(\boldsymbol{x_v}, a) + L(\boldsymbol{x_v}, a) \tag{4.12}$$

where $\boldsymbol{\lambda_v}$ can be interpret as the Lagrange multiplier and represents the sensitivity (gradient) of the cost with respect to changes in the state variable. In other words, it is the change of $J$ caused by a small change $\partial \boldsymbol{x_v}$ on the state $\boldsymbol{x_v}$. $\boldsymbol{\lambda_v}$ is also known as the co-state. According to the PMP, for all control inputs (vehicle acceleration) that falls in the premises of permissible controls set $\mathcal{A}_v$, the optimal control $a^*$ must satisfy:

$$\mathcal{H}_v(\boldsymbol{x_v^*}, a^*, \boldsymbol{\lambda_v^*}) \leq \mathcal{H}_v(\boldsymbol{x_v^*}, a, \boldsymbol{\lambda_v^*}), \quad \forall a \in \mathcal{A}_v, t \in [t_0, t_f] \tag{4.13}$$

The above Hamiltonian law could be expressed alternatively as the following necessary conditions:

$$\text{(i)}\ \ 0 = \frac{\partial \mathcal{H}_v}{\partial a}, \qquad \text{(ii)}\ \ \dot{\boldsymbol{\lambda}}_{\boldsymbol{v}} = -\frac{\partial \mathcal{H}_v}{\partial \boldsymbol{x_v}}, \qquad \text{(iii)}\ \ \dot{\boldsymbol{x}}_{\boldsymbol{v}} = \frac{\partial \mathcal{H}_v}{\partial \boldsymbol{\lambda_v}} \tag{4.14}$$

Equation (iii) in (4.14) is equivalent to the vehicle dynamics. Equations (i) and (ii) serve to solve for optimal control. For the vehicle level optimization, substituting Hamiltonian with the cost function of this study:

$$\begin{aligned} \mathcal{H}_v &= \boldsymbol{\lambda_v}^T \cdot \dot{\boldsymbol{x}}_{\boldsymbol{v}}(t) + L(\boldsymbol{x_v}, a) \\ &= \lambda_1(t) \cdot v(t) + \lambda_2(t) \cdot a(t) \\ &\quad + \beta_1 \cdot \left[f_\varphi(t) + C_{wind}\, v(t)^2 + m \cdot a(t)\right] \cdot v(t) + \beta_0 \\ &\quad + w_1 \cdot (v(t) - v_{lim})^2 + w_2 \cdot a(t)^2 \end{aligned} \tag{4.15}$$

Equation (i) in (4.14) provides:

$$\frac{\partial \mathcal{H}_v}{\partial a}(\boldsymbol{x_v}, a, \boldsymbol{\lambda_v}) = \lambda_2(t) + m \cdot \beta_1 \cdot v(t) + 2w_2 \cdot a(t) = 0 \tag{4.16}$$

It can be rearranged to provide the control law:

$$a(t) = \frac{\lambda_2(t) + m \cdot \beta_1 \cdot v(t)}{-2w_2} \tag{4.17}$$

Equation (ii) in (4.14) provides:

$$\dot{\lambda}_1 = \lambda_1(t + dt) - \lambda_1(t) = -\frac{\partial \mathcal{H}_v}{\partial d}(\boldsymbol{x_v}, a, \boldsymbol{\lambda_v})dt = 0 \tag{4.18}$$

$$\begin{aligned} \dot{\lambda}_2 &= \lambda_2(t + dt) - \lambda_2(t) = -\frac{\partial \mathcal{H}_v}{\partial v}(\boldsymbol{x_v}, a, \boldsymbol{\lambda_v})dt \\ &= -\lambda_1(t)dt - \left\{\beta_1 \cdot \left[f_\varphi(t) + ma(t) + 3C_{wind}\, v(t)^2\right] - 2w_1 \cdot (v(t) - v_{lim})\right\}dt \end{aligned} \tag{4.19}$$

The final states are penalized by the objective function. (4.2). The following final condition for $\lambda_v$ needs to be met as the transversality conditions

$$\boldsymbol{\lambda}_v(t_f) = \frac{\partial}{\partial \boldsymbol{x}_v}\phi(\boldsymbol{x}_v(t_f)) \tag{4.20}$$

which gives:

$$\lambda_1(t_f) = 2 \cdot \psi_1 \cdot \big(d(t_f) - d_f\big), \qquad \lambda_2(t_f) = 2 \cdot \psi_2 \cdot (v(t_f) - v_f) \tag{4.21}$$

To solve the aforementioned problem for optimal vehicle speed control, a numerical solution is presented here [114]. The main idea is to find state $\boldsymbol{x_v}$ in a forward pass (utilizing the $\boldsymbol{\lambda_v}$ from the previous iteration) and then find $\boldsymbol{\lambda_v}$ in a backward pass. The procedure is summarized in the following:

Table 4-1 Numerical solution for the optimal control

**Algorithm**: numerical solution for the optimal control

1: Set the initial value of co-state $\boldsymbol{\Lambda}^{(0)}(t) = 0$ for $t \in [t_0, t_f]$.

Set $j = 1$.

2: *loop:*

3: Solve the state dynamic equations forward in time for $\boldsymbol{x}_v^{(j)}(t)$ using $\boldsymbol{\Lambda}^{(j-1)}$ computed from the previous iteration for $t \in [t_0, t_f]$.

4: Solve for the co-state $\boldsymbol{\lambda}_v^{(j)}(t)$ backward in time utilizing $\boldsymbol{x}_v^{(j)}(t)$.

5: Update $\boldsymbol{\Lambda}^{(j)}$ based on the co-state $\boldsymbol{\lambda}_v^{(j)}(t)$ and the co-state $\boldsymbol{\Lambda}^{(j-1)}$ from the previous iteration. $\alpha$ is a weighting factor that smooth the updating process.

$$\boldsymbol{\Lambda}^{(j)} = (1 - \alpha) \cdot \boldsymbol{\Lambda}^{(j-1)} + \alpha \cdot \boldsymbol{\lambda}_v^{(j)}$$

6: **if** $\left\| \boldsymbol{\Lambda}^{(j)} - \boldsymbol{\lambda}_v^{(j)} \right\| < \epsilon_{max}$ ($\epsilon_{max}$: a pre-set tolerance level)

$j = j + 1$

**goto** 3:

7: **else**

$\boldsymbol{x}_v^{(j)}(t)$ is the final optimal state trajectory.

*4.3.1.6. Following Preceding Vehicle: Solution Based on Nonlinear Programming*

The previous section solves the optimal control for scenarios where the target vehicle is not following a preceding vehicle. To handle car-following scenarios with car-following distance constraint (4.10), signal constraints (4.11) and speed bounds (4.8), an alternative control is designed based on nonlinear programming (NLP). The optimal control problem formulated in the previous sections is discretized and formulated as a NLP problem. As discussed in Chapter 1, this approach is effective in handling optimal control problems with state constraints. Efficient NLP solvers [32–35] can be used to solve the optimal control in real-time by taking advantage of the sparsity of the discretized problem. In this section, the optimal control problem is discretized using one-step Euler method. The Euler method is selected as it is simple and efficient enough for solving this optimization problem. More advanced and accurate pseudo-spectral method can be used to discretize the problem similarly as in Section 3.3.2. Assume the problem is discretized into $N$ partitions, the following discretized optimization problem is solved

$$\begin{aligned} \underset{d,v,a}{min} \quad & \phi(\boldsymbol{x}(N_{PH})) + \sum_{k=1}^{N-1} L(v(k), a(k)) \\ s.t. \quad & d(k+1) = d(k) + dt \cdot v(k) \\ & v(k+1) = v(k) + dt \cdot a(k) \\ & d(k) \geq d_p(k) - d_{max} \\ & d(k) \leq d_p(k) - \left(d_{min} + h_{min} \cdot v(k)\right) \\ & v_{min} \leq v(k) \leq v_{max} \\ & a_{min} \leq a(k) \leq a_{max} \\ & d(k_r) \geq d_{sig}, \qquad d\left(k_g\right) \leq d_{sig} \\ & d(1) = 0, v(1) = v_0 \end{aligned} \tag{4.22}$$

where $L(v(k), a(k))$ is defined as in (4.2).

Analytical gradient and Hessian are computed and provided to the NLP solver to reduce the computational burden. The gradient is as the following:

$$\frac{\partial L}{\partial d(k)} = \beta_1\left[-\mu mg \cdot sin\left(\varphi(k)\right) + mg \cdot cos(\varphi(k))\right] \cdot \frac{\partial \varphi}{\partial d} \cdot v(k) \tag{4.23}$$

$$\begin{aligned}\frac{\partial L}{\partial v(k)} = {} & \beta_1 \cdot \left[\mu mg \cos\left(\varphi(k)\right) + mg \sin\left(\varphi(k)\right)\right] + 3\beta_1 \cdot C_{wind} \cdot v^2(k) \\ & + \beta_1 \cdot m \cdot a(k) + 2w_1 \cdot (v(k) - v_{lim})\end{aligned} \tag{4.24}$$

$$\frac{\partial L}{\partial a(k)} = \beta_1 \cdot m \cdot v(k) + 2w_2 \cdot a(k) \tag{4.25}$$

Note that as indicated in (4.23), roadway slope angle $\varphi$ actually depends on the target vehicle's location $d$. $\partial\varphi/\partial d$ is the roadway slope changing rate with respect to the vehicle location. The Hessian matrix contains all the second partial derivatives of (4.23)-(4.25), that is

$$\begin{aligned}\frac{\partial^2 L}{\partial d(k)^2} = {} & \beta_1\left[-\mu mg\, cos\left(\varphi(k)\right) - mg\, sin(\varphi(k))\right] \cdot \left(\frac{\partial \varphi}{\partial d}\right)^2 \cdot v(k) \\ & + \beta_1\left[-\mu mg\, sin\left(\varphi(k)\right) + mg\, cos(\varphi(k))\right] \cdot \frac{\partial^2 \varphi}{\partial d^2} \cdot v(k)\end{aligned} \tag{4.26}$$

$$\frac{\partial^2 J}{\partial v(k)^2} = 6\beta_1 \cdot C_{wind} v(k) + 2w_1 \tag{4.27}$$

$$\frac{\partial^2 J}{\partial v(k)\partial a(k)} = \beta_1 m \tag{4.28}$$

$$\frac{\partial^2 J}{\partial a(k)^2} = 2w_2 \tag{4.29}$$

$$\frac{\partial^2 J}{\partial d(k)\partial v(k)} = \beta_1\left[-\mu mg \cdot sin\left(\varphi(k)\right) + mg \cdot cos(\varphi(k))\right] \cdot \frac{\partial \varphi}{\partial d} \tag{4.30}$$

$$\frac{\partial^2 J}{\partial d(k)\partial a(k)} = 0 \tag{4.31}$$

With these analytical gradients and hessians, the optimization problem is real-time implementable using an efficient interior-point nonlinear programming solver [52]. This optimization can be implemented in a model predictive control fashion with traffic prediction similarly as in Section 2.2.

### 4.3.2. Powertrain Level Optimization

As shown in Figure 4.1, step 2 is the powertrain level optimization. The powertrain model of the HEV in this work is based on the Toyota Hybrid System (THS) architecture [105,115]. The inputs to the model are passed on from the vehicle level optimization, which include grade angles, vehicle speed and acceleration trajectories. Both the power-split between the engine and the battery, and the engine operating point are optimized to minimize fuel consumption. The optimal control problem is solved using the PMP approach. The solving approach is extended from previous work [105]. In the previous work, the road terrain was assumed to be level. This work takes one step further to include the effect of different terrain angles in the optimization.

*4.3.2.1. State Equation*

For the HEV powertrain dynamic model, the state is the battery SOC level, and the control input is battery power $P_{batt}$. The state dynamics is

$$\dot{SOC}(t) = -\frac{V_{oc} - \sqrt{V_{oc}^2 - 4R_{batt}P_{batt}(t)}}{2R_{batt}Q_{batt}} \tag{4.32}$$

where $V_{oc}$ is the open-circuit battery voltage, $R_{batt}$ is the battery resistance, and $Q_{batt}$ is the battery capacity in $(A \cdot sec)$. In reality, these variables depend on the current battery SOC level. These variables are considered as constants since change of SOC is relatively small during the optimization horizon.

*4.3.2.2. Powertrain Model*

The static powertrain model is shown as the following [101,105]

$$F_t(t) = T_v(t)/r_r \tag{4.33}$$

$$\omega_m(t) = K \cdot v(t)/r_r \tag{4.34}$$

$$\omega_e(t) \cdot (R + S) = \omega_g(t) \cdot S + \omega_m(t) \cdot R \tag{4.35}$$

$$T_m(t) = \frac{T_v(t)}{K} - T_e(t) \cdot \left(\frac{R}{R + S}\right) \tag{4.36}$$

$$T_g(t) = -T_e(t) \cdot \left(\frac{S}{R + S}\right) \tag{4.37}$$

where $F_t$ is the thrust force and is as (4.6); $T_v$ is the vehicle thrust torque; $\omega_m$ is the motor speed; $T_m$ is the motor torque; $\omega_g$ is the generator speed; $T_g$ is the generator torque; $K$ is the gear ratio between the motor and the vehicle driveline shaft; $R$ is the radius of the ring gear; $S$ is the radius of the sun gear.

The net power of the motor and the generator determines the battery power [101,105]

$$P_{batt}(t) = \eta_m^{k_m} \cdot \omega_m(t) T_m(t) + \eta_g^{k_g} \cdot \omega_g(t) T_g(t) \tag{4.38}$$

where $\eta_m$ and $\eta_g$ are the efficiency of the motor and the generator; $k_m = 1$ when $\omega_m T_m$ is positive; $k_m = -1$ when $\omega_m T_m$ is negative; $k_g = 1$ when $\omega_g T_g$ is positive; $k_g = -1$ when $\omega_g T_g$ is negative.

*4.3.2.3. Objective Function*

The cost function is defined as

$$J = \psi_3 \cdot \left(SOC(t_f) - SOC_f\right) + \int_{t_0}^{t_f} \dot{m}_{fuel}(v, a, \varphi, P_{batt}) dt \tag{4.39}$$

where the first term is the terminal constraint. The terminal constraint is to ensure that $SOC(t_f)$ reaches the desired $SOC_f$ at the end of the time horizon to maintain charge sustaining. The fuel consumption rate $\dot{m}_{fuel}$ is modeled as

$$\dot{m}_{fuel} = a_o(v, a, \varphi) P_{batt}(t) + b_o(v, a, \varphi), \forall\, t \in [t_0, t_f] \tag{4.40}$$

where $a_o$ and $b_o$ are two mappings that were acquired for vehicle speed between [0 m/s, 26.82 m/s] ([0 mph, 60 mph]), vehicle acceleration between [-6.71 m/s2, 6.71 m/s2] ([-15 mph/s, 15 mph/s]) and grade angle between [-0.27 rad, 0.27 rad]. Efforts were made to reduce computational complexity:

- *Problem order reduction*. As shown in Section 4.3.2.2, the optimization was originally a two-level optimization for both power-split and engine operating point. It was downgraded by pre-pairing the engine operating point $(T_e, \omega_e)$ with a given set of input information (altitude, speed and acceleration) and battery power $P_{batt}$. The pre-paired engine operating point $(T_e, \omega_e)$ was selected as that gave the lowest fuel consumption rate $\dot{m}_{fuel}$.

- *Linearization.* The relation between $\dot{m}_{fuel}$ and $P_{batt}$ is linearized as $\dot{m}_{fuel} = a_o P_{batt} + b_o$. The entire coefficient sets $(a_o, b_o)$ are formed as two mappings, acquired using engine map data and the vehicle longitudinal dynamics model. $a_o$ represents the decrease rate in fuel consumption when choosing different battery power for a given vehicle power demand, and $b_o$ is the fuel consumption when battery outputs no power.
- *Pre-determined mappings.* The two $a_o$ and $b_o$ mappings are pre-calculated offline at different vehicle power demand with different vehicle speed, acceleration and grade. The results are stored in the controller. During the optimization process, the controller refers to these mappings for information, instead of calculating in real-time. Changes in grade do not affect shapes, but shift $a_o$ mapping along the vehicle acceleration axis (Figure 4.3).

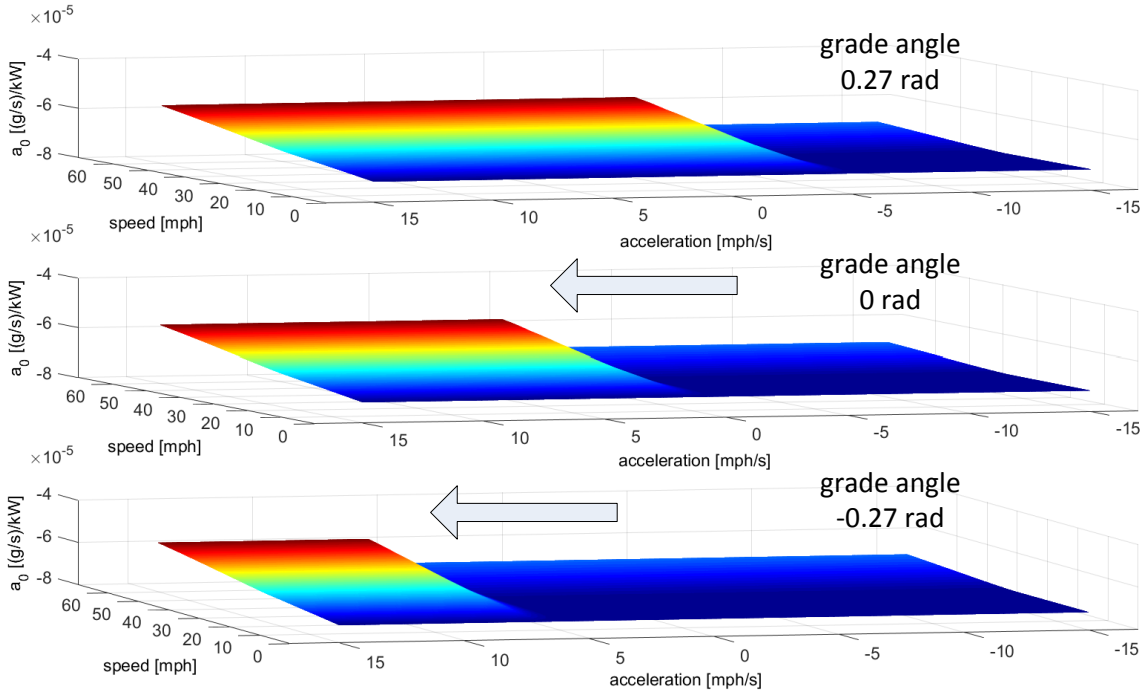


Figure 4.3 Grade angle affects the $a_0$ mapping in the fuel consumption model.

*4.3.2.4. Constraints and Initial Conditions*

The maximum power that the battery can provide is limited by the capacity of the battery, that is

$$\mathcal{U}_p = \left\{P_{batt} \middle| P_{batt} \leq V_{oc}^2/4R_{batt}, \forall t \in [t_0, t_f]\right\} \tag{4.41}$$

Initially, the battery SOC level is assumed to be

$$SOC(t_0) = SOC_0 \tag{4.42}$$

*4.3.2.5. Solution Based on Pontryagin's Minimum Principle*

The solving method for the powertrain level optimization is similar to what was demonstrated in Section 4.3.1.5. With the state dynamics and cost function, the Hamiltonian can be expressed as

$$\mathcal{H}_p = a_o(v, a, \varphi)P_{batt}(t) + b_o(v, a, \varphi) + \lambda_3\left(-\frac{V_{oc} - \sqrt{V_{oc}^2 - 4R_{batt}P_{batt}(t)}}{2R_{batt}Q_{batt}}\right) \tag{4.43}$$

where $\lambda_3$ is the costate. Given the necessary conditions for solving the optimal control

$$\begin{cases} \dot{\lambda}_3 = -\dfrac{\partial \mathcal{H}_p}{\partial SOC} = 0 \\ \dfrac{\partial \mathcal{H}_p}{\partial P_{batt}} = a_o(v, a, \varphi) - \dfrac{\lambda_3}{Q_{batt}\sqrt{V_{oc}^2 - 4R_{batt}P_{batt}(t)}} = 0 \\ \lambda_3(t_f) = w_5 \end{cases} \tag{4.44}$$

To find out the value of $\lambda_3$, charge-sustaining condition is applied. The sum of $\dot{SOC}(t)$ at the end of the optimization should be zero to guarantee charge-sustaining. Therefore, the co-state can be found as:

$$\lambda_3 = 2Q_{batt}^2 R_{batt}\left[\sum_{t_0}^{t_f - dt}\left(\frac{1}{a_o(t)}\right)\right]^{-1}\left[\left(\frac{t_f - t_0}{dt}\right)\frac{V_{oc}}{2R_{batt}Q_{batt}}\right] \tag{4.45}$$

Therefore, from the necessary conditions, the optimal control input $P_{batt}$ can be found as:

$$P_{batt}(t) = \frac{1}{4R_{batt}}\left[V_{OC}^2 - \left(\frac{\lambda_3}{a_o(t)Q_{batt}}\right)^2\right] \tag{4.46}$$

With the above method, the optimal battery power $P_{batt}$ can be calculated from the grade angles, dynamic speed limit, vehicle speed and acceleration trajectories from the vehicle level optimization.

*4.3.2.6. Solving Process*

The charge-sustaining condition gives an analytical solution for the co-state. As a result, the control input $P_{batt}$ is found analytically instead of using iteration process. This reduces computational burden. When $P_{batt}$ is determined, the engine operating point $(T_e, \omega_e)$ is selected as the ones that give the minimal fuel consumption. As mentioned in [105], the computational burden of the optimization is low. This method can potentially be used in real-time.

## 4.4. Simulation Evaluation

In this section, the proposed vehicle speed and powertrain operation optimization controller is evaluated in two scenarios: a rolling terrain scenario with no nearby preceding vehicle and an urban drive scenario where the target vehicle follows a preceding vehicle to pass an intersection (eco-approach). The following assumptions are made for the evaluation:

- Time step is 0.1 second;
- $\psi_1$ and $\psi_2$ are large positive numbers which ensure a constraint on vehicle's final state; $w_1 = 0.05$; and $w_2 = 0.1$;
- Fuel consumption coefficients $\beta_0 = 0.037$; $\beta_1 = 6.7 \times 10^{-5}$;
- Drag coefficients $\mu = 0.00475$; $C_{wind} = 0.36$;$m = 1400$;
- Acceleration range is [-5, 3] $m/s^2$;
- The battery *SOC* level is charge-sustained at the end in order to have a fair comparison.

### 4.4.1. Rolling Terrain Scenario

The first scenario is rolling terrain where there is no nearby preceding vehicle and the optimal control is solved as in Section 4.3.1.5 using PMP. In order to represent the real world scenario, two types of road are selected as stereotypes, a major arterial and a collector road. The grades assigned to each road type follow the recommendation from the "Green Book" [116]. Sensitivity study was conducted with regard to two factors of the rolling terrain: density and intensity. Density is represented by the length of each up/down hill. The longer the up hills, the denser the hills are. Intensity is represented by the grade of each up/down hill. The higher the grade, the more intense the hills are. The following is the design specifications of two road types:

- *Major arterial*: A speed limit of 55 *mph*, with maximal grade intensity of 6%
- *Collector road*: A speed limit of 35 *mph*, with maximal grade intensity of 15%.

For each road type, two hill density cases are constructed, 400 ft. (uphill length) and 800 ft. (uphill length). The hills are repeated continuously throughout each road. In total, four terrain scenarios are simulated. For each scenario, simulation time is 400 seconds and the initial target vehicle speed equals to the speed limit of the terrain type. The initial location is defined as 0 meter and the initial SOC level is 0.6. It is assumed that slope is constant within one time step. It is reasonable since each time step is one tenth of a second. The distance a vehicle could travel within such short time can have little variation on slope.

*4.4.1.1. Controller Types*

The fuel efficiency will be improved on two levels: vehicle level and powertrain level. The two-level integrated optimal controller is not only compared against the constant-speed cruise-control case for a quantitative evaluation, it is also compared against other individual level optimal controllers to demonstrate the marginal benefit brought by the integration. The purpose of these comparisons is to reveal the advantage

of co-optimization. For the scenarios that are not optimized for powertrain control, a rule-based battery controller is adopted. To ensure charge-sustaining in the rule-based method, the battery is set to start charging or discharging to the initial SOC level during the last 10 seconds of the simulation. Detailed information about this rule-based controller is discussed in [105]. The scenarios are listed in the following:

- *Baseline*: A vehicle cruises constant speed at speed limit with rule-based controller.
- *Speed Optimization*: A vehicle travels at optimized speed with rule-based controller. In this case, only speed trajectory is optimized. The powertrain is operating under the rule-based controller.
- *Powertrain Optimizati*on: A vehicle cruises at speed limit with powertrain control optimized. In this case, only power-split and engine operating point are optimized. The vehicle travels at the speed limit.
- *Integrated Optimization*: A vehicle travels at optimized speed with optimized powertrain control.

*4.4.1.2. Fuel Consumption Calculation*

The final product of a controller includes a trajectory of engine operating point. The fuel consumption is found by referring to an engine map [105]. The summation of the instantaneous fuel consumption gives the cumulative fuel consumption.

*4.4.1.3. Simulation Results*

The results are presented in this section. They confirm that the integrated optimal controller is superior to the other two individual level controllers (speed and powertrain optimization). The integrated optimal controller not only improves fuel consumption benefits, but also achieves a comfortable driving experience with desired mobility.

The computing time for the optimization is 19.9 seconds, given a 400 second optimization time horizon. The program was performed on a computer with i5 CPU @ 2.67 GHz and 8GB memory. It indicates the proposed optimal controller can potentially be used for real-time applications.

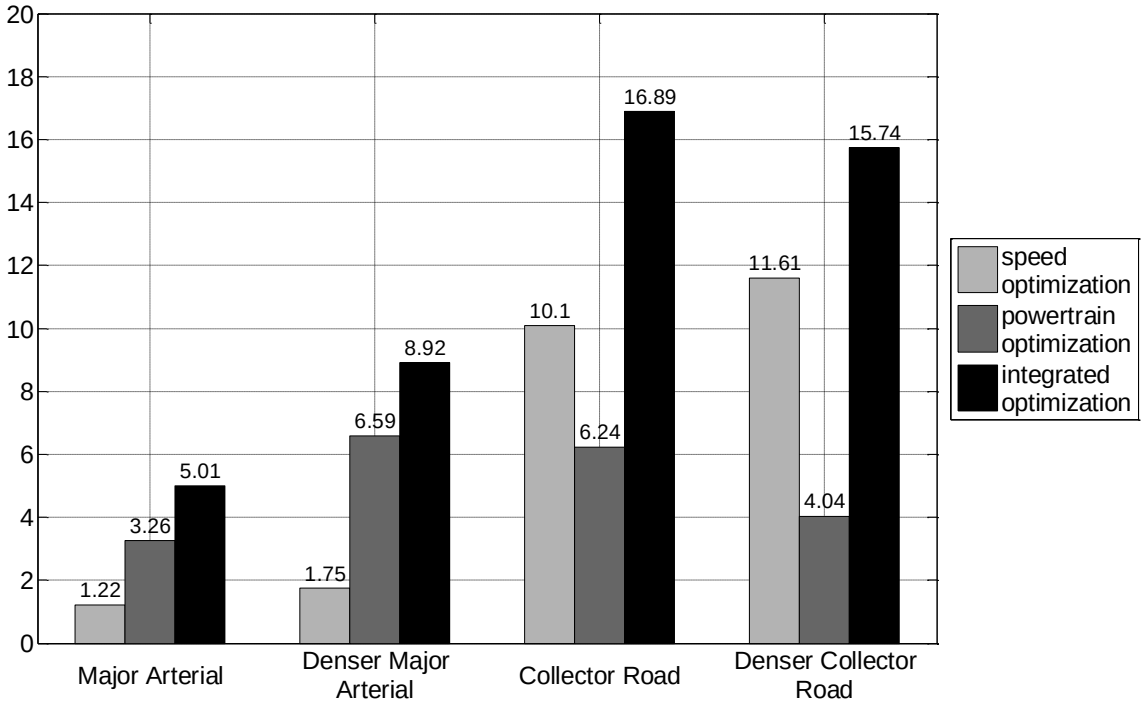


Figure 4.4 Fuel consumption benefits (%).

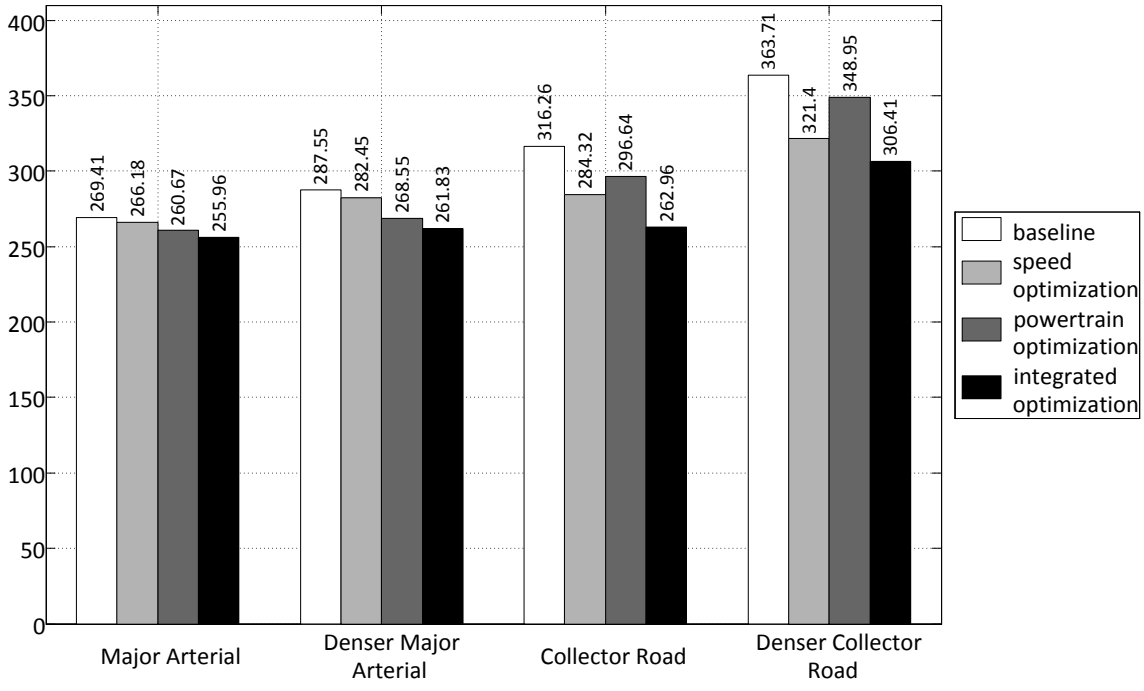


Figure 4.5 Cumulative fuel consumption (gram).

Figure 4.4 and Figure 4.5 show the fuel consumption benefits comparison among the integrated controller, individual optimizations, and the baseline on all four road

topographies. The proposed integrated optimal controller demonstrates the most fuel savings. The value of the saving is generally the summation of the savings of two individual level controllers. This indicates that the two individual optimizations have minimal conflict with each other. The fuel savings of the integrated optimization and the speed optimization are higher on steeper roads. While the powertrain optimization shows relatively constant fuel savings. The effect of grade density depends on intensity of grade. On major arterial roads, the fuel consumption benefits of the proposed optimal controller increases in denser-located-hills scenario, while a decrease is observed on collector roads.

Figure 4.6 and Figure 4.7 show the optimized speed profile, terrain altitude profile, cumulative fuel consumption, and battery SOC level for major arterials and collector roads respectively. The results all make sense. In all the four terrain scenarios, the optimized speed profile has a periodic pattern as the grade angle changes. The vehicle accelerates as the grade angle decreasing, and decelerates as the grade angle increasing. The penalty on mobility and comfort in the cost function keeps the speed from deviating too much from the speed limit.

The speed shows more variations in more intensive terrain cases. The major arterial scenarios (with 6% max grade angle) have speed variations of about 1.1 mph, while the collector road scenarios (with 15% max grade angle) have speed variations of about 3.1 mph. This is reasonable, because to maintain a constant speed on collector roads, it requires more power when climbing uphills and brakes more (loss more kinetic energy to heat) when traveling downhills. To be noted, in all the scenarios, the speed variations are within the safe range ($\pm 5$ mph).

The vehicle level optimization brings more significant fuel consumption benefits on collector roads. The larger speed variations contribute to this observation. The speed decrease on uphill reduces the power required to climb up the hill. The more the speed deviates from speed limit, the less the power is needed. The less the power needed, the more the fuel is saved.

SOC are all charge-sustained. This guarantees a fair comparison. Without future altitude information, the rule-based controller tends to accumulate battery energy. It only applies part of the battery energy gained from downhill to uphill climbing. Note that before the end of simulation, the battery discharges to ensure charge-sustaining.

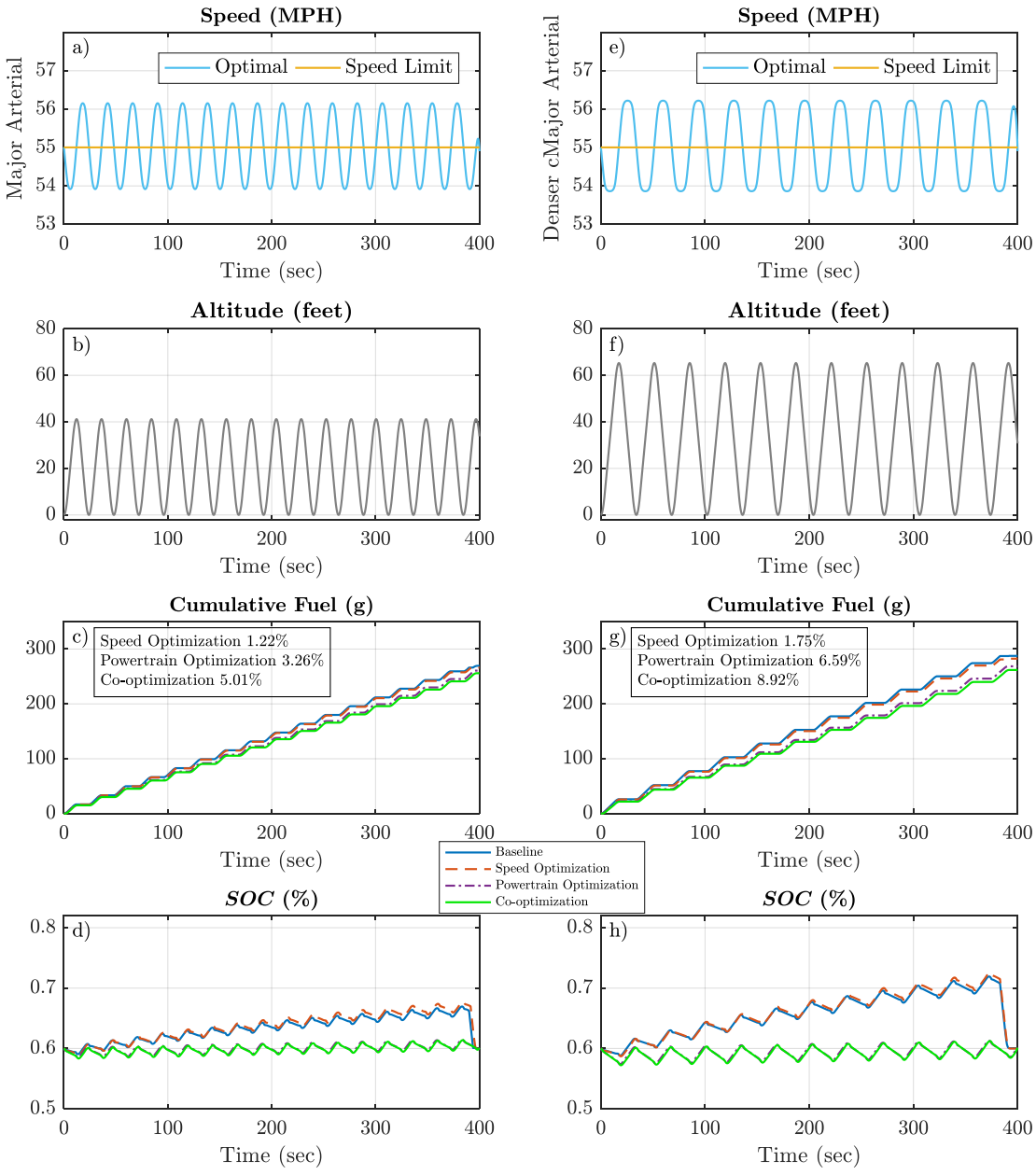


Figure 4.6 Optimized speed, altitude, cumulative fuel consumption, and battery SOC level for major arterials.

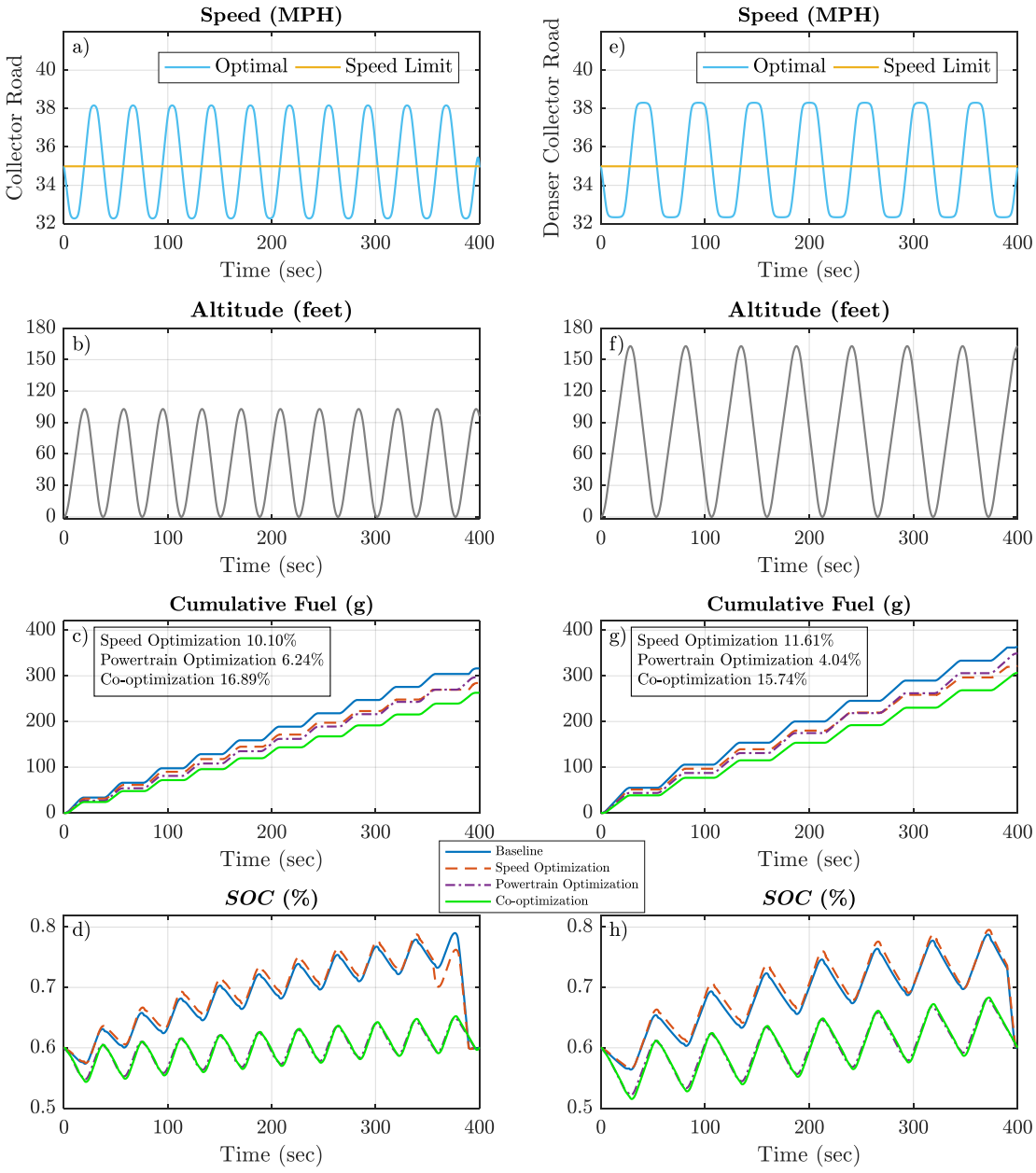


Figure 4.7 Optimized speed, altitude, cumulative fuel consumption, and battery SOC level for collector roads.

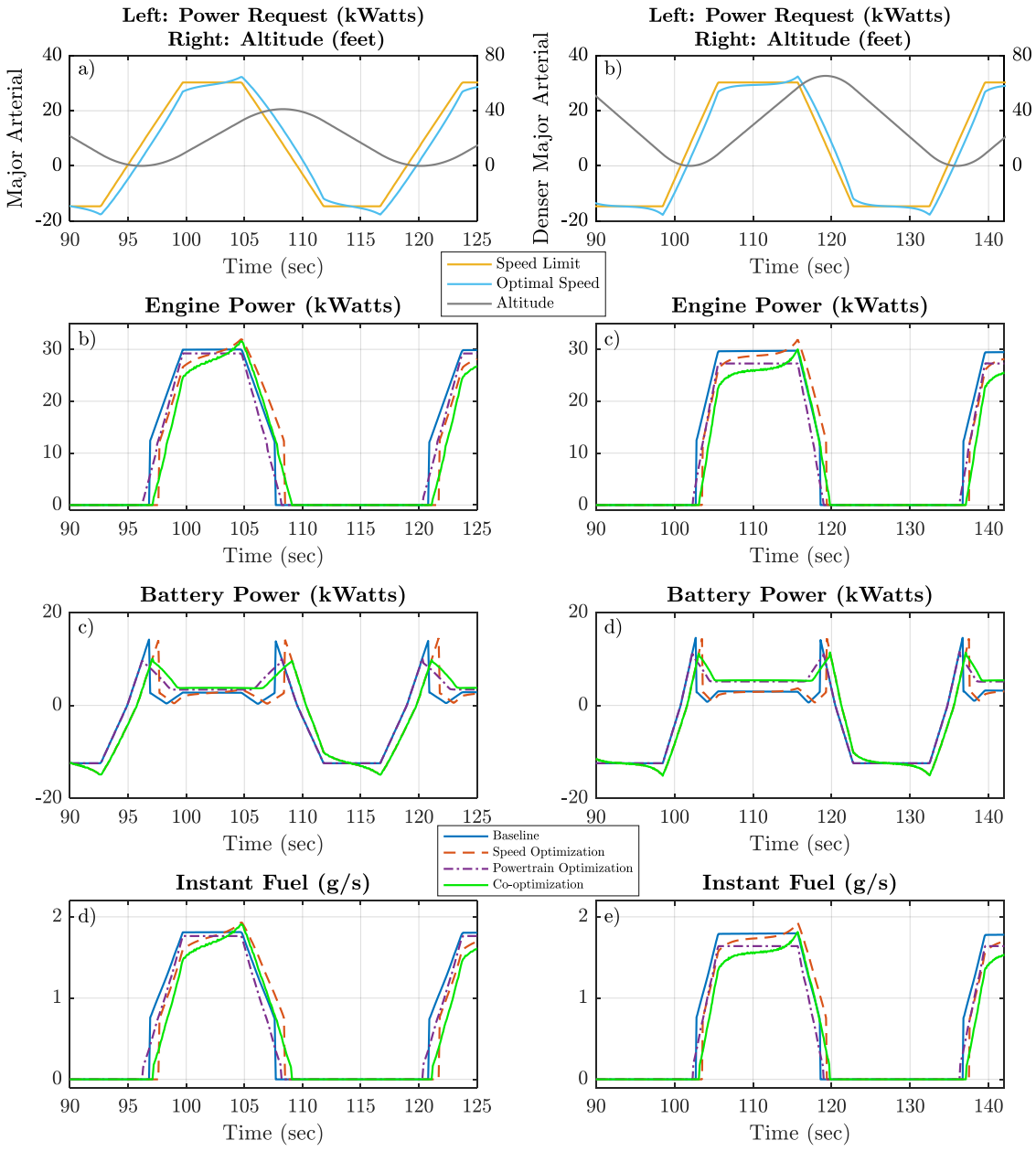


Figure 4.8 Power request, engine power, battery power, and instantaneous fuel consumption for major arterials (zoomed to one hill climbing).

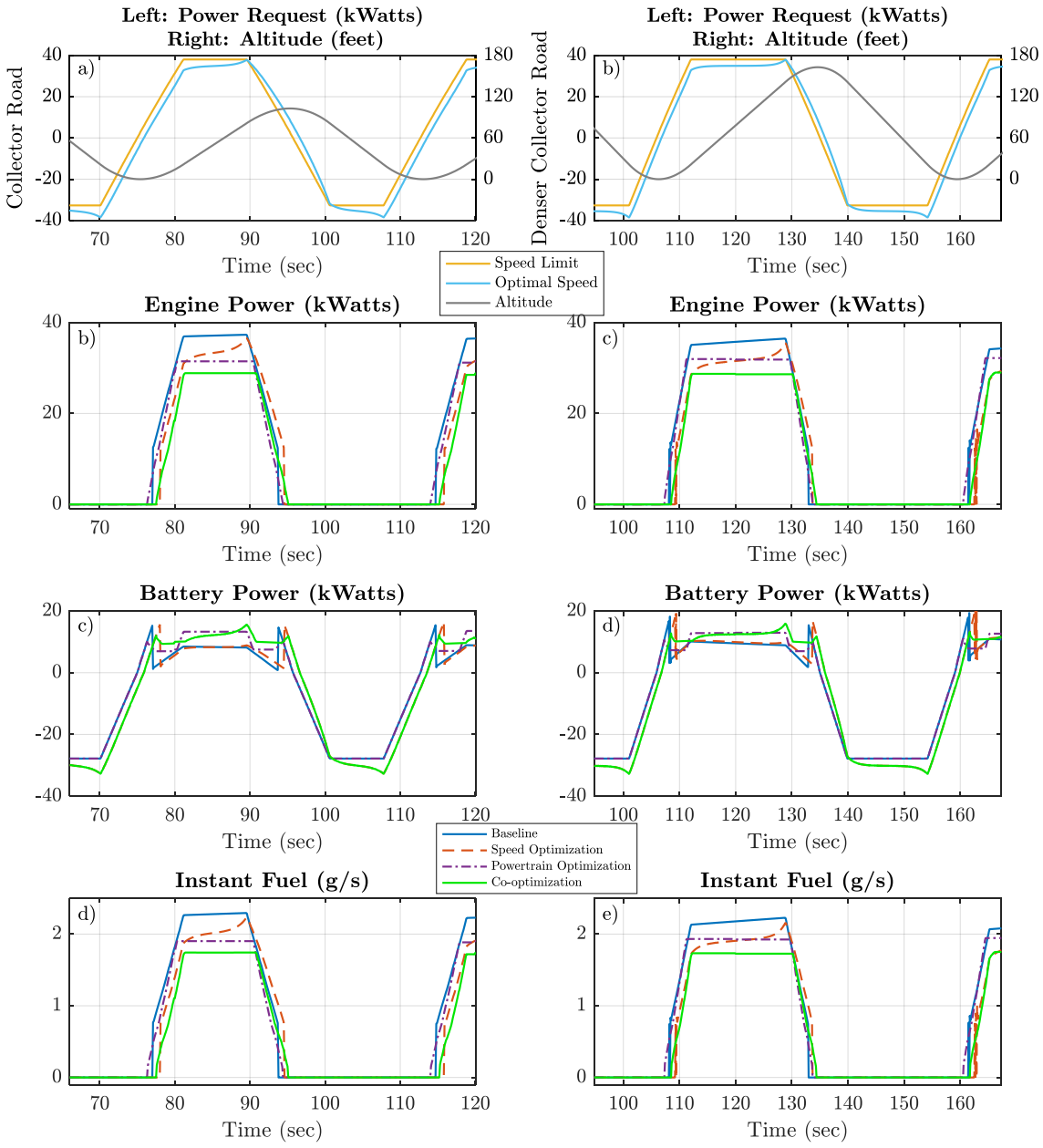


Figure 4.9 Power request, engine power, battery power, and instantaneous fuel consumption for collector roads (zoomed to one hill climbing).

Figure 4.8 and Figure 4.9 show the power request, engine power, battery power, and instantaneous fuel consumption of the vehicle climbing up and climbing down one hill for major arterials and collector roads respectively.

The integrated optimization ensures that the engine is always operating in the most efficient region (around 25 kWatt to 30 kWatt, as shown in Figure 4.2). This leads to the increase of fuel savings on the collector roads. As observed from Figure 4.8 and Figure 4.9, power request peaks when the speed begin to increase as the grade angle decreases. On collector roads, the battery produces the extra energy to meet the peak power request. On the major arterial, the controller uses engine to provide the extra energy. Consequently, in both scenarios, the engine always operates in the most efficient region. The battery is sufficiently charged during downhill traveling.

The powertrain optimization has similar fuel consumption benefits among various road topographies. A key benefit of the powertrain level optimization is that it is unnoticeable to the driver and can be implemented even with low penetration of connected vehicles.

The proposed optimal controller has two time horizons: prediction horizon and update horizon. The prediction horizon is the look-ahead time distance. The update horizon represents the frequency input information is updated and corrected. Update horizon can only be greater than or equal to the computation time. Figure 4.10 presents computation time of various prediction horizons and time step sizes. The prediction horizon is 400 seconds in the sample study since it is constrained by the associated computation time (about 20 seconds). Twenty seconds update time is chosen as the upper limit for a real-time application in this research. Future users could refer to this chart to determine their own prediction horizon. Figure 4.10 also demonstrates the real-time potential of the proposed optimal controller.

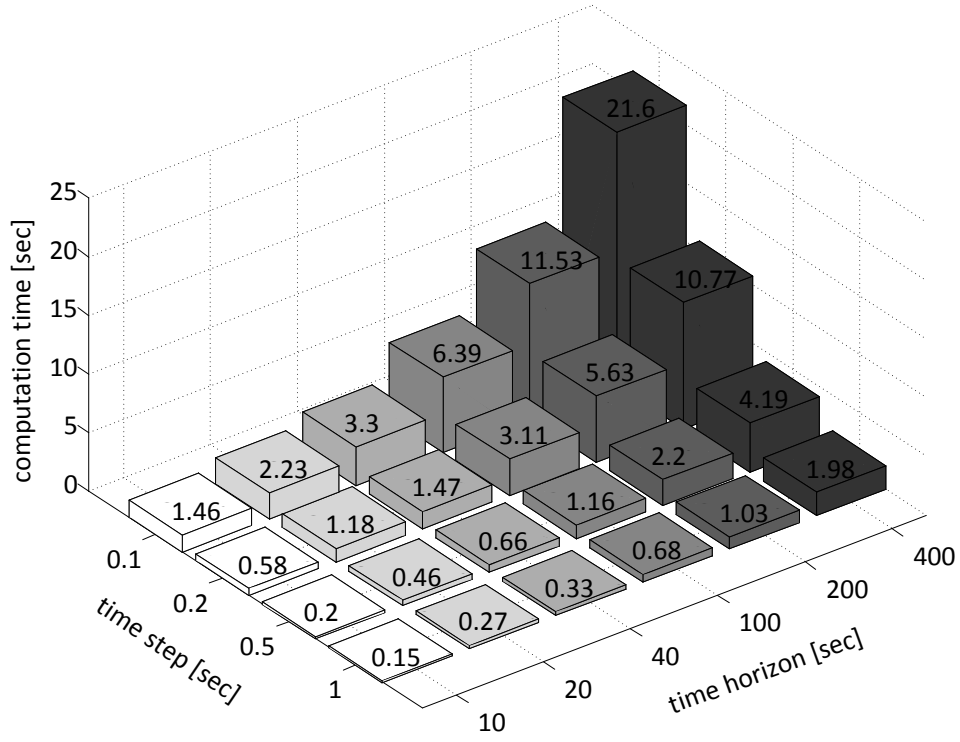


Figure 4.10 Computation time of various prediction horizon and time step size.

*4.4.1.4. Uncertainties consideration*

The proposed optimal controller is tested for its robustness under realistic condition where its input information is with mismatch and stochastic perturbation. Two factors are evaluated:

- Grade uncertainty: discrepancy between designed grade and constructed grade. The uncertainty is assumed to be uniformly distributed in the range of [-5%, 5%] of the maximal grade intensity [117].
- GPS positioning uncertainty: discrepancy between position from GPS and the actual position. It is assumed to be normally distributed with standard deviation of 3.9 m and mean of 0 m [118].

The following figure shows an example of difference between received grade and actual grade. In this case, the discrepancy between the received position and actual position is 7.8 m.

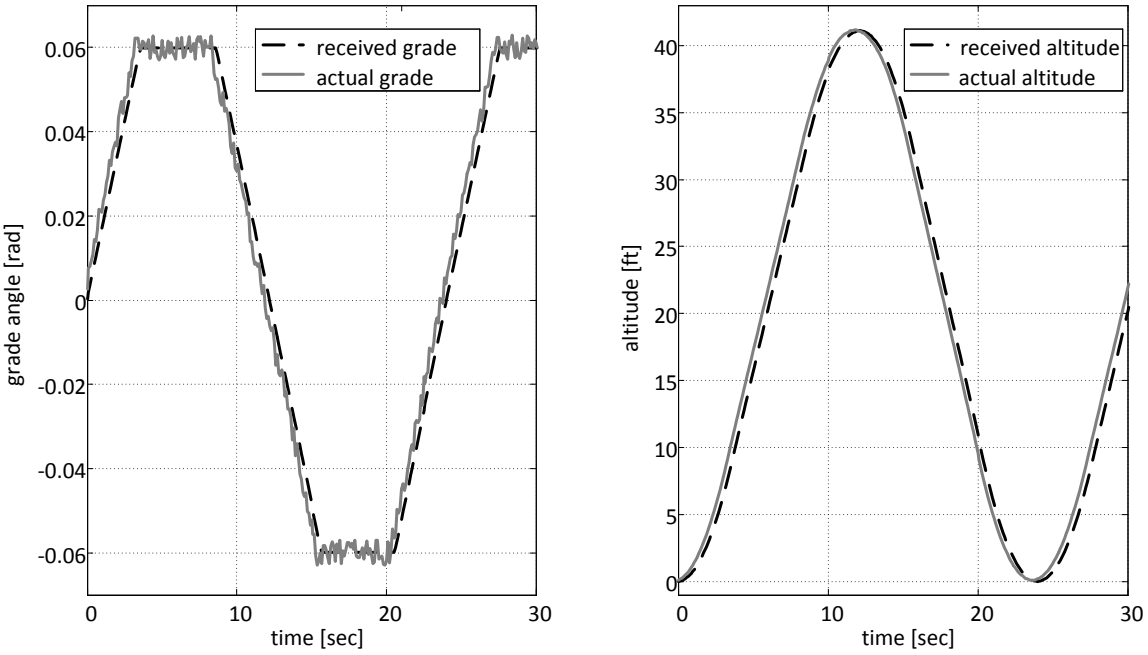


Figure 4.11 Difference between received grade and actual grade (major arterial case).

The proposed controller is evaluated under the same assumptions stated at the beginning of Section 4.4. Additionally, the optimal controller follows the same optimal $P_{batt}$ and changes other powertrain states to maintain the optimal speed trajectory. Additionally, it is assumed that the input grade and position information is updated every 10 sec.

Figure 4.12-Figure 4.15 present the performance of the optimal controller with the consideration of grade and GPS perturbations. The results show that the fuel consumption benefits decrease from [5.01%, 15.74%] (no perturbation) to [1.77%, 13.27%] (grade perturbation only) and [0.8%, 12.52%] (grade + GPS perturbation).

Note that fuel consumption of the baseline controller also changes under perturbations. For the baseline case, rule-based $P_{batt}$ is allowed to change to maintain speed under perturbations. While for the integrated controller, optimal $P_{batt}$ follows previous optimized trajectory. Nevertheless, the proposed integrated optimal controller is

always beneficial compared to both individual optimal controllers and baseline controller under all road scenarios.

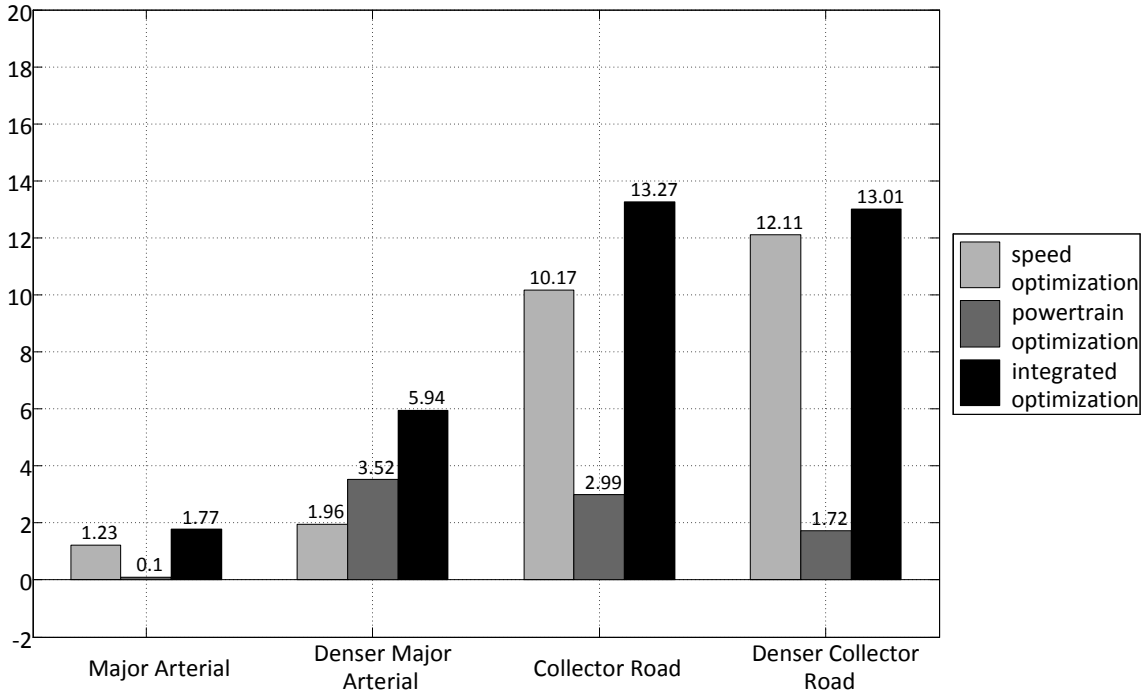


Figure 4.12 Fuel consumption benefits (with grade uncertainty)

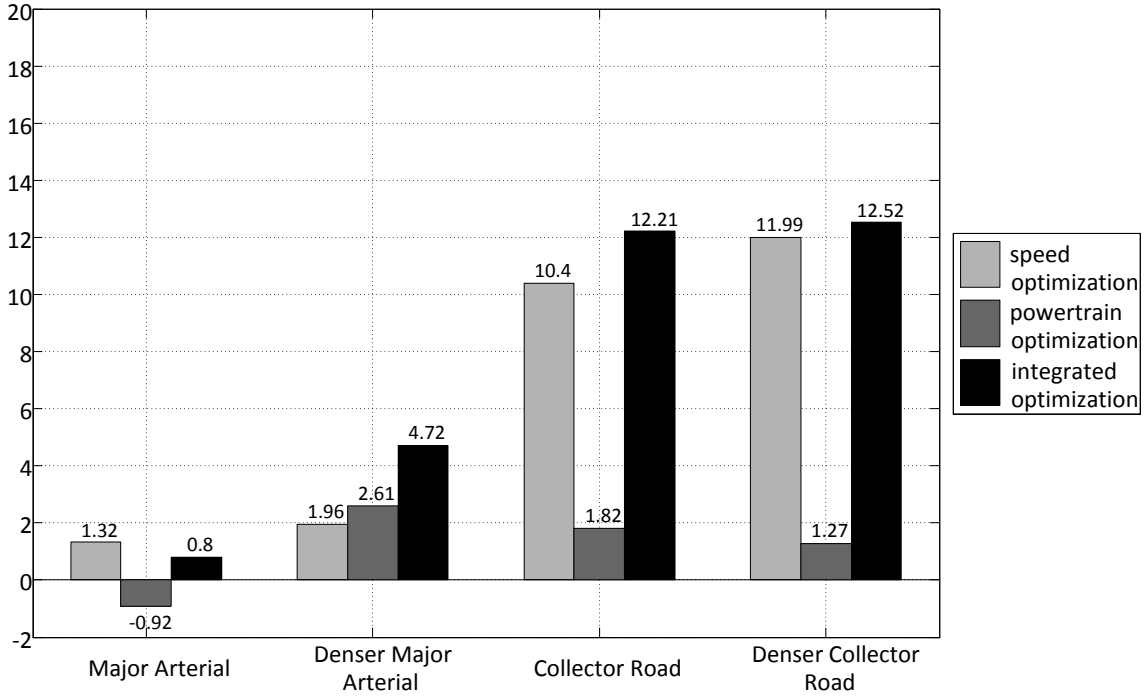


Figure 4.13 Fuel consumption benefits (with grade uncertainty plus GPS uncertainty)

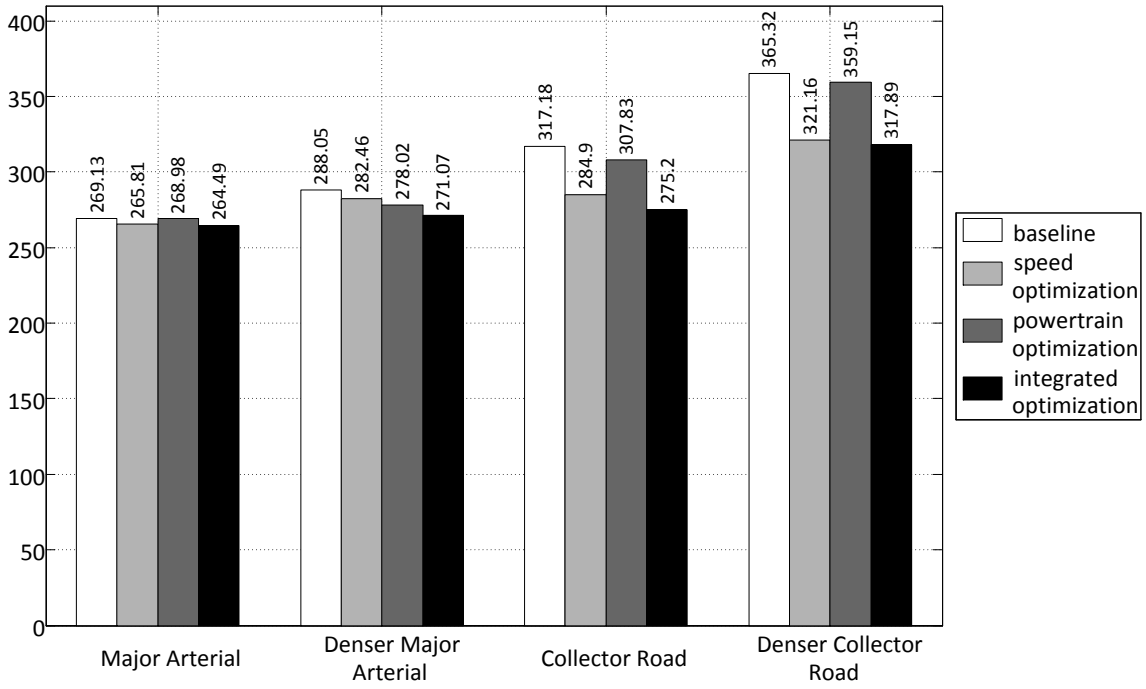


Figure 4.14 Fuel consumption (with grade uncertainty)

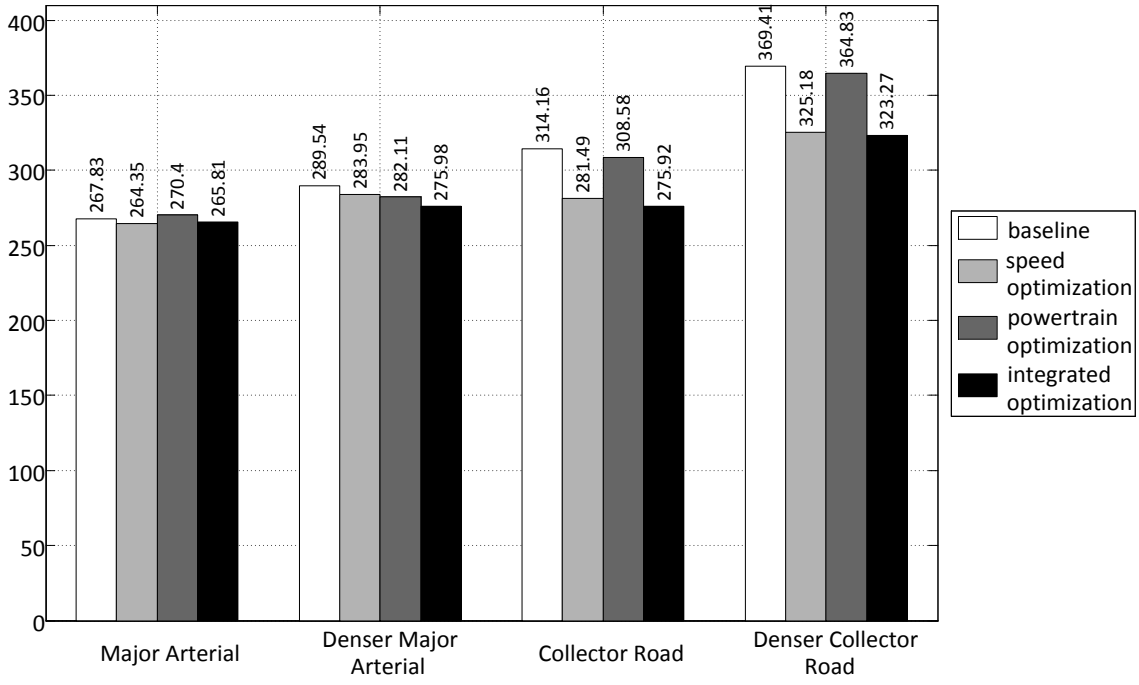


Figure 4.15 Fuel consumption (with grade uncertainty plus GPS uncertainty)

### 4.4.2. Eco-approach Scenario with Real-Traffic Data

*4.4.2.1. Scenario*

The second simulation scenario is an eco-approach application. The target vehicle follows a preceding vehicle to pass the intersection. The optimal control is solved as in Section 4.3.1.6. To generate a realistic traffic scenario, the living lab is used (Section 6.3). Firstly, field test was conducted on the TH55 as a human driver approaches the instrumented intersection. The on-board unit (OBU) on the on-road testing vehicle records the vehicle trajectories and the traffic signal information received from the roadside unit (RSU). This on-road testing vehicle is considered as the preceding vehicle. Next, the vehicle speed and powertrain operation optimization algorithms are implemented in a consecutive order. The vehicle dynamics controller (Section 4.3.1.6) solves an optimal vehicle acceleration trajectory by using the preceding vehicle's trajectory and the signal information. The optimal acceleration profile is sent to the powertrain controller (Section 4.3.2) to optimize engine operating points and the power-split simultaneously. In this section, to focus on demonstrating the capability of the optimal control, it is assumed that the target vehicle knows perfectly the future signal phase and timing, and the preceding vehicle's trajectory. As future work, this optimal control method can be extended to use the predicted traffic information following the framework shown in Chapter 2. Also, HIL testbed experiment can be conducted (similar as in Section 3.4) to validate the optimal control strategy using vehicle and powertrain models of a HEV (such as [119]). The corresponding fuel consumption and emissions can thus be accurately measured and compared.

*4.4.2.2. Simulation Results*

Simulation results are shown in Figure 4.16 and Figure 4.17. In Figure 4.16, both vehicles are using a rule-based (heuristic) powertrain controller while the target vehicle's speed is optimized. In Figure 4.17, the preceding vehicle uses an optimal powertrain controller while the target vehicle's speed and powertrain operation are co-optimized.

Figure 4.16a and Figure 4.16b show that, at first, without traffic signal information, the preceding vehicle accelerates and then decelerates when the vehicle is within a comfortable stopping distance to the red traffic signal. In contrast, the target vehicle knows when the signal will turn green, and therefore maintains its speed. It then decelerates slowly, while maintaining an appropriate following distance, before accelerating when the signal turns green. Without knowing future signal information, the preceding vehicle's performance is constrained based on current information, which forces it to be reactive and decelerates more when the signal is red. The target vehicle accelerates and decelerates less than the preceding vehicle, hence requiring less power as reflected by the lower engine and battery power (Figure 4.16f and Figure 4.16g).

The effects of powertrain optimization can be seen by comparing Figure 4.16 and Figure 4.17. As observed, with powertrain operation optimization, the engine speeds in Figure 4.17d are generally lower than those in Figure 4.16d. In addition, engine idling is also either eliminated or minimized, as can be seen from Figure 4.16c and Figure 4.17c. These correspond to more efficient engine operating regions, which result in better fuel economy for both vehicles (Figure 4.17e) compared to vehicle dynamics optimization only (Figure 4.16e). Moreover, Figure 4.16h and Figure 4.17h show that for both vehicles, at the beginning of the cycle, the optimal powertrain controller uses more battery to propel the vehicle since it anticipates a future braking event that will replenish the battery charge.

Figure 4.18 and Figure 4.19 shows a comparison of fuel consumption and fuel benefits. With vehicle dynamics and powertrain operation co-optimization, the target vehicle fuel saving is about 23 percent compared to the preceding vehicle. The vehicle dynamics optimization brings the target vehicle about 17 percent fuel saving. Furthermore, with powertrain operation optimization, the preceding vehicle can also achieve about 10 percent fuel improvement.

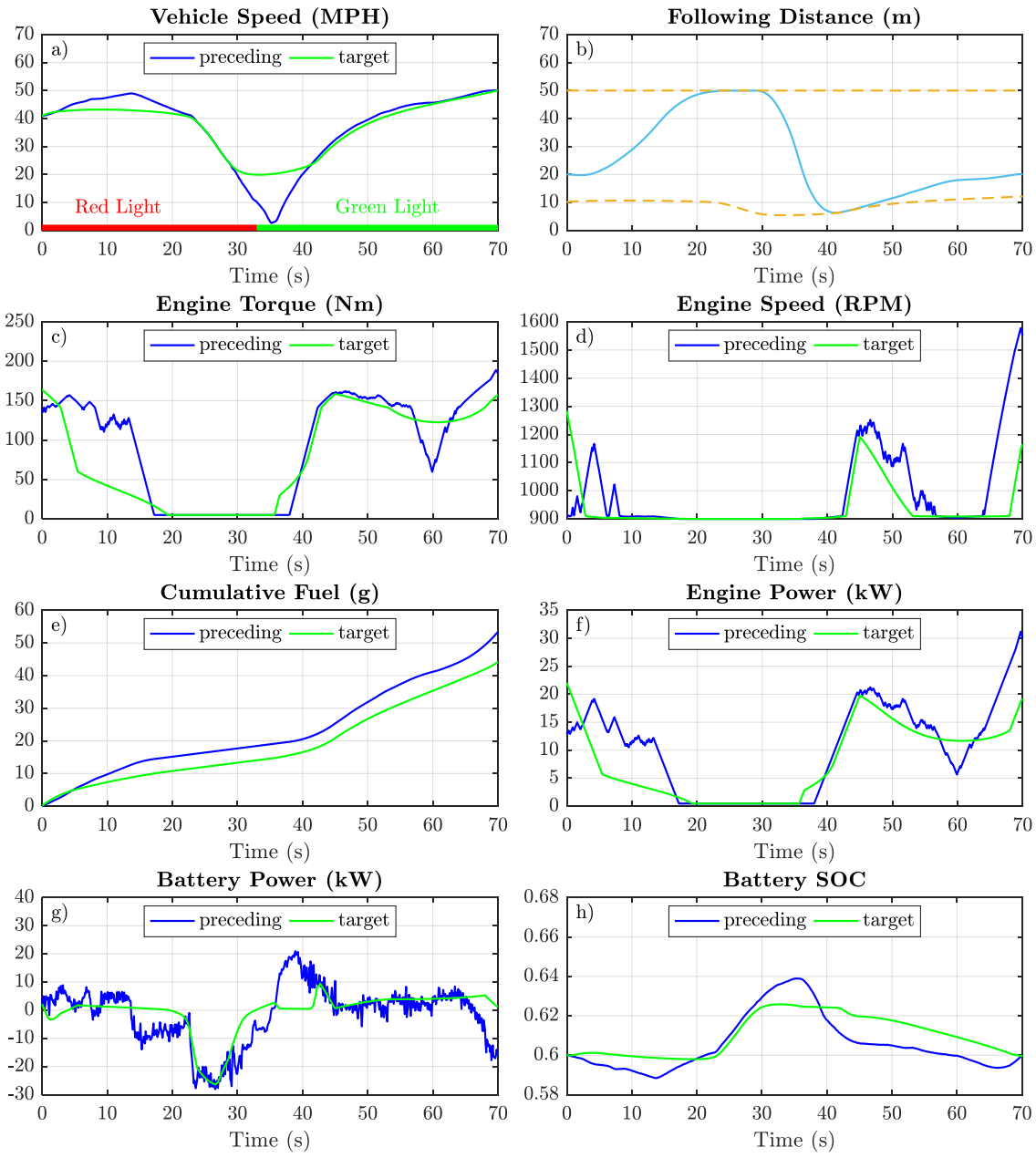


Figure 4.16 Vehicles and powertrain dynamics with rule-based powertrain controller

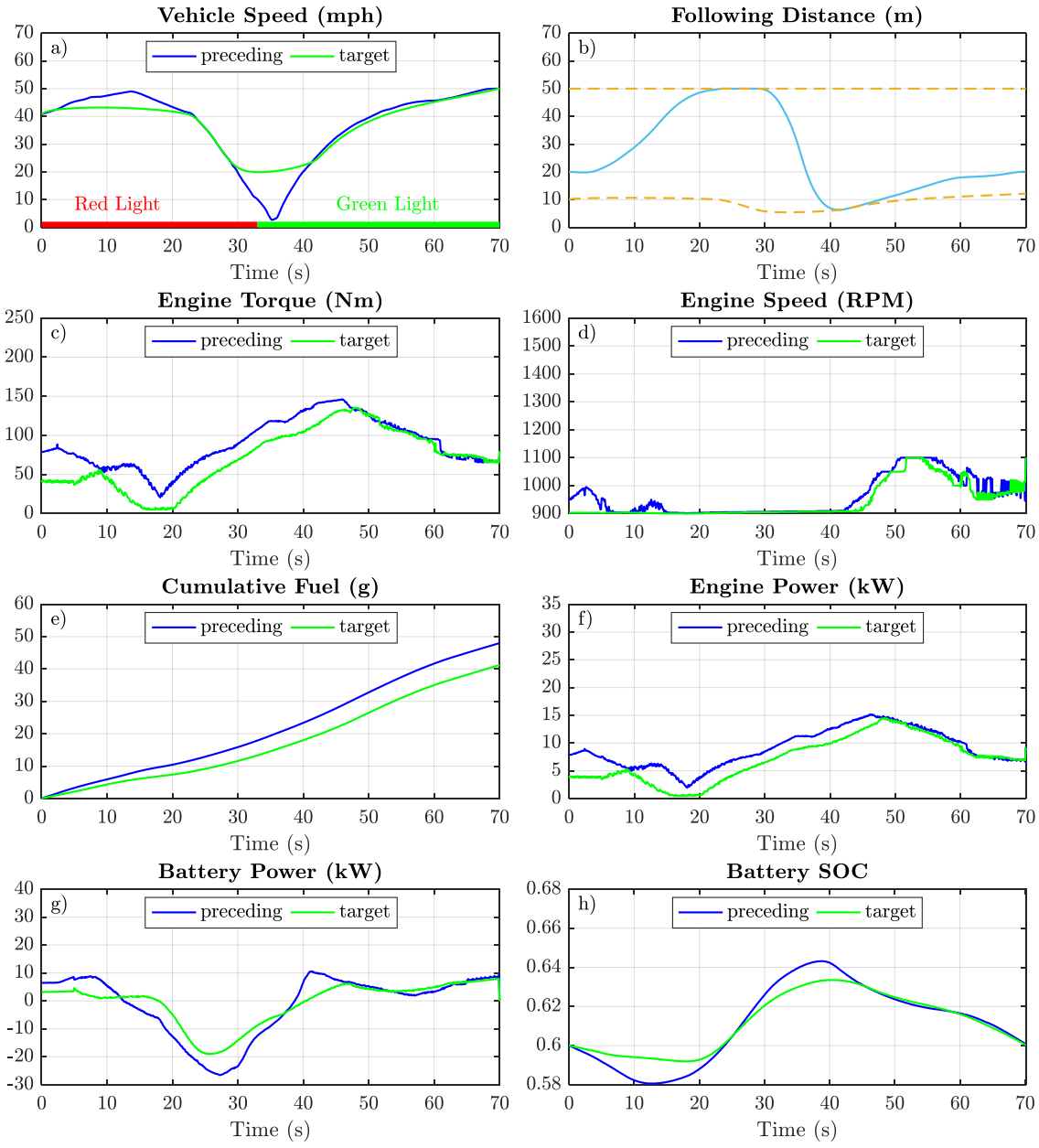


Figure 4.17 Vehicles and powertrain dynamics with optimal powertrain controller

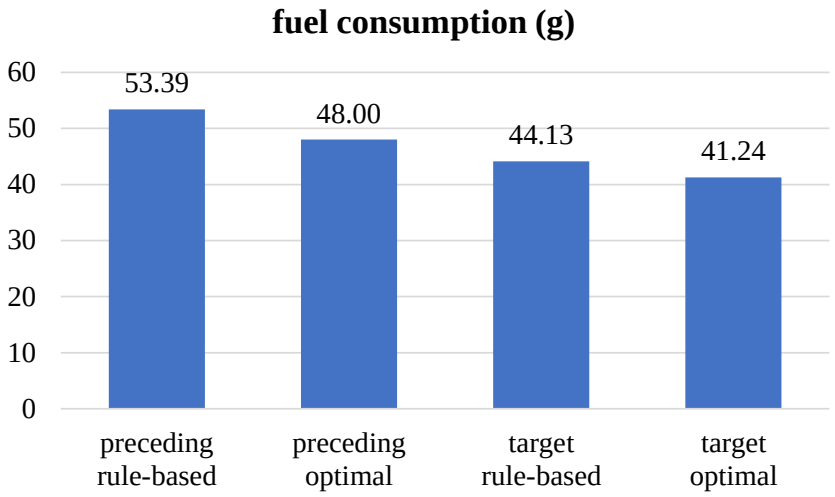


Figure 4.18 Comparison of fuel consumption

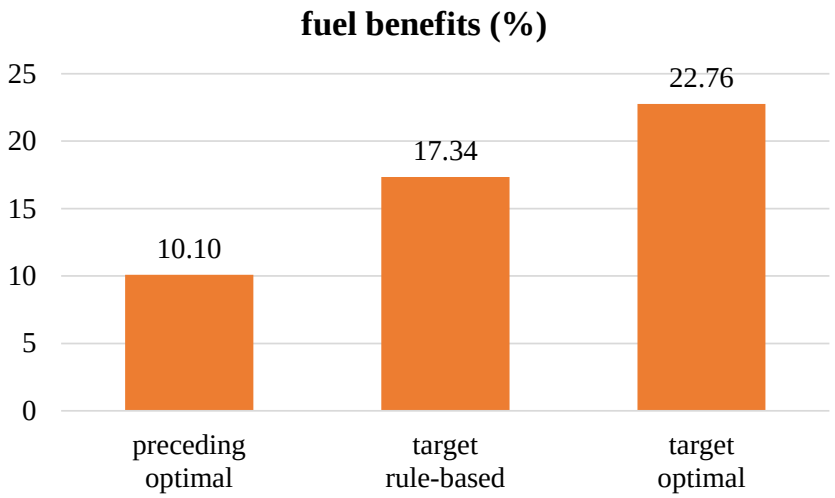


Figure 4.19 Comparison of fuel benefits

## 4.5. Conclusion

This chapter presents a vehicle dynamics and powertrain operation co-optimization controller for a HEV to maximize fuel efficiency. The controller determines optimal vehicle acceleration, power-split and engine operating point all together. It makes use of the emerging CV technology and utilizes present and future information as optimization input, which includes preceding vehicle speed, location, road topography and dynamic

speed limit. The problem was solved using Pontryagin's minimum principle and nonlinear programming. Efforts were made to reduce the computational burden of the optimization process. It can potentially be used in real-time applications. The optimal control is evaluated in two scenarios: 1) rolling terrain scenario with no nearby preceding vehicle; 2) eco-approach scenario where the target vehicle follows a preceding vehicle to pass an intersection.

In the rolling terrain scenario, the results show that benefit of the proposed optimal controller is significant when compared to regular HEV cruising on rolling terrain at constant speed. It ranges from 5.0% to 8.9% on major arterials and from 15.7% to 16.9% on collector roads. The variation is caused by the density change of hilly roads. The proposed integrated optimal controller is superior to individual level optimal controllers. The benefit of the integrated controller generally equals to that of two individual level controllers added together. This indicates that the two individual optimizations have minimal conflict with each other. The proposed optimal controller requires minor speed variation. The speed deviation from speed limit is 1 mph on a 6% slope and 3 mph on a 15% slope. The controller would thus cause little interference to traffic behind. It is implementable right now as a part of a more advanced cruise control system. The proposed optimal controller is robust against information uncertainty and mismatch. The computational time for the optimization is up to 21.6 seconds, given a 400 second optimization time horizon. It can potentially be used in real-time.

In the eco-approach scenario, the target vehicle follows a human-driven preceding vehicle to pass a real-world signalized intersection. With vehicle dynamics and powertrain operation co-optimization, the target vehicle fuel saving is about 23 percent compared to the preceding vehicle. The vehicle dynamics optimization alone saves 17 percent fuel for the target vehicle. The powertrain operation optimization brings in additional 6 percent benefits. Furthermore, with powertrain operation optimization alone, the preceding vehicle can achieve about 10 percent fuel improvement.

# Chapter 5

# Optimization for Battery Electric Vehicles

## 5.1. Introduction

In previous chapters, two of the most common powertrain types of vehicles are studied: internal combustion engine based vehicles (ICVs), where both the vehicle trajectory and gear shift position are optimized, and hybrid electric vehicles (HEVs), where both the vehicle trajectory and power-split between the engine and the battery are optimized. Recently, more studies have been conducted on connected and autonomous electric vehicles (EVs) due to the advancement of battery technologies and the stricter regulations on energy efficiency and emissions. Researchers in [120] studied the optimal speed control for an EV passing signalized arterials. The queue length at the intersection is considered to estimate the upcoming driving conditions. A mixed-traffic platoon is further investigated in [121] where both connected EVs and non-connected vehicles share the road. Study [122] developed a closed-form optimal speed solution for an EV based on the assumption that the preceding vehicle will have a constant acceleration. Both urban and highway scenarios were investigated using real-world trip data. The above studies adopted simplified energy consumption models and assumed that the motor loss is proportional to the current draw square. In [123], researchers developed a motor efficiency model as polynomial functions of motor torque and speed. They studied an EV in highway cruising scenarios on hilly roads and assumed known preceding vehicle's trajectory.

There are several limitations in current literature: *1) The effects of battery aging on speed optimization of EVs are not considered systematically.* The battery is the only power source for EVs and its aging can be a crucial concern to the users. The battery aging process is complicated and can be affected by many factors such as high current

rates, deep depth-of-discharge (DOD), extreme temperatures [124]. Considering these factors may restrict the battery usage and have negative impacts on energy efficiency. Researchers have considered the aging effects when developing battery management strategies for HEVs [125,126] or charging the EVs [127]. There lack studies that consider battery aging for optimal speed control of connected and autonomous EVs. *2) The regenerative braking limits are not discussed.* For EVs, regenerative braking cooperates with the frictional braking to provide the desired deceleration. Regenerative braking converts kinetic energy to electrical energy and charges the battery. It is crucial for EVs to ensure a satisfactory driving range. Ideally, the vehicle should use regenerative braking as much as possible. However, there are many other considerations: a) The maximum amount of regenerative braking depends on the charging current that the battery can take. b) The battery cycling due to frequent or high regenerative braking can accelerate the battery aging especially when the battery state-of-charge (SOC) is high or low [128]. c) When the SOC is near full, the battery can no longer be charged and the frictional braking should provide all the deceleration force. d) At low vehicle speeds (motor speeds), the motor has relatively low charging capability and regenerative braking alone may not be able to stop the vehicle effectively without frictional braking [129]. e) The braking force distribution between the front and rear wheels should be considered as well [130]. High regenerative braking can lock the driving wheels earlier than the driven wheels and may cause vehicle stability or control issues. There lacks literature on how to formulate these considerations as constraints during the optimal speed control of EVs. *3) The traffic prediction is not systematically developed.* In the near future, it is likely that both CVs and non-CVs will share the road. The traffic prediction should be able to handle such mixed-traffic scenarios. It is challenging to use car-following models due to the difficulty in knowing the number of non-CVs in front of the target vehicle. Also, a large car-following distance can bring negative impacts to the entire traffic (e.g. reduce overall traffic throughput). It is crucial to enforce a car-following distance constraint so

that the target vehicle will follow the preceding vehicle within an appropriate distance. It is then necessary to predict the future speed of the preceding vehicle to formulate such constraint.

This chapter aims to address the above limitations and develop a comprehensive optimal speed control framework for connected and autonomous EVs considering battery aging effects and regenerative braking constraints. The target vehicle intelligently controls the vehicle speed and car-following distance based on predicted traffic conditions using real-time information enabled by connectivity. The traffic prediction is based on the traffic flow model and can be implemented in a mixed-traffic scenario (Chapter 2). The control is evaluated for a traffic scenario where the target vehicle follows a vehicle platoon to pass a signalized roadway with two intersections. The optimal control strategy should be solved in real-time and adapts to real-time traffic conditions. The complexity of this problem is mainly due to additional optimization variables and constraints brought by regenerative braking limits and battery aging considerations as well as the enforcement of car-following distance constraints. Though these constraints ensure the optimal control strategy is realistic and can be implemented in a real traffic scenario, they make it more challenging to solve the optimal control problem. In this chapter, direct method is used to obtain a real-time solution. The optimal control problem is formulated with carefully selected optimization variables. Then the problem is simplified and discretized without sacrificing the accuracy and solved by a state-of-the-art numerical solver.

The remainder of this chapter is organized as follows: Section 5.2 formulates the optimization problem; Section 5.3 simplifies the problem and develops the control; Section 5.4 evaluates the proposed control in a simulated traffic scenario; Finally, Section 5.5 concludes the chapter.

## 5.2. Problem Formulation

### 5.2.1. Objective Function

The optimization objective function is defined as:

$$J = \phi\left(\boldsymbol{x}(t_f)\right) + \int_{t_0}^{t_f} [P_{batt}(t) + w_1 \cdot (v(t) - v_{lim})^2 + w_2 \cdot a(t)^2 + w_3 \cdot \sigma(t)]dt \quad (5.1)$$

$$\phi\left(\boldsymbol{x}(t_f)\right) = \psi_1 \cdot \left(d(t_f) - d_f\right)^2 + \psi_2 \cdot \left(v(t_f) - v_f\right)^2 \quad (5.2)$$

where $P_{batt}$ is the battery power demand and its summation is essentially the energy consumption of the vehicle; $\sigma$ is the battery aging model. All other variables follow the definitions in (3.5)(3.6). $P_{batt}(t)$ and $\sigma(t)$ are modeled as the followings:

*1) Energy Consumption Model* The battery output power is used to drive the vehicle motion and provide power to all the auxiliary systems (e.g. headlights, air conditioner, radio). It is assumed that the EV has a single motor and is front wheel drive. This is a typical EV configuration in the market (dual-motor EVs are usually used for luxury cars). For simplicity, the auxiliary power is assumed to be constant during the optimization horizon. Denote vehicle drive power as $P_{drv}$ and auxiliary power as $P_{aux}$, then:

$$P_{batt}(t) = P_{drv}(t) + P_{aux}(t) \quad (5.3)$$

All the vehicle drive power is sent to the electric motor which connects to the vehicle wheels mechanically. The motor efficiency usually depends on the motor operating points (motor speed $\omega_m$ and motor torque $T_m$). Depending on whether the motor is in the motor mode or the generator mode, the relationship between $P_{drv}$ and motor operating points is:

$$P_{drv}(t) = \begin{cases} \dfrac{\omega_m(t)T_m(t)}{\eta_m\left(\omega_m(t),\, T_m(t)\right)}, & T_m(t) \geq 0 \\ \eta_m\left(\omega_m(t),\, T_m(t)\right) \cdot \omega_m(t)T_m(t), & T_m(t) < 0 \end{cases} \quad (5.4)$$

The piecewise function (5.4) can be computationally challenging. It is approximated by the following polynomial as function of motor speed and torque:

$$P_{drv}(t) \approx p_{00} + p_{10} \cdot \omega_m(t) + p_{01} \cdot T_m(t) + p_{11} \cdot \omega_m(t) \cdot T_m(t) \quad (5.5)$$

where $p_{ij}$ are fitting parameters. In this work, an AC induction motor is used based on data from Autonomie [131]. The values of the fitting parameters are shown in Table 5-1 and the coefficient of confidence $R^2$ of the fitting is 0.99.

Table 5-1 Energy consumption model fitting parameters

| $p_{00}$ | $p_{10}$ | $p_{01}$ | $p_{11}$ |
|---|---|---|---|
| 1344.5 | 1.64 | 28.1 | 1.0 |

*2) Battery Aging Model* The aging of lithium-ion batteries (most common battery type for EVs) degrades the performance of an EV. It originates from a number of processes and depends on both the environment and utilization factors. Models derived from electrochemical phenomena can be complex and of high computational cost. Typically, battery aging includes both capacity decrease and resistance increase. As discussed in [124], for lithium-ion batteries, capacity drop is the primary aging effect and can result from either the loss of cyclable lithium or loss of electrode active materials. In this work, only the battery capacity fading effects are considered using the empirical model [132] below

$$Q_{loss}(c,T,Ah) = B(c) \cdot exp\left(\frac{E_a(c)}{R \cdot T}\right) \cdot (Ah)^z \tag{5.6}$$

and

$$c = \frac{|I_{batt}|}{Q_{batt}}; \quad Ah = \int_0^t |I_{batt}| \cdot \frac{dt}{3600} \tag{5.7}$$

where $c$ is the battery C-rate; $I_{batt}$ is the battery current; $Q_{batt}$ is the battery capacity; $B(c)$ is the pre-exponential factor; $E_a(c)$ is the activation energy; $R$ is the gas constant; $T$ is the absolute temperature in Kelvin; $z$ is the power law factor; $Ah$ is the total Ah-throughput of the battery, that is the cumulative electrical charge/discharge of the battery from the first usage to current time instance $t$. The constant 3600 converts the unit of time from seconds to hours. Table 5-2 shows values of the model. Model (5.6) is

based on experimental data and the Arrhenius equation. Effects from battery state-of-charge (SOC) or equivalently depth-of-discharge (DOD) are not explicitly considered but the Ah-throughput has a direct connection to SOC or DOD. The authors of [132] found that influence from different SOCs are small compared to other factors. Similar results can be observed from [133].

Table 5-2 Battery aging model parameters

| Parameter | Value |
|---|---|
| $B(c)$ | $-47.8c^3 + 1215.0c^2 - 9418.9c + 36041.7$ |
| $E_a(c)$ | $31700 - 370.3 \cdot c\ (J/mol)$ |
| $R$ | $8.31\ (J/mol \cdot K)$ |
| $z$ | 0.55 |

The model (5.6) describes the total capacity drop since the first usage of the battery. The capacity loss during the optimization horizon is calculated as the following

$$\begin{aligned} \Delta Q_{loss}(c,T,Ah) &= \int_{t_0}^{t_f} dQ_{loss}(c,T,Ah) \\ &= \int_{t_0}^{t_f} \frac{\partial Q_{loss}(c,T,Ah)}{\partial Ah} \cdot dAh \\ &= \int_{t_0}^{t_f} \dot{Q}_{loss}(c,T,Ah) \cdot c \cdot Q_{batt} \cdot \frac{dt}{3600} \end{aligned} \tag{5.8}$$

In the second line of (5.8), only Ah-throughput is considered as it is the dominant variable in the capacity drop model (5.6). Also, it is assumed that the temperature of the battery is well maintained by the thermal management system and can be considered as a constant. The third line of (5.8) comes from the definition of Ah-throughput as in (5.7).

### 5.2.2. State Equations

$$\dot{\boldsymbol{x}}(t) = \begin{bmatrix} \dot{d}(t) \\ \dot{v}(t) \\ \dot{SOC}(t) \end{bmatrix} = \begin{bmatrix} v(t) \\ a(t) \\ -\dfrac{I_{batt}(t)}{Q_{batt}} \end{bmatrix} \tag{5.9}$$

There are three states: target vehicle's location $d$, speed $v$, and the battery SOC. It is assumed that battery temperature is well maintained by the thermal management system and can be considered as a constant. Otherwise, temperature should be another state with thermal dynamic equation. The battery model is based on the internal resistance model (Figure 5.1):

$$P_{batt}(t) = n_{ser} V_{oc}(SOC) \cdot I_{batt}(t) - I_{batt}^2(t) \cdot \frac{n_{ser}}{n_{par}} R_{batt}(SOC) \tag{5.10}$$

where $n_{ser}$ is the total number of batteries connected in series; $n_{par}$ is the total number of batteries connected in parallel; $V_{oc}$ is the single battery open circuit voltage; $R_{batt}$ is the single battery internal resistance. Both $V_{oc}$ and $R_{batt}$ depend on the current SOC level and the relationships are obtained from [131].

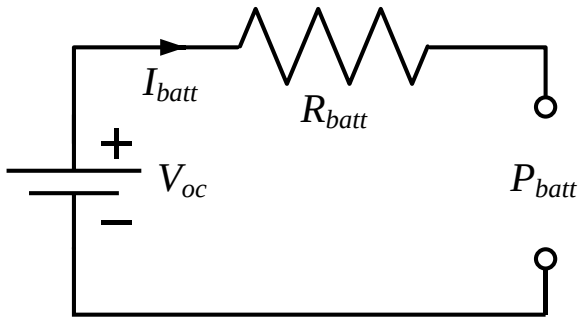


Figure 5.1 Internal resistance battery model ($r_{int}$) for a single battery cell

### 5.2.3. Vehicle and Powertrain Models

The energy consumption model (5.5) is a function of motor speed and torque. The following vehicle and powertrain models are used to convert them into function of states and control (vehicle location, speed and acceleration) [11]:

$$\omega_m(t) = n \cdot v(t), \qquad n = r_t \cdot r_f / r_r \tag{5.11}$$

$$T_m(t) \cdot n = f_\varphi(t) + C_{wind}\, v(t)^2 + m \cdot a(t) + F_b(t) \tag{5.12}$$

and $$f_\varphi(t) = \mu mg \cdot cos[\varphi(d(t))] + mg \cdot sin[\varphi(d(t))] \tag{5.13}$$

where all variables follow the definitions in (3.2)-(3.4). Again, it is assumed that $f_\varphi(t)$ is known as a function of time and equals to what the preceding vehicle would experience (speed of preceding vehicle comes from the traffic prediction). With the relationships in (5.11)-(5.13), the energy consumption model (5.5) can be written as below with parameters shown in Table 5-3:

$$\begin{aligned} P_{drv}(t) = {} & \left[p_{00} + p_{01} \cdot \frac{f_\varphi(t)}{n}\right] + \left[p_{10} n + p_{11} \cdot f_\varphi(t)\right] \cdot v(t) + \left[p_{01} \cdot \frac{C_{wind}}{n}\right] \cdot v^2(t) \\ & + \left[p_{11} \cdot C_{wind}\right] \cdot v^3(t) + \left[p_{01} \cdot \frac{m}{n}\right] \cdot a(t) + \left[\frac{p_{01}}{n}\right] \cdot F_b(t) \\ & + p_{11} m \cdot v(t) \cdot a(t) + p_{11} \cdot v(t) \cdot F_b(t) \end{aligned} \tag{5.14}$$

Table 5-3 Vehicle and powertrain models parameters

| Parameter | Value |
|---|---|
| $n$ | 23.5789 |
| $C_{wind}$ | 0.4153 |
| $m$ | 1848 $kg$ |

### 5.2.4. Constraints

*1) Jerk Constraints* The rate of acceleration (jerk) is constrained to avoid sudden jumps of the acceleration:

$$-jerk_{min} \le \dot{a}(t) \le jerk_{max} \tag{5.15}$$

*2) Physical Bounds Constraints* The vehicle speed and acceleration is bounded:

$$0 \le v(k) \le v_{lim}, \qquad a_{min} \le a(k) \le a_{max} \tag{5.16}$$

*3) Traffic Constraints* Similar as in Section 3.2.5, if following a preceding vehicle, the car-following distance should be constrained to ensure both a safe operation and a

satisfactory traffic throughput. Also, if passing an intersection, the target vehicle can only pass the intersection when the signal is green [13].

$$d(t) \geq d_p(t) + \beta \cdot \sigma_{d_p}(t) - d_{max} \tag{5.17}$$

$$d(t) \leq d_p(t) - \beta \cdot \sigma_{d_p}(t) - \left(d_{min} + h_{min} \cdot v(t)\right) \tag{5.18}$$

$$d_{sig} \leq d(t_r), \qquad d\left(t_g\right) \leq d_{sig} \tag{5.19}$$

where all variables follow the same definitions as in Section 3.2.5. The constraints have to be satisfied for the entire optimization horizon (from $t_0$ to $t_f$). Future location of the preceding vehicle is anticipated using the traffic prediction algorithm (Section 2.2).

*4) Regenerative Braking Constraints* There are several constraints for regenerative braking as discussed in Section 5.1.

- The first constraint is due to the maximum charging current constraint which is a function of SOC [131,134,135]. The maximum charging current should be zero when SOC is full. The maximum charging current map from [131] is adopted here, as shown in Figure 5.2. Using (5.10), the maximum charging power can be obtained. Then for a given vehicle speed, the maximum charging torque can be formulated:

$$T_{m_{min}}\left(n \cdot v(t), SOC(t)\right) + T_{rsrv} \leq T_m(t) \tag{5.20}$$

Using (5.12), constraint (5.20) can be written as a maximum combined deceleration for given SOC and grade angle.

$$\begin{aligned}\left[\left(T_{m_{min}}\left(n \cdot v(t), SOC(t)\right) + T_{rsrv}\right) \cdot n - f_\varphi(t) - C_{wind} \cdot v^2(t)\right]/m \\ \leq \left(\underbrace{a(t) + F_b(t)/m}_{a_{comb}}\right)\end{aligned} \tag{5.21}$$

The left-hand-side of (5.21) depends on SOC and grade angle. To obtain an analytical model, all possible SOC and grade angle values are gridded and for each SOC and grade angle, (5.21) is approximated as the following ($b_i(SOC, \varphi)$ are coefficients depend on SOC and grade angle):

$$\begin{aligned}\max\{b_1(SOC, \varphi) \cdot \exp(b_2(SOC, \varphi) \cdot v(t)) + b_3(SOC, \varphi), a_{flat}\} \\ \leq \left(\underbrace{a(t) + F_b(t)/m}_{a_{comb}}\right)\end{aligned} \tag{5.22}$$

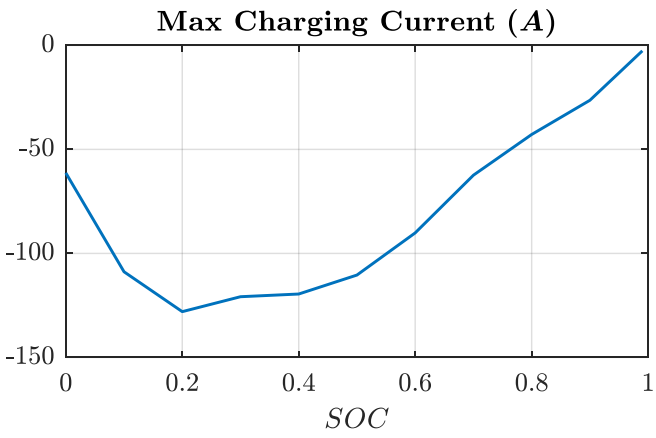


Figure 5.2 Maximum charging current of the battery

- The second constraint is to limit regenerative braking when vehicle speed is low (below $v_{small}$). Essentially, the constraint (5.23) is in the form of a step function. It is approximated using a smooth sigmoid function (5.24):

$$0 \leq T_m(t), \qquad if\ v(t) < v_{small} \tag{5.23}$$

$$\frac{T_{m_{min}}}{1 + \exp[-\alpha \cdot (v(t) - v_{small})]} \leq T_m(t) \tag{5.24}$$

- The third constraint is to balance the braking force distribution (BFD) between the front and rear wheels. For a single wheel drive EV, if solely relies on the regenerative braking on the driving wheels to decelerate, the driving wheels will have high braking force and the wheels will lock much earlier than the driven wheels. For a front wheel drive EV, this means the front wheels will lockup earlier which can cause a loss of directional control. For a rear wheel drive EV, this means loss of directional stability. Therefore, to deliver the desired total deceleration, braking force should be distributed appropriated on both front and rear wheels. For a front wheel drive EV, which is considered in this work, the feasible braking force distribution region is shown as the blue area in Figure 5.3 [136]. The two axes show the braking force on each wheel with respect to the weight of the vehicle. Alone each dashed gray lines, the summation of braking forces on front and rear wheels is constant and thus vehicle deceleration is

constant. On the upper bound curve (known as I-curve) of the blue feasible region, front and rear wheels will lockup at the same time. Usually, the real wheel lockup is more safety critical so it is preferable to have more front wheel braking (operate below the I-curve). The lower bound curve of the BFD region is to prevent the front wheels being locked too early. The red shows the BFD curve used in this work. All the braking force will be produced by the regenerative braking if deceleration is less than 0.2g. After that, both frictional braking and regenerative braking will work together to produce the braking force. The BFD constraint can be described as:

$$F_b(t) \geq d_1 \cdot T_m(t) \cdot n + d_2 \;\&\; F_b(t) \geq d_3 \cdot T_m(t) \cdot n + d_4 \tag{5.25}$$

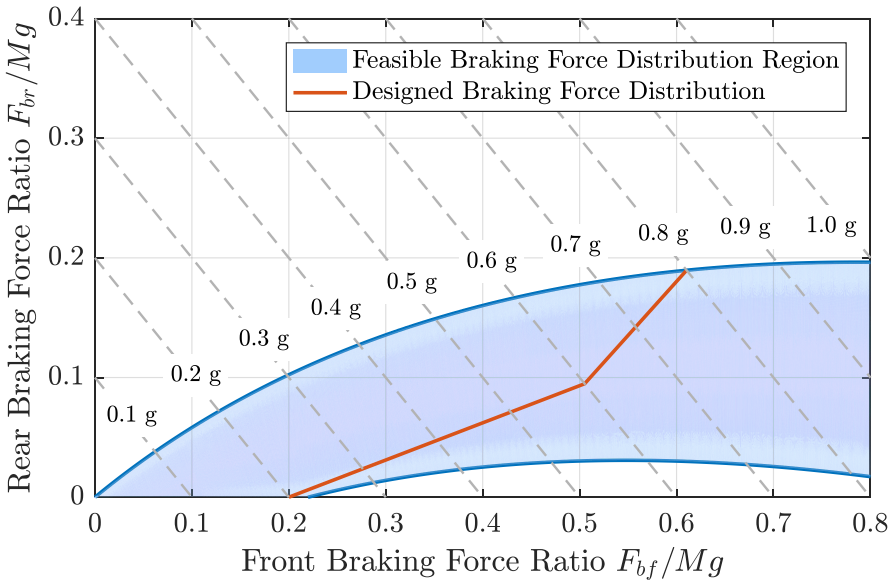


Figure 5.3 Brake force distribution design

*5) Discharging Constraints* The regenerative braking constraints limit the battery charging. Battery discharging should be constrained as well. It is assumed that the maximum battery discharging limit is the same as the maximum torque limit of the motor characteristic, that is:

$$T_m(t) \leq T_{m_{max}}\big(n \cdot v(t)\big) \tag{5.26}$$

Use an exponent function to develop an analytical form:

$$a(t) + F_b(t)/m \leq min\{c_1\, exp\big(c_2 \cdot v(t)\big) + c_3, T_{m_{flat}}\} \tag{5.27}$$

## 5.3. Control Design

In this section, the optimal control problem formulated in the previous section is solved. The optimization is implemented in the MPC fashion following the framework in Section 2.1. At each update instance $t_{UD}$ (1 second), the controller updates both traffic prediction and the actual vehicle and powertrain states. The traffic prediction method presented in Section 2.2 is used to anticipate future driving conditions using information enabled by connectivity. The output of the traffic prediction is the speed of the immediate preceding vehicle which formulates the constraints (5.17)(5.18). Then the optimization problem is solved for the next prediction horizon $t_{PH}$ (15 secons). The first $t_{UD}$ seconds of the optimal control law is implemented and the control is updated again with new traffic information. To further reduce the computational burden, the optimization problem is simplified with carefully selected optimization variables (Section 5.3.1). The problem is discretized using an efficient multi-interval pseudo-spectral method (Section 5.3.2) and transformed into a NLP problem. The optimal solution is obtained using a state-of-the-art NLP solver (Section 5.3.3).

### 5.3.1. Problem Simplifications

During the optimization horizon (15 seconds in this work), the SOC level will not significantly change considering the large size of the battery pack for an EV. Therefore, it is assumed that during each optimization horizon, SOC is approximately a constant and it only gets updated at the beginning of each update instance. This is a reasonable assumption as shown in the simulation results in Section 5.4. Based on this assumption, the SOC dynamic (5.9) is neglected and all the variables depend on the SOC are considered as constant. Other problem simplifications include:

*1) Battery Aging Model Simplification* The Ah-throughput is directly linked to SOC. Since the battery SOC is assumed to be constant (during each optimization horizon), the battery aging model (5.8) is reduced as a function solely depends on battery C-rate. It is further approximated as a cubic polynomial:

$$\begin{aligned}\Delta Q_{loss}(c) &= \int_{t_0}^{t_f} \dot{Q}_{loss}(c, T, Ah) \cdot c \cdot Q_{batt} \cdot \frac{dt}{3600} \\ &\approx \int_{t_0}^{t_f} (q_1 \cdot c^3 + q_2 \cdot c^2 + q_3 \cdot c) dt\end{aligned} \tag{5.28}$$

where $q_1, q_2, q_3$ are fitting parameters. These parameters are determined for gridded points of all possible temperature and Ah-throughput values. The parameter maps are created offline and stored as lookup tables. As the SOC gets updated at the beginning of each optimization horizon, the Ah-throughput and temperature gets updated. These fitting parameters are then obtained from the stored lookup tables.

*2) Optimization Variables Selection* The optimization variables include the states: vehicle location and speed; the control variables: vehicle acceleration, frictional braking force, and an additional variable battery current. Battery current is necessary to model the battery aging (5.28). Based on (5.10), battery current $I_{batt}$ depends on battery power and can be written as a function of vehicle speed and acceleration. It is selected as an additional variable so that the battery aging model can be kept with a simpler form to reduce computational burden. Thus (5.10) is considered as an additional equality constraint.

### 5.3.2. Discretization

The multi-interval pseudo-spectral method is adopted here. The optimization horizon is divided into multiple intervals. In each interval, trajectories of controls (vehicle acceleration $a$, braking force $F_b$), states (vehicle location $d$ and speed $v$), and the additional variable battery current $I_{batt}$ are approximated with low-order polynomials at Legendre–Gauss–Lobatto (LGL) quadrature nodes. The optimization solves values of

these variables at these nodes. The discretization follows the same steps as in Section 3.3.2. Note that, when discretizing constraints (Step 5 as in Section 3.3.2), there is no engine torque rate constraint for EVs and the jerk constraint (5.15) is discretized as the following

$$\begin{aligned} D^i \cdot \left[a\left(\tau_0^i\right)\ a\left(\tau_0^i\right)\ \cdots\ a\left(\tau_0^i\right)\right]^T &\le jerk_{max} \cdot \left(\frac{t_i - t_{i-1}}{2}\right) \\ -D^i \cdot \left[a\left(\tau_0^i\right)\ a\left(\tau_0^i\right)\ \cdots\ a\left(\tau_0^i\right)\right]^T &\le jerk_{max} \cdot \left(\frac{t_i - t_{i-1}}{2}\right) \end{aligned} \tag{5.29}$$

where the $D^i$ matrix follows the definition in (3.34). Also, when enforcing continuity constraints (Step 6 as in Section 3.3.2), large jerks between two discretization intervals are avoided by the following constraints

$$\begin{aligned} a\left(\tau_{N^{i-1}}^{i-1}\right) - a\left(\tau_0^i\right) &\le jerk_{max} \cdot \left(\tau_0^i - \tau_{N^{i-1}}^{i-1}\right) \\ -\left(a\left(\tau_{N^{i-1}}^{i-1}\right) - a\left(\tau_0^i\right)\right) &\le jerk_{max} \cdot \left(\tau_0^i - \tau_{N^{i-1}}^{i-1}\right) \end{aligned} \tag{5.30}$$

### 5.3.3. Obtain Numerical Solution of the Optimal Control

With all the simplification and discretization, the optimization problem is formulated with minimal computational burden. In addition, analytical gradients and hessians are calculated and provided to the NLP solver to further reduce the computation burden. The optimization problem is solved using IPOPT [33] (which is one of the best state-of-the-art NLP solver [99]) and implemented in Matlab. The traffic prediction horizon $t_{PH}$ is 15 seconds and the prediction gets updated every 1 second ($t_{UD} = 1$). For all update instances, the average computational time of the optimization is 0.54 seconds (on a laptop with i7 CPU@2.6 GHz). This validates the real-time potential of the proposed optimal controller.

## 5.4. Simulation Results

### 5.4.1. Scenario

The traffic scenario is generated using the microscopic traffic simulator VISSIM. The roadway is assumed to be single-lane with speed limit 55 mph. For simplicity, it is

assumed that the roadway is flat (grade angle equals to zero). A 16-vehicle platoon is selected as the case study and the target vehicle follows the last vehicle in the platoon. It is assumed that 8 vehicles of the platoon are CVs which means 50% penetration rate (PR) of connectivity. All CVs broadcast their locations and speeds information. Information of all non-CVs in the platoon is unknown to the target vehicle. The communication range between two CVs is assumed to be 300-meter [13]. The roadway of interest contains two consecutive intersections. The first one is at 800-meter and the second one is at 2000-meter. The total travel distance is 2500-meter and travel time is about 160 seconds. For simplicity, perfect communication is assumed without delays and packet drops. The energy consumption of the target vehicle is compared to the immediate preceding vehicle (baseline vehicle) which is the last vehicle in the platoon.

### 5.4.2. Simulation Results

Figure 5.4 shows comparison of car-following performance between the perfect prediction scenario and the 50% penetration rate (8-CV prediction) scenario. In the perfect prediction scenario (two top figures in Figure 5.4), the target vehicle fully utilizes the spacing range between the upper and lower following distance constraints. It anticipates the traffic slow down due to red lights and decelerates earlier than the preceding vehicle at both of the two intersections. The total amount of deceleration is reduced to avoid waste of kinetic energy. As a consequence, the target vehicle accelerates less after the signals turn green and saves energy. The energy saving is 14.3%. In the 8-CV prediction scenario (two bottom figures in Figure 5.4), the target vehicle is more conservative in using the following distance range due to the constraints (5.17)(5.18). Due to inaccurate traffic prediction, the target vehicle decelerates more than the perfection prediction scenario and hence loses more kinetic energy. Overall, the controller can achieve 9.1% energy benefit which is satisfactory.

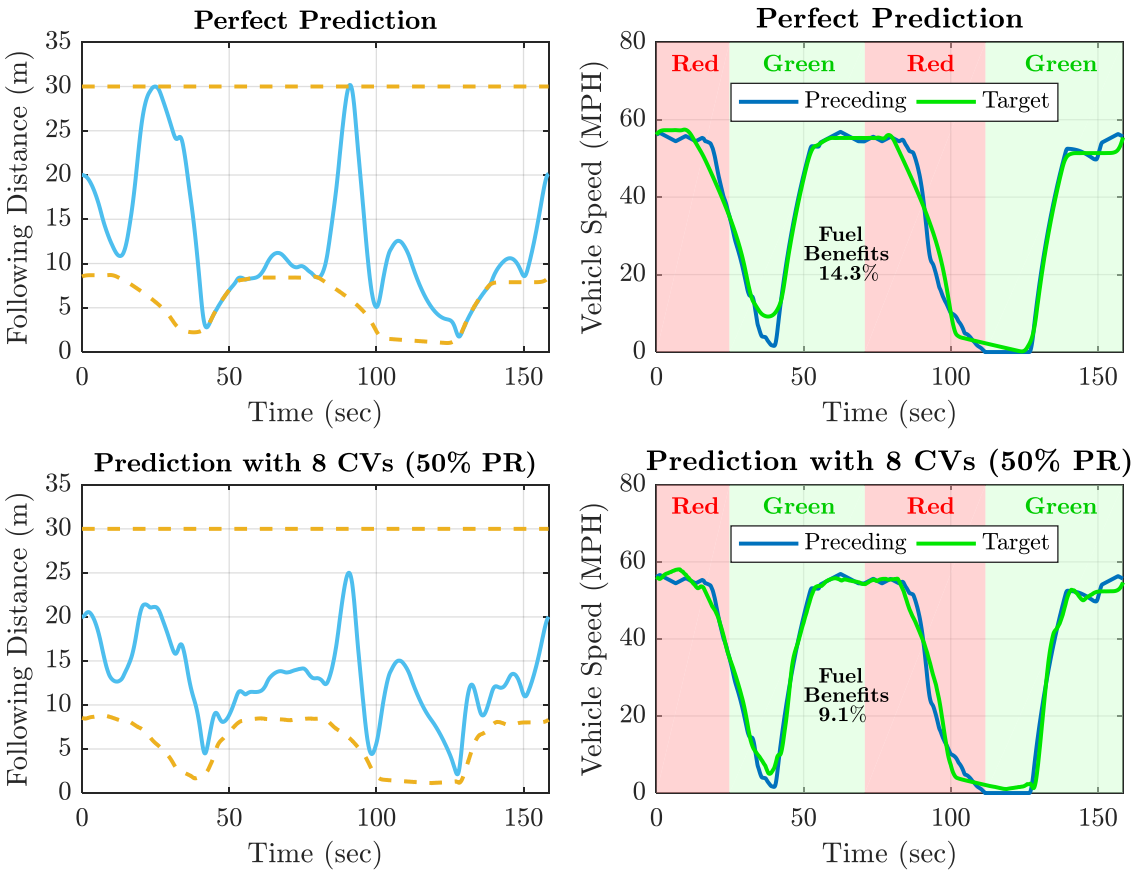


Figure 5.4 Car-following performance comparison

Figure 5.5 shows comparison of powertrain states between the target vehicle and the preceding vehicle for the 8-CV prediction scenario. It can be seen that the majority of the energy benefits come from less decelerations when approaching the intersections and less aggressive accelerations when leaving the intersections. The preceding vehicle decelerates more and reaches the limits of regenerative braking Figure 5.5g). The frictional braking has to kick in and the kinetic energy wastes to heat. The target vehicle stays away from the regenerative braking limits and uses much less frictional braking (total frictional braking force is 54% less). Figure 5.6 shows the comparison of motor operating points. Overall, the target vehicle tends to operate the motor in more efficient regions. During the deceleration and acceleration, the motor operating points tends to move along the gradients of the efficiency contours which validate the optimality. The

preceding vehicle stays longer in low efficient regions (around low speed or low torque). Note that during low motor speed regions, motor torque is non-negative due to the cutoff of regenerative braking when vehicle speed is low, as in constraint (5.24). Based on the battery aging model (6), the target vehicle achieves energy benefits without significant impacts on the battery aging (the capacity loss increases by about 3%).

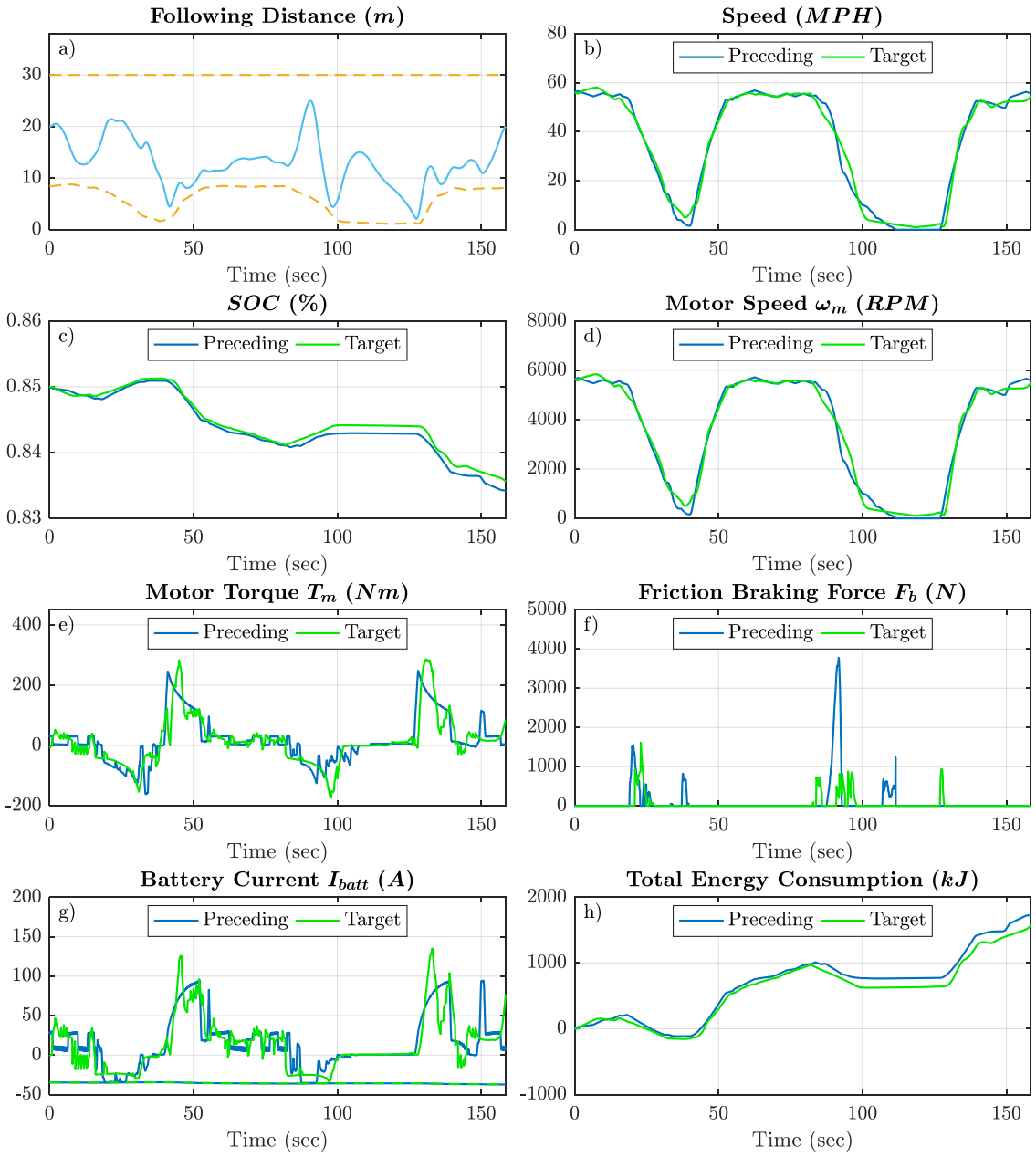


Figure 5.5 Powertrain states comparison

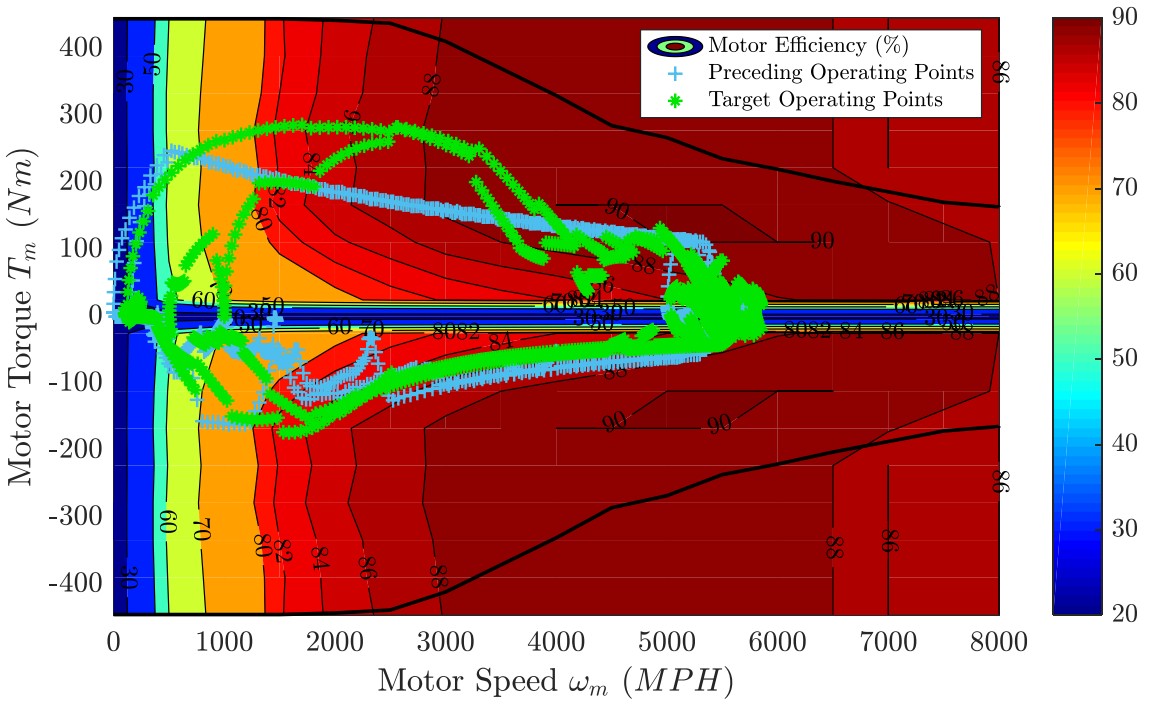


Figure 5.6 Motor operating points comparison

Figure 5.7 shows the energy flow comparison between the target vehicle and the preceding vehicle. All the percentages refer to energy in joule. For the preceding vehicle, 40% of the energy on the vehicle wheels goes to the regenerative braking. For the target vehicle, the regenerative braking accounts for near 48%. In addition, the target vehicle uses more regenerative braking to decelerate and reduces the wastes due to frictional braking. The motor loss of the target vehicle decreases as it operates the motor in more efficient regions. For the target vehicle, through regenerative braking, total of 0.19kWh is recovered to the battery and the total positive battery output is 0.63kWh. The net energy returned to the battery is 30%. For the preceding vehicle, the value is 25%. This verifies the benefits from the optimal controller and demonstrates that it is crucial for EVs to have the regenerative braking capabilities. All the energy flow percentage values are within the same range as the estimation from [137][138] for an EV in urban drive. This confirms the fidelity of the simulation study.

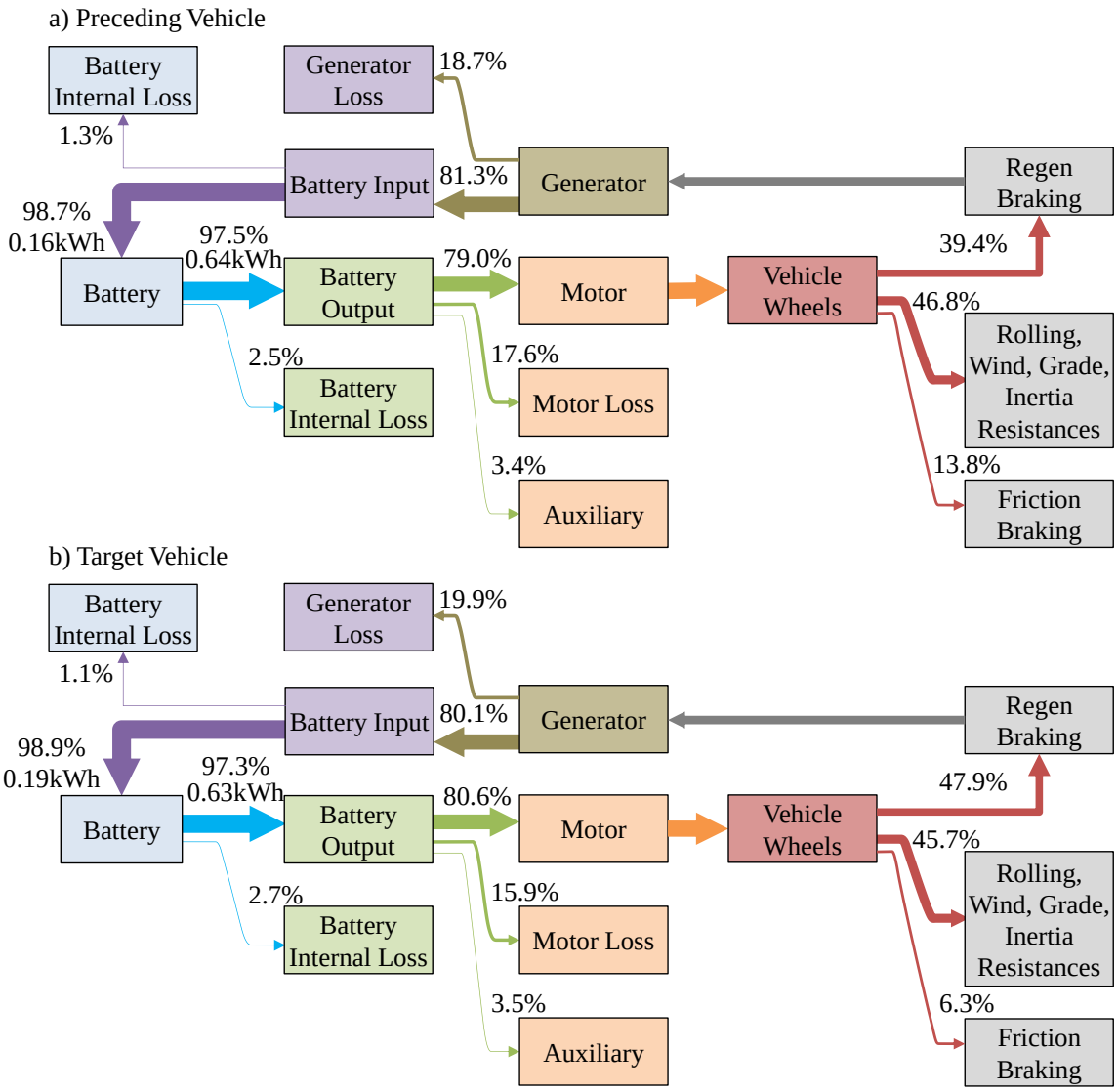


Figure 5.7 Energy flow comparison

For EVs, the regenerative braking may start as soon as the driver lifts off the pedal (known as one-pedal driving). This gives an additional degree of freedom in improving the energy efficiency of an EV. It will be preferable to have an aggressive regenerative braking if the driver pedals off to make a full stop. However, if the driver intends to glide, regenerative braking can potentially decrease the energy efficiency. During regenerative braking, kinetic energy is transferred to electrical energy. Later, it is converted back to kinetic energy when vehicle power is needed. This double-conversion is less efficient.

Ideally, the regenerative braking should only be activated when it is anticipated that the vehicle power request will be low, that is when the vehicle is indeed going to a full stop rather than gliding.

## 5.5. Conclusion

A comprehensive optimal speed control framework for connected and autonomous electric vehicles is developed considering battery aging effects and regenerative braking constraints. The proposed optimal speed control is evaluated in a simulated traffic scenario for a signalized roadway with two intersections. The results show that with 50% penetration rate of connectivity, the target vehicle can achieve 9.1% energy improvement. The performance is satisfactory compared to the 14.3% energy saving with perfect traffic prediction. This demonstrates the effectiveness of the proposed optimization method. The consideration of battery aging ensures a satisfactory battery life and the regenerative braking constraints make the optimal control strategy realistic for practice. The proposed control method can be extended to other connected and autonomous vehicle applications as well as other traffic scenarios.

# Chapter 6

# Evaluating Connected and Autonomous Vehicles Using a Hardware-in-the-loop Testbed and a Living Lab

## 6.1. Introduction

In previous chapters, several energy focused CAV applications have been developed for vehicles of different powertrain types. As mentioned in Section 1.5, there are many technical challenges to evaluate the effectiveness and energy benefits of these CAV applications. Several researchers have investigated hardware-in-the-loop (HIL) simulations to allow an actual testing vehicle to interact with simulated traffic [48,49]. However, to avoid safety concerns, these HIL experiments usually don't allow interactions between the actual testing vehicle and the real traffic, and are limited to proving grounds. Instead of letting an actual target vehicle interacting with virtual traffic, the HIL testbed demonstrated in this chapter allows a virtual target vehicle to interact with real traffic while maintaining the fidelity of fuel and emissions measurement with laboratory instruments. A laboratory powertrain research platform is used to represent the virtual target vehicle, which consists of an actual engine, an engine loading device (hydrostatic dynamometer), and vehicle dynamic models. The real traffic information is brought to the powertrain research platform through communications with on-road testing vehicles and instrumented traffic intersections. The key advantages are, with an actual engine, the target vehicle simulated by the powertrain research platform can accurately represent the dynamics of the target vehicle and it can interact with real traffic with no safety concern.

Our previous work [55] has enabled the HIL testbed to interact with virtual traffic from VISSIM in real-time. In this chapter, the HIL testbed is further enhanced to match the performance of an actual vehicle and to incorporate real-world traffic information

using a living lab. The validation with actual vehicles significantly improves the credibility of the HIL testbed. The introducing of real-world traffic data extends the capabilities of the HIL testbed. It enables the HIL testbed to evaluate the real-time capability and robustness of various CAV applications in realistic roadway conditions. To match an actual testing vehicle, the same engine as the actual vehicles at the Federal Highway Administration (FHWA) was installed on the HIL testbed. Both the powertrain and vehicle models were carefully calibrated using actual vehicle data generated from a FHWA research project [100,139]. The performance of the virtual target vehicle emulated by the powertrain research platform was compared against the actual vehicle's performance data to validate the effectiveness and accuracy of the HIL testbed. Experimental results of eight sets of roadway scenarios show great matching between the HIL testbed and the actual vehicle, with about 1% error. In all eight sets, the same roadway conditions as the actual vehicle (speed limit, degree of road slope, etc.) were input into the HIL testbed and the dynamometer generates the same load as the actual vehicle's engine is getting. In addition, the living lab enables the HIL testbed to interact with real traffic and extends the capabilities to the HIL testbed. Two new testing capabilities have been demonstrated through two CAV applications. All these works lead to an innovative CAV evaluation testbed that is economic, effective, and without safety concerns. High-accuracy vehicle performance is captured by the HIL testbed and realistic real-world traffic scenarios are generated by the living lab. The HIL testbed can thus evaluate the performance of a target CAV that follows an on-road testing vehicle driven on real-world roadway conditions to evaluate different CAV applications.

The remainder of the chapter is organized as follows: Section 6.2 presents how the HIL testbed is configured to match an actual testing vehicle; Section 6.3 discusses the approaches to develop a living lab; Section 6.4 shows test results to demonstrate the HIL testbed's capabilities to match an actual testing vehicle and the functions of the living lab; Finally, Section 6.5 concludes the chapter. For clarity, note that when we mention

powertrain research platform, it refers to the system that consists of an actual engine, a hydrostatic dynamometer and all related controllers to emulate a virtual target vehicle; when talking about HIL testbed, it means the entire testing platform which includes the traffic simulation, the living lab and the powertrain research platform.

## 6.2. HIL Testbed Configuration

### 6.2.1. Overview

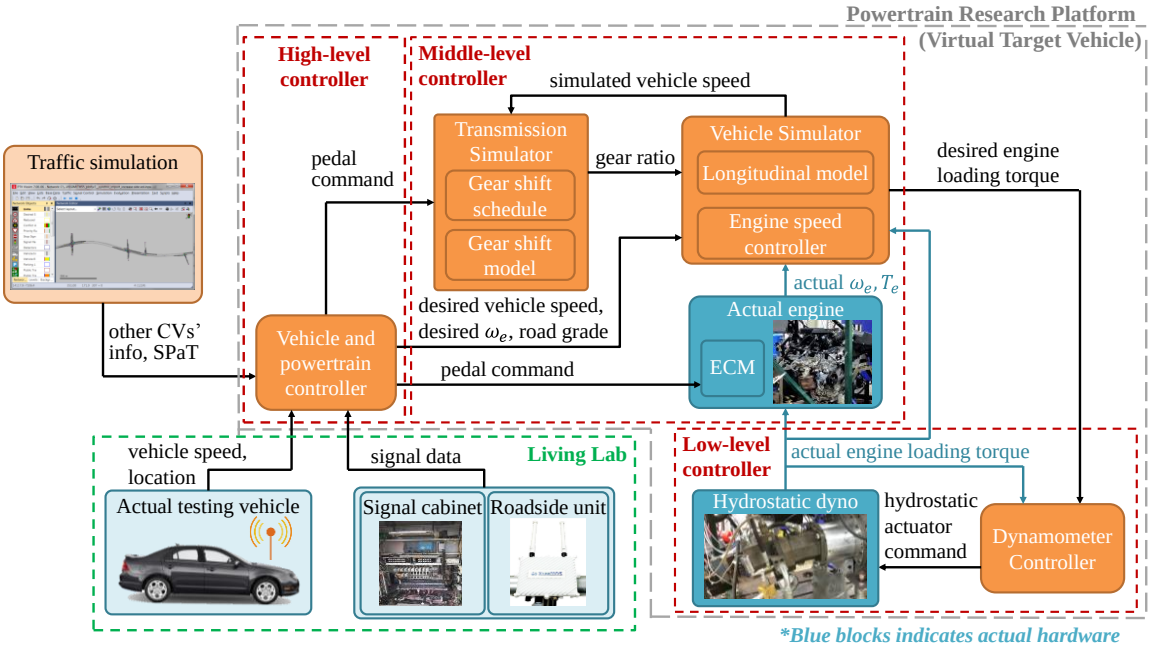


Figure 6.1 Overall architecture of the HIL testbed

The HIL testbed developed at the University of Minnesota [55] was reconfigured so that it can match the performance of an actual testing vehicle and can incorporate real traffic information through the living lab (Section 6.3). Figure 6.1 shows the overall architecture of the HIL testbed. The blocks in blue indicate actual hardware, such as the actual engine, hydrostatic dyno, and all components of the living lab (i.e. actual testing vehicles, signal cabinet, RSU); the blocks in orange color indicate software includes traffic simulator (VISSIM), all controllers, and vehicle models. The same engine as the

actual testing vehicle at the FHWA was purchased and installed (Section 6.2.2). The engine is controlled using a three-level control architecture similar to [101]. With these controllers, the engine in the lab can receive the same loading torque as an actual testing vehicle and match the actual vehicle's performance:

*1) High-level controller.* The high-level controller receives the same traffic conditions as the target vehicle (speed limit, road slope angles, preceding vehicle's speed and location, etc.), and commands the same vehicle trajectories (vehicle's location, speed, acceleration, etc.), and powertrain states (engine speed, engine torque, etc.) as the target vehicle. To match the performance of an actual vehicle (Section 6.4.2), the same roadway conditions are input to this controller, and the controller commands the same vehicle trajectories and powertrain states as the actual vehicle. For an energy focused CAV application, this controller is essentially an optimization algorithm for fuel improvement (see Section 6.4.3.1). This controller uses several engine maps that were obtained by running the newly installed engine through different operating points (Section 6.2.3).

*2) Middle-level controller.* The middle-level controller includes the transmission model (powertrain model) and the vehicle model. To match the performance of an actual testing vehicle, these models were carefully calibrated using actual vehicle data generated from a FHWA research project [100,139]. The transmission model (Section 6.2.4) contains a shift schedule and a gear shift model. The shift schedule determines the current gear ratio between the engine speed and the vehicle wheel speed, and was obtained using actual vehicle testing data. The gear shift model describes the dynamics of the gear shifting process. The vehicle model (Section 6.2.5) has a vehicle longitudinal model and an engine controller. The longitudinal model simulates the vehicle dynamics and outputs the simulated vehicle longitudinal speed. The engine controller determines the desired engine loading torque based on the longitudinal dynamics, desired and actual engine speed.

*3) Low-level controller.* The low-level controller receives the desired engine loading torque command from the middle-level controller and it controls the hydrostatic dynamometer to provide that loading torque to the actual engine. A feedback linearization controller [119] is used to achieve precise loading torque tracking.

In the following sections, each element of the HIL testbed is discussed in details.

### 6.2.2. Target Engine Installation

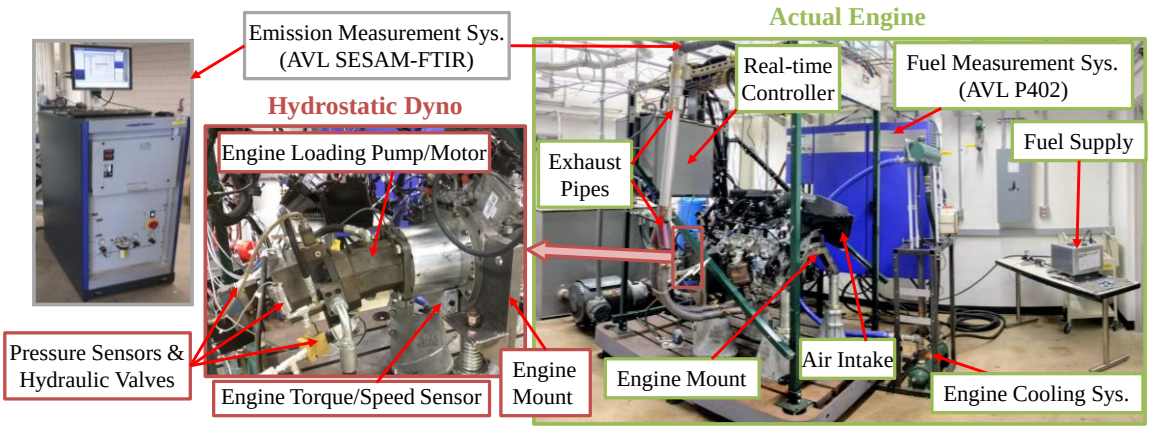


Figure 6.2 Overview of the powertrain research platform

The same engine as the actual testing vehicle (2013 Cadillac SRX) at the Federal Highway Administration was installed, which is a General Motors (GM) LFX 3.6L V6 engine. A transient hydrostatic dynamometer was used to motor or load the engine [119]. Figure 6.2 shows the overview of the powertrain research platform after all configurations. All necessary mechanical and electronic components of the engine were installed, including the engine control module (ECM), harness cables and relay & fuse box. The stock ECM software is used to operate the engine. Therefore, the engine control strategies (e.g. spark timing, fuel injection timing) remain the same as in an actual vehicle. The desired engine operating points (engine speed and engine torque) are determined by the high-level controller (as in Figure 6.1) and commanded using two control signals sent from the real-time controller. These two control signals mimic the output signals from an

actual accelerator pedal (driver's command). The ECM receives these signals and then commands the engine throttle opening to change the engine output power.

The real-time engine speed and torque are measured by a high precision Hottinger Baldwin Messtechnik GmbH (HBM) T12 torque/speed transducer. It was installed between the engine crankshaft and the engine loading pump/motor shaft. Both the engine and the loading pump/motor were mounted through customized engine mount, casing and adapters. The same air intake manifold as an actual vehicle is used, while the engine cooling system was redesigned with customized coolant tank and radiator. The outlets of the catalytic converters were connected to the building exhaust through customized pipes as well. Necessary connecting hoses were installed to connect the precise fuel consumption and emission measurement systems to the engine. The fuel measurement system is a P402 from AVL with measurement uncertainty of 0.1% and output frequency of up to 80 kHz. The emissions are measured using AVL's SESAM-FTIR, which can measure up to 25 components of exhaust gas from engine combustion including NOX, CO, CO2 and HCHO with a sampling rate of 1 Hz.

### 6.2.3. Engine Maps Development

Engine maps are necessary for developing the three-level controller of the HIL testbed and for calibrating vehicle and powertrain models. In total, three steady-state engine maps were obtained in the lab:

*1) Engine speed, throttle and engine torque map.* Both the engine speed and throttle trajectories were recorded from actual vehicle but the engine torque was not measured due to the lack of a torque sensor on the actual vehicle. With this engine map, the corresponding engine torque can be obtained which is important for both the transmission model calibration (Section 6.2.4) and the vehicle model calibration (Section 6.2.5).

*2) Engine speed, throttle and accelerator pedal map.* As mentioned in the previous section, the throttle is commanded indirectly by sending the accelerator pedal signals to

the ECM. With this engine map, the correct pedal command can be determined given recorded engine speed and throttle commands from the actual vehicle.

*3) Engine speed, throttle and fuel consumption map.* This engine map is crucial for developing the fuel consumption model of the target vehicle. This model is necessary for designing optimization algorithms in a CAV application (e.g. eco-approach application in Section 6.4.3.1). In addition, it could be used as a benchmark to validate the engine maps obtained on the HIL testbed by comparing the calculated fuel consumption from the engine map against the measured fuel consumption from the actual vehicle.

To develop these engine maps, the engine was controlled to run through different steady-state operating points and the corresponding data was measured and recorded. The following procedures were adopted: First, the testing points were determined for both the engine speed and throttle based on their operating ranges from actual vehicle tests. The engine speed was gridded every 100 revolutions per minute (RPM) step and the throttle was gridded every 1%. In certain regions where the engine torque is sensitive to the throttle changes, additional throttle grids were tested for every 0.5%. Second, the HIL testbed was controlled to hold both the engine speed and torque at steady state for each testing point. The corresponding data (engine speed, engine torque, pedal and throttle position, and fuel consumption) were measured and recorded. Each set point was held for at least 30 seconds to ensure the engine has reached steady-state. Finally, all recorded data were processed to develop the engine maps. The outliers were excluded and the measurements were averaged. Figure 6.3 show the three engine maps obtained through the above HIL experiments.

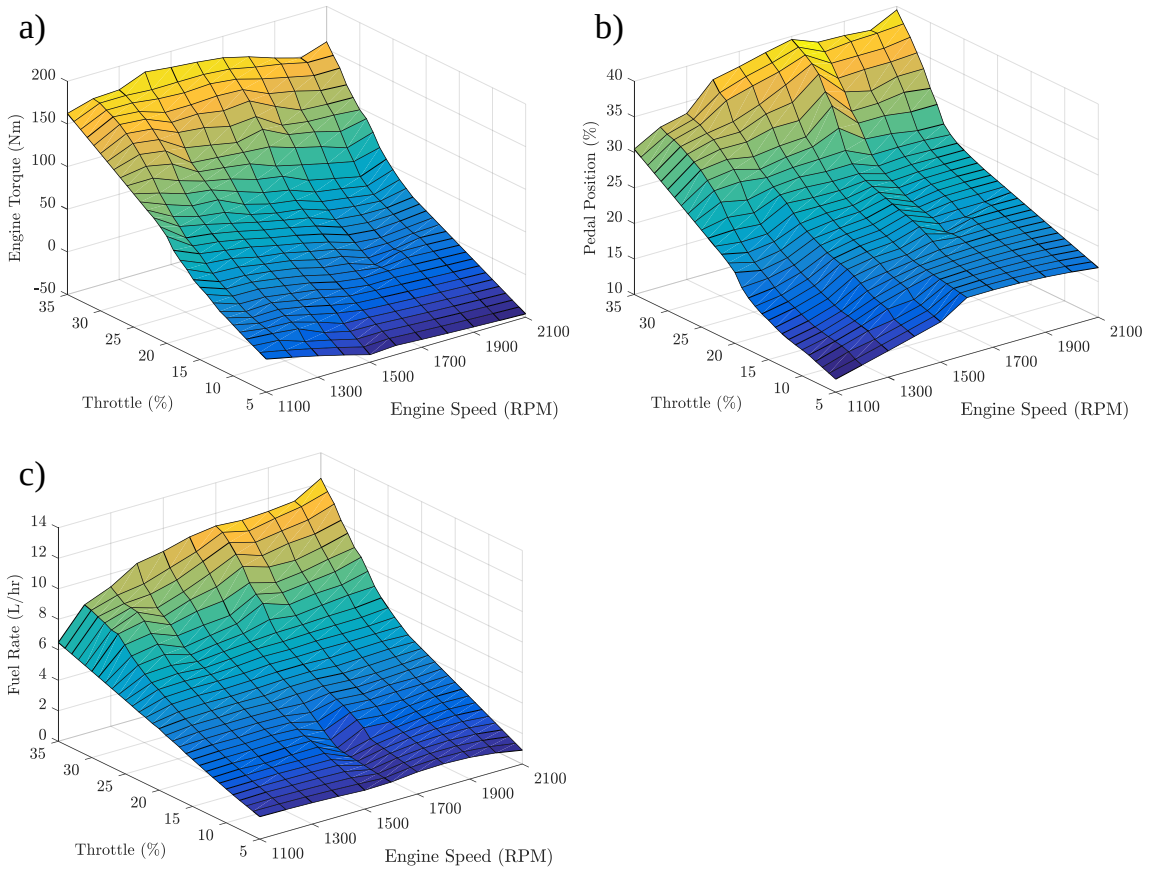


Figure 6.3 Engine maps: a) engine speed, throttle and torque map; b) engine speed, throttle and accelerator pedal map; c) engine speed, throttle and fuel consumption map

### 6.2.4. Transmission Model Development

The actual testing vehicle (2013 Cadillac SRX) utilizes the GM 6T70 Hydra-Matic six-speed automatic transmission [140]. An automatic transmission utilizes a shift schedule to determine the desired gear position and electronically control the gear ratio between the engine output shaft and the vehicle wheels. The shift schedule usually depends on the current vehicle speed and engine throttle position and it is determined by the car manufacturer through extensive calibrations to achieve objectives such as ride comfort, drivability and fuel economy. To match the performance of an actual vehicle, it is ideal to use the same shift schedule in the transmission model. However, this shift

schedule is not readily available. Therefore, the shift schedule is determined empirically using actual vehicle's data from a FHWA project [100,139]. The result is shown in Figure 6.4.

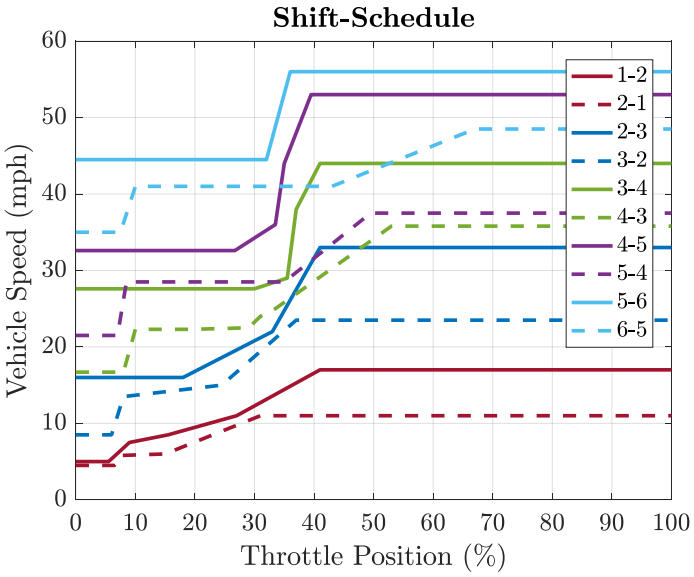


Figure 6.4 Empirical transmission shift schedule

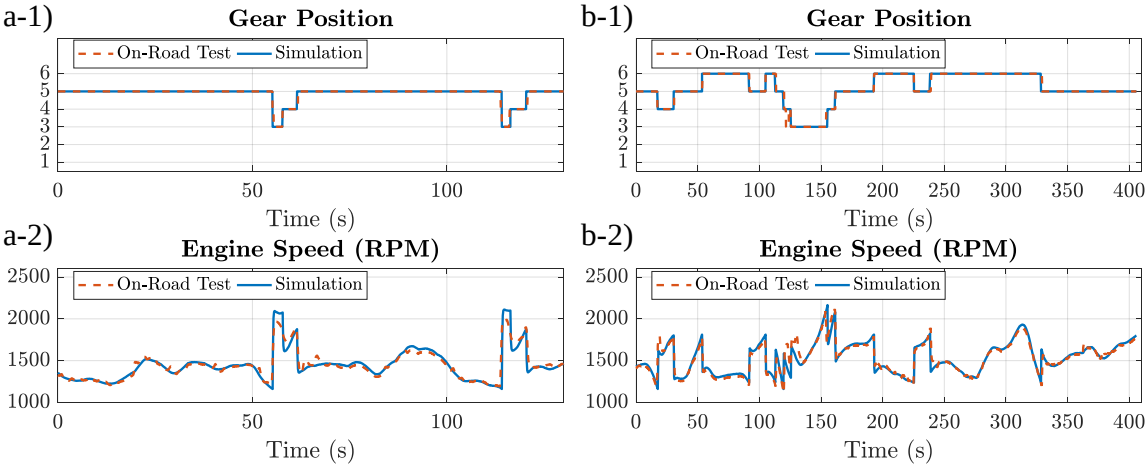


Figure 6.5 Transmission model calibration results: a) actual vehicle test one; b) actual vehicle test two

During the actual vehicle tests, all the vehicle speed, throttle position and gear position data were recorded. These data were used to determine a shift schedule. Essentially, it is to determine multiple curves of vehicle speed and throttle position relationships. The gear position changes when the operating points of vehicle speed and throttle position cross one of these curves. The first step was to extract actual vehicle data points whenever a gear-shift event occurs (i.e. the gear position changes). Next, curves of the shift schedule were obtained as piecewise linear curves that fit the extracted gear-shift event data points with the minimum error. Figure 6.5a-1 and Figure 6.5b-1 shows the calibration results for two actual vehicle test scenarios. The blue lines indicate gear positions obtained from the shift schedule. The recorded vehicle speed and throttle position data were sent to the shift schedule to find the gear positions. The red dashed lines indicate gear positions recorded from the actual vehicle. It can be seen that the two gear positions match well which verified the shift schedule.

In addition, parameters of the following powertrain model were determined:

$$\omega_e(t) = \frac{R_{fd} \cdot GR(t)}{R_{tire}} \cdot v(t) \tag{6.1}$$

where $\omega_e$ is the engine speed ($rad/s$); $GR$ is the transmission gear ratio; $R_{fd}$ is the final drive ratio; $R_{tire}$ is the wheel tire radius ($m$); $v$ is the vehicle speed ($m/s$). The values of all transmission gear ratios (six for the six-speed transmission) and final drive ratio were obtained from the brochure of the 2013 Cadillac SRX. The tire radius was calibrated since the actual tire radius can be slightly different from the brochure due to the deformation of the tire. The same actual vehicle data from FHWA were used. The inputs are vehicle speed and actual gear ratio, the output is the calculated engine speed from the powertrain model (6.1). The tire radius was determined to be the one that gives the minimum error between the calculated engine speed and the engine speed recorded from the actual vehicle. Calibration results from two actual vehicle testing scenarios are shown in Figure 6.5a-2 and Figure 6.5b-2. The blue lines indicate engine speeds

calculated from the powertrain model and the red lines indicate engine speeds recorded from the actual vehicle. It can be seen that the two engine speeds match well which verifies the powertrain model.

### 6.2.5. Vehicle Model Development

The vehicle and powertrain dynamics are governed by the following equations:

$$J_e \dot{\omega}_e(t) = T_e(t) - T_f(t) - T_d(t) \tag{6.2}$$

$$\underbrace{M_v a(t)}_{inertia\ resistance} = \frac{\overbrace{T_d(t) \cdot R_{fd} \cdot GR(t)}^{axle\ torque}}{R_{tire}} - \left( \underbrace{f_{tire} M_v g\ cos\ \varphi(t)}_{rolling\ resistance} + \underbrace{M_v g\ sin\ \varphi(t)}_{grade\ resistance} + \underbrace{\overbrace{\frac{1}{2} C_d \rho A}^{C_{wind}}\ v(t)^2}_{wind\ resistance} \right) \tag{6.3}$$

where $T_e$ is the engine torque ($Nm$); $T_f$ is the engine friction torque ($Nm$); $T_d$ is the engine loading torque ($Nm$); $a$ is the vehicle acceleration ($m/s^2$); $f_{tire}$ is the rolling resistance friction constant; $M_v$ is the vehicle mass ($kg$); $g$ is gravity constant; $\varphi$ is the road slope angle ($rad$); $C_d$ is the drag coefficient; $\rho$ is the air density ($kg/m^3$); $A$ is the vehicle frontal area ($m^2$).

From (6.2), to ensure the performance of the virtual target vehicle matches the performance of an actual testing vehicle, both the engine output torque and the engine loading torque need to be the same as the actual vehicle. The engine torque can be controlled by sending the same accelerator pedal command as the actual vehicle. However, the desired loading torque has to be estimated using (6.3) which includes several unknown parameters. As discussed in the previous section, the gear ratios and final drive values were already obtained from the brochure, and the tire radius was calibrated. The gravity constant is also a known constant. The remaining parameters that need to be calibrated are $f_{tire}$, $M_v$, and the lumped wind resistance constant $C_{wind}$.

These parameters were calibrated using the actual vehicle data from a FHWA project [100,139]. For a well calibrated vehicle model, the calculated engine loading torque from

(6.3) should match the engine loading torque of an actual vehicle, given the same vehicle trajectory and roadway condition. During the actual vehicle tests, all the vehicle speed, acceleration, roadway slope, and gear positions were recorded. These data were sent to (6.3) to obtain the calculated engine loading torque. Due to the difficulties in installing a torque sensor on an actual vehicle, the actual engine loading torque was not directly measured. It was estimated by an engine map using recorded engine speed and throttle of the actual vehicle. The model parameters of (6.3) were selected as those giving the minimum error between the calculated engine loading torque and the estimated actual engine loading torque. The initial guess were based on the brochure and the ranges of these parameters were referred to [11].

In total, two FHWA data sets were used to calibrate the model: Aberdeen Track scenarios (data set 1) and rolling terrain scenarios (data set 2). The data set 1 was conducted on a relatively flat roadway and the effects of road grade angles are limited. A flat roadway is ideal for the longitudinal model calibration since the model is sensitive to the grade resistance term. Even for a roadway with small grade angle, the grade resistance term can become dominant compared to other resistances. Therefore, the data set 1 was used at beginning to obtain a preliminary calibration of the parameters though the nonlinear least square method. Once this was done, the model was further calibrated using the data set 2.

Figure 6.6a shows one calibration result from data set 1 and Figure 6.6b shows one calibration result from data set 2. The blue lines are estimated actual engine loading torque and the red lines are calculated engine loading torque using (6.3). It can be seen that in both scenarios, the calculated engine loading torque match well with the estimated engine loading torque from actual vehicle data. This validates the vehicle model calibration. The root-mean-square-errors (RMSEs) are 3.08 and 18.30 respectively. The result from data set 2 has greater RMSEs due to more transient engine dynamins and more aggressive roadway slopes.

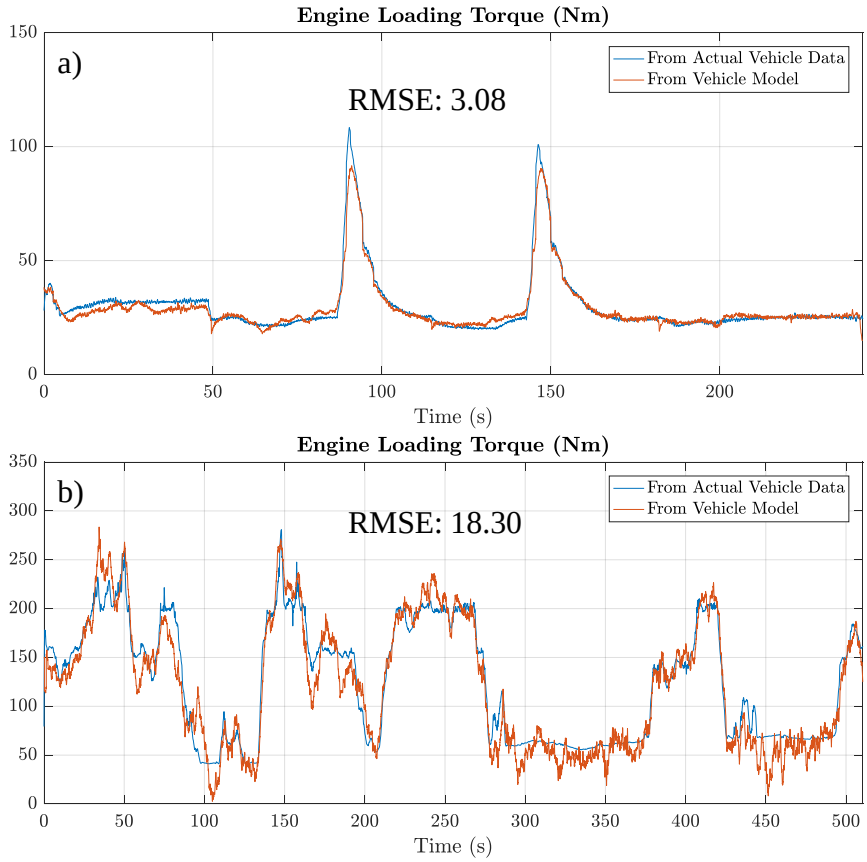


Figure 6.6 Vehicle model calibration results

### 6.2.6. Implementation

Once all models and controllers were calibrated and verified, the performance of the virtual target vehicle represented by the powertrain research platform was compared against the performance of an actual vehicle. Given a testing scenario, first the high-level controller calculates the desired accelerator pedal command and engine torque using the engine maps and the calibrated longitudinal model. Next, these commands plus vehicle performance data (vehicle's speed, acceleration, etc.) and the testing scenario's roadway conditions (speed limit, the degree of road slope, etc.) are sent to the middle-level controller to determine the desired loading torque using both powertrain and vehicle models. This loading torque plus a compensation term from an engine controller (as shown in Figure 6.1) determines the final desired loading torque. This engine controller is

a proportional-integral (PI) controller based on engine speed feedback and compensates for uncertainties of the powertrain and vehicle models. Finally, the engine loading pump is controlled to provide the loading torque. The actual engine speed and torque are measured and sent to the vehicle model to simulate the performance of the virtual vehicle. The fuel consumption and emissions of the virtual target vehicle are measured using precise instruments and recorded as well. The results of the HIL testbed validation are shown in Section 6.4.2.

## 6.3. Living lab Development

The living lab enables real-time traffic data communication (including loop detectors, traffic signal and vehicle data) between the actual roadway (testing field) and the HIL testbed. To enable thee real-time communication, a roadway segment has been equipped with a roadside unit (RSU) and a small number of testing vehicles are instrumented with onboard units (OBUs). The OBU collects the vehicle data in real-time (vehicle's location, speed, acceleration etc.) and broadcasts this information as basic safety message (BSM) to the RSU and the surrounding testing vehicles. The RSU broadcasts both traffic signal and loop detector data to the testing vehicles, and forwards all traffic data remotely to the HIL testbed. The HIL testbed can thus mimic a virtual target vehicle that follows an on-road testing vehicle in real-time to evaluate the performance of various CAV applications. The value of the living lab is that it enables the HIL testbed to access real-world traffic data. Therefore, the HIL testbed can evaluate various CAV applications in realistic world traffic scenarios. This is an important feature since simulated traffic scenarios from VISSIM may not accurately reflect the real-world situations due to difficulties in modeling the highly nonlinear and complex traffic dynamics. The HIL testbed can thus evaluate the real-time capability and robustness of various CAV applications in real-world traffic scenarios. It is neither restricted to simulated traffic scenarios nor to proving grounds scenarios. All the on-road testing vehicles are driven by

human on real-world roadways and they interact with all other traffic and signals just as normal vehicles will behave. Therefore, even though there are only a few instrumented vehicles, the traffic scenarios generated from the living lab are still from real traffic data.

### 6.3.1. Overview

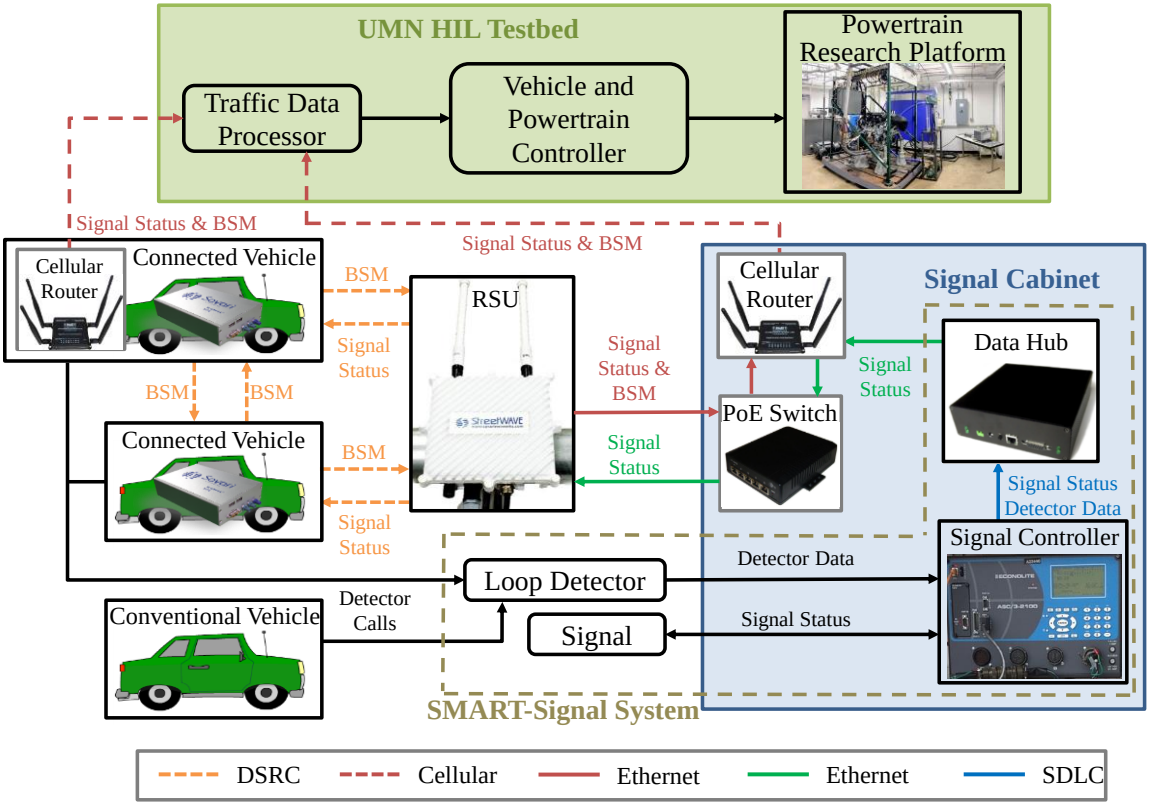


Figure 6.7 Overall architecture of the living lab

Figure 6.7 shows the overall architecture of the living lab. The signal information is obtained from the serial data link cable (SDLC) port of the signal controller. A SMART-signal system [141] is used to obtain both the signal status and detector data. Firstly, the signal controller sends signal status and detector data to the data hub through the SDLC. Then the data hub relays the data to the RSU through an Ethernet cable. The RSU processes and formats the data, and broadcasts to the surrounding testing vehicles through dedicated short range communication (DSRC) wirelessly. Meanwhile, the testing

vehicles forward BSMs to the RSU as well. Finally, the RSU combines signal status and loop detector data with the BSMs, and transmits to the HIL testbed using cellular network. As mentioned previously, the HIL testbed can thus evaluate the performance of a virtual target vehicle that follows one of the on-road testing vehicles. Depending on the specific CAV application, a vehicle and powertrain controller (essentially the high-level controller in Figure 6.1) controls the actual engine of the powertrain research platform to mimic the operation of the target vehicle's engine. Real-time fuel consumption and emissions are measured and recorded. Details of each component of the living lab will be further explained in the following sections.

If a testing vehicle is equipped with a cellular router, traffic data can alternatively be sent from the testing vehicle. The living lab has the capability to conduct HIL tests with real-time communication among traffic infrastructures, testing vehicles and a virtual target vehicle driven by a real engine. Example is shown in Section 6.4.3.2. The real traffic data can also be collected and stored for offline evaluation of CAV applications. Section 6.4.3.1 shows an eco-approach application as the example.

### 6.3.2. Intersection Instrumentation

The RSU has been instrumented at the intersection between Trunk Highway 55 (TH55) and Winnetka Ave in Minnesota (Figure 6.8a)). It is installed on the signal pole as close to the middle of the road as possible to ensure the best line-of-sight (Figure 6.8b)). An inside view of the instrumented signal cabinet is shown in Figure 6.8c). The inside view essentially shows actual connections inside the signal cabinet among components illustrated in Figure 6.7. The Data Hub connects to the signal controller (Econolite ASC/3-2100) through a SDLC cable. The RSU (Savari StreetWAVE) is powered using a long Ethernet cable routed from the signal cabinet. This Ethernet cable sits securely inside the signal pole and the cable tunnels underground. The RSU and Data

Hub are connected through a cellular router (Mofi Network 4500). Using this router, the RSU can forward traffic data remotely to the HIL testbed.


Figure 6.8 Living lab intersection instrumentation: a) location of the instrumented intersection (between Trunk Highway 55 and Winnetka Ave); b) view of the RSU mounted on the signal pole; c) inside view of the instrumented signal cabinet

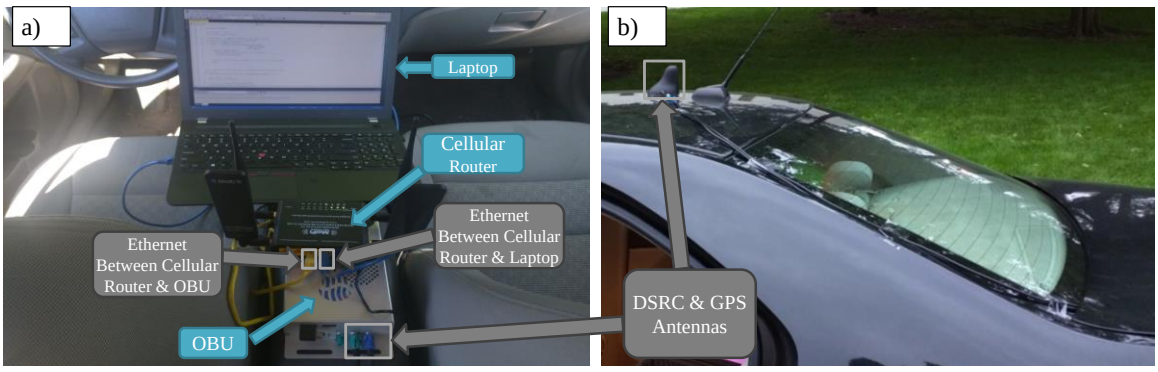


Figure 6.9 Living lab testing vehicle instrumentation: a) inside view of the instrumented vehicle; b) roof view of the instrumented vehicle

### 6.3.3. Testing Vehicle Instrumentation

Figure 6.9a) and Figure 6.9b) show the instrumentation of a testing vehicle. The OBU (Savari MobiWAVE) has been installed to obtain vehicle speed, location (longitude and latitude) and altitude (road slope) information based on Global Positioning System (GPS). This information is then formatted as BSM data following the SAE J2735 standard [142]. The BSM is broadcasted to the RSU every 0.1 second using the DSRC. The OBU also receives signal status and loop detector data from the RSU. The GPS and DSRC antenna of the OBU sit on the top of the vehicle roof to ensure a good signal reception. If a cellular router is equipped in the testing vehicle, the traffic data can be transmitted remotely to the HIL testbed from the OBU. In addition, a laptop or a tablet can be connected to the OBU through the Ethernet port or the RS-232 port. Thus a human machine interface can be developed to display real-time vehicle data and signal data to the driver or provide driving guidance.

### 6.3.4. Integration to the HIL Testbed

The value of the living lab is that it enables the HIL testbed to access real-world traffic data. Therefore, the HIL testbed can evaluate various CAV applications in realistic world traffic scenarios. Integration of the living lab and the HIL testbed extends the capabilities of the HIL testbed for various CAV applications evaluation. There are two usages of the living lab. In the first usage, real-world traffic data are collected from the living lab first before conducting the HIL tests. Then the HIL testbed can evaluate the performance of a target vehicle in realistic traffic scenarios. In the second usage, the HIL testbed and the living lab interact in real-time through real-time communication. The HIL testbed sends real-time information of the target vehicle as the feedback to affect the performance of on-road testing vehicles or the signal controller. In addition, the HIL testbed can evaluate CAV applications in more realistic environments. A key value brought by the HIL testbed is that the vehicle powertrain dynamics is explicitly

considered by installing the actual engine and well calibrated vehicle model. The real-time capability and the robustness of a CAV controller can be evaluated realistically with considerations such as prediction uncertainties, communication delays, etc. The HIL testbed can function as a rapid prototyping platform to validate whether the CAV controller would perform as expected if implementing on an actual vehicle.

If the living lab is used to generate real traffic data and the HIL testbed uses the collected data later, real-time communication is not an issue. But if the living lab and the HIL testbed need to interact in real time, then communication delay has to be considered. The delay can be avoided by using a wired network. Both the HIL testbed and the living lab (the signal controller and the RSU) will be connected to the internet through wired network. The on-road testing vehicles will communicate with the RSU through DSRC. Therefore, they can share information using network communication such as TCP/IP and the delays are minimal [55]. With the current setup, the delays can be considered by the CAV controllers. Essentially, delays affect the quality of the traffic information and thus bring more uncertainties in the traffic prediction. The controller should be robust to ensure satisfactory performance even with the existence of these uncertainties. This can be addressed by using robust optimization methods to consider the uncertainties explicitly during the controller design [143] or model predictive control (MPC) to update traffic information frequently.

## 6.4. Experiment results and discussion

### 6.4.1. Capabilities of the HIL Testbed and the Living Lab

The HIL testbed has three potential usages:

1) *Evaluate the performance of a target vehicle inside the VISSIM simulated traffic network.* Any vehicle from the simulated traffic scenario can be selected as the target vehicle and the HIL testbed can accurately evaluate its performance. If multiple vehicles are of interest, each vehicle can be evaluated one-by-one and multiple HIL experiments

can be conducted. With a simulated traffic network, various complex traffic scenarios can be evaluated and there could be one or multiple CAVs. There could be other vehicles following the target CAV emulated by the HIL testbed and the benefits of CAVs to the overall traffic (or the mobility benefits of CAVs) can be understood.

2) *Evaluate the performance of a target vehicle in real-world traffic scenarios.* Real-world traffic scenarios are generated first using recorded on-road testing vehicle data and signal data from the living lab before conducting the HIL experiments. Once a real-world traffic scenario is generated, the HIL testbed will emulate a target vehicle that follows one of the on-road testing vehicles. This enables evaluating the target vehicle in realistic traffic scenarios. Simulated traffic scenarios from software such as VISSIM may not accurately reflect the real-world situations due to the difficulties in modeling the highly nonlinear and complex traffic dynamics. The HIL testbed can be a rapid prototyping platform to evaluate and compare different CAV control strategies in real-world traffic scenarios.

3) *Evaluate the performance of a target vehicle that interacts with real traffic in real-time.* In this setup, again the HIL testbed emulates a target vehicle that follows one of the on-road testing vehicles. The difference is that the HIL testbed shares information (both receiving and sending information) with the living lab in real-time. This means that the HIL testbed can send real-time information of the target vehicle as the feedback to affect the performance of on-road testing vehicles or the signal controller. This setup is more close to the real-world implementation situations. The real-time capability and the robustness of the CAV controller can be evaluated realistically as well with considerations such as prediction uncertainties, communication delays, etc.

For the real-time usage of the living lab (the third usage), one example application is the coordinated control of a vehicle platoon. The target vehicle (HIL testbed) will follow a platoon of on-road testing vehicles and send its future control decisions to these preceding vehicles. The preceding vehicles will affect the fuel consumption of the target

vehicle. By considering the traffic information behind themselves, the preceding vehicles can be driven to achieve the maximum energy benefits of the entire vehicle platoon. However, safety concerns have to be carefully considered in this application. The on-road testing vehicles can be either human-driven vehicles with speed advisory or autonomous vehicles. Another example application is the adaptive signal control. The HIL testbed can send the optimal SPaT to the signal controller based on information from both the target vehicle and the on-road testing vehicles. Therefore, the signal controller can adapt to the status of the target vehicle to improve energy efficiency and mobility.

The development of the living lab enables the second and third usages. The mobility benefits of CAVs can be evaluated for VISSIM simulated traffic networks (the first usage). The key is that any vehicle from the VISSIM simulation can be selected as the target vehicle and the HIL testbed can accurately evaluate its performance. For example, if a platoon of vehicles is of interest with mixed CAVs and non-CAVs, each vehicle in the platoon can be evaluated one-by-one with multiple HIL experiments. Therefore, performance of all vehicles in the platoon can be understood which would reveal the mobility benefits of CAVs. The HIL testbed can be potentially used for evaluating safety benefits as well with further enhancement. For example, latency is more critical for a safety focused CAV application. When interacting with on-road testing vehicles in real-time, the communication delays may need to be minimized. The evaluation of safety benefits is out of the scope this work.

The HIL testbed is designed to be able to swap different types of engines and accommodate different vehicle models. Our group has tested a diesel engine [101] and a Ford gasoline engine [119] on the HIL testbed before with different vehicle models, such as a hybrid electric vehicle [55]. The current GM gasoline engine is installed since it matches the actual testing vehicles at FHWA and therefore allows us to compare directly the HIL testbed with the actual testing vehicles.

In the following sections, Section 6.4.2 validates that the HIL testbed can match the performance of actual vehicles which significantly improves the credibility of the HIL testbed. Section 6.4.3 shows two examples to demonstrate the second and third capabilities of the HIL testbed which are enabled by the living lab.

### 6.4.2. Match the Performance of the Actual Testing Vehicle

In this section, experiments are conducted on the HIL testbed to compare its performance against the actual testing vehicle at the FHWA. Actual vehicle tests have been conducted on the CAV platform of the FHWA [100,139]. Fuel measurement devices were equipped on the actual testing vehicle and the fuel saving benefits of an eco-drive control algorithm developed in [7] were compared with a conventional constant-speed cruise control on several roadways in Virginia. To evaluate the performance of the HIL testbed against the actual vehicle, eight representative testing scenarios was selected and tested on the HIL testbed. Both eco-drive and baseline scenarios were included for four different roadways. The summary of fuel consumption results are shown in Table 6-1. Overall, the virtual vehicle represented by the HIL testbed has similar fuel consumption as the actual vehicle. The HIL testbed achieved similar fuel benefits (between the baseline scenario and the eco-drive scenario) as the actual testing vehicle with about 1% error. These results validate the effectiveness and accuracy of the HIL testbed.

For all road scenarios, performance of the virtual vehicle matches well with the performance of the actual testing vehicle. The simulated vehicle speeds from the HIL testbed match the actual vehicle speeds which validated the calibrated transmission and vehicle models. Both the engine speeds and throttles were tracked well which ensures the resulting engine torque and fuel consumption match those of the actual testing vehicle. All these results validate that the HIL testbed can match the performance of the actual testing vehicle with high accuracy.

Table 6-1 Summary of all testing scenarios

| Road Scenario | Scenario | Actual Vehicle Test | | | HIL Test | | |
|---|---|---|---|---|---|---|---|
| | | Travel Time (sec) | Fuel (L) | Fuel Benefits (%) | Travel Time (sec) | Fuel (L) | Fuel Benefits (%) |
| River Northbound | Baseline | 365.6 | 0.690 | 8.2 | 365.58 | 0.674 | 9.3 |
| | Eco-drive | 405.8 | 0.633 | | 405.78 | 0.611 | |
| Georgetown Pike Northbound | Baseline | 160.6 | 0.204 | 11.3 | 160.59 | 0.208 | 10.6 |
| | Eco-drive | 163.0 | 0.181 | | 162.99 | 0.186 | |
| GW Parkway Southbound | Baseline | 641.5 | 0.904 | 8.1 | 641.48 | 0.900 | 7.2 |
| | Eco-drive | 648.7 | 0.831 | | 648.68 | 0.835 | |
| US 17 Northbound | Baseline | 469.8 | 0.921 | 4.2 | 465.57 | 0.938 | 3.7 |
| | Eco-drive | 510.5 | 0.882 | | 510.47 | 0.903 | |

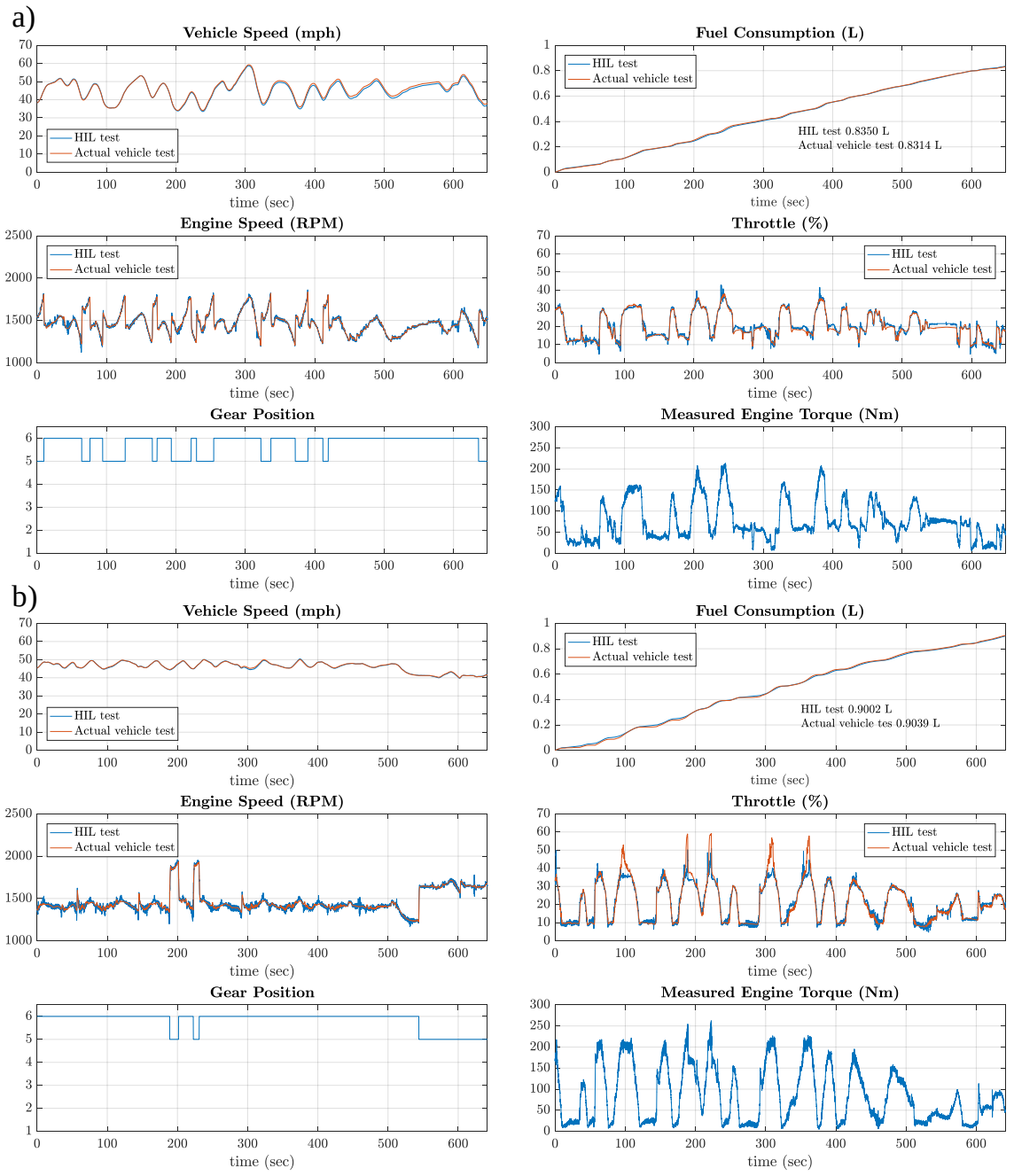


Figure 6.10 HIL testing results for gw parkway: a) eco-drive scenario; b) baseline scenario

Figure 6.10 shows the HIL testing results for the GW Parkway scenario. It can be seen that the simulated vehicle speed matches the actual testing vehicle's speed, and both

the engine speed and throttle tracks well. Note that there are several high throttle regions where the throttle positions were not tracked perfectly. It turns out that in these regions, the throttle positions are sensitive to changes of the pedal positions, while the engine torque is not sensitive to the throttle positions. In other words, when the pedal varies a small amount, the throttle can vary significantly but the increase on engine torque is small. Therefore, effects of these regions on the vehicle performance and fuel consumption are small. The engine torque data were not measured during all actual vehicle experiments due to difficulties in installing a torque sensor on an actual vehicle. In addition, for the particular test scenario shown in Figure 10, gear position data were not recorded by the FHWA. Nevertheless, it is anticipated that both the gear position and engine torque data from the HIL testbed would reflect the performance of the actual vehicle with high fidelity. This is because both the powertrain and vehicle models used in the HIL testbed have been well calibrated and their accuracy has been demonstrated in Section 2.4 and Section 2.5

### 6.4.3. Demonstration of the Living Lab

To demonstrate the capabilities brought by the living lab, two experiments were conducted. The first experiment is an eco-approach application. The trajectory of the preceding vehicle was recorded from on-road testing vehicles driven by human drivers in real world traffic scenario on the TH55 (the instrumented roadway). The HIL testbed emulates the operation of a target vehicle that follows the preceding vehicle to pass an intersection, and the performance of the target vehicle is compared with the performance of the immediate preceding vehicle. The second experiment shows the real-time capability of the living lab. The HIL testbed mimics a target vehicle that exactly follows a testing vehicle driven by a human driver on a real road in real-time.

*6.4.3.1. Eco-approach application*

The experiment setup is shown in Figure 6.11. Three actual testing vehicles instrumented with on-board units (OBUs) were driven by human drivers to pass a real-world intersection at trunk highway 55 (TH55) in Minnesota. The OBUs collect vehicle data such as each vehicle's location, speed and acceleration. The intersection is instrumented with a roadside-unit (RSU) [144]. The RSU is connected to the signal controller and obtains signal phase and timing (SPaT) and information from detectors. The location and speed of these vehicles and the signal phase and timing were recorded and synchronized. Slopes of the real-world roadway were obtained using the elevation data from the Minnesota Geospatial Information Office (MnGeo) [145].

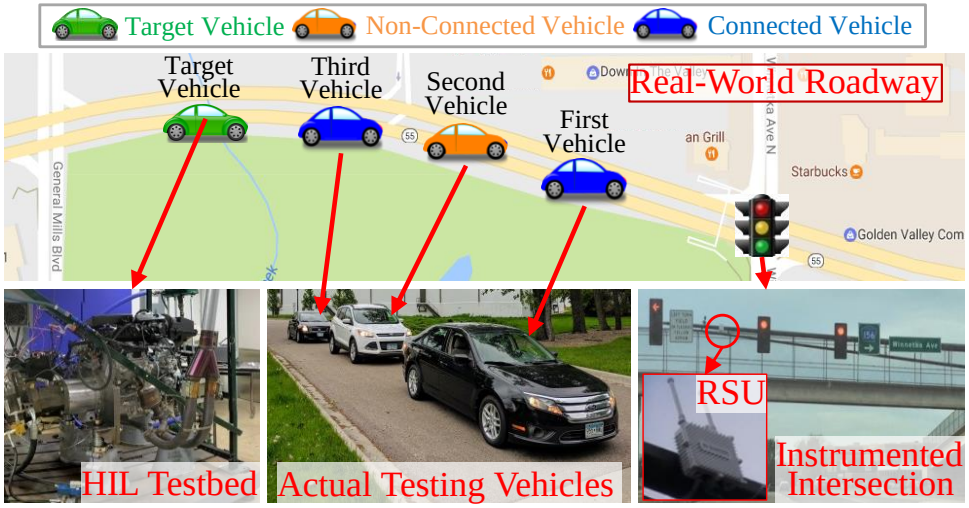


Figure 6.11 Illustration of the real-world traffic scenario

With these data, any vehicle of the three testing vehicles can be treated as a human-driven CV or a non-CV. The HIL testbed will then emulate a virtual target vehicle that follows these preceding vehicles to pass the intersection. In this work, it is assumed that the first and the third vehicles are human-driven CVs, and the second vehicle is a non-CV (see Figure 6.11). The target vehicle follows the third vehicle in the platoon (see Figure 6.11). This third vehicle is driven by a human driver and is considered as the baseline. Even though data of all three vehicles were recorded, the target vehicle (the HIL

testbed) will only know information of those selected as CVs. There could be other vehicles on the road but the target vehicle will not know whether those vehicles exist and their locations. The target vehicle uses information of the two preceding human-driven CVs and signal phase and timing to predict the future traffic conditions. It is assumed that the communication range between the target vehicle and the intersection is 500 meters. Therefore, the target vehicle begins eco-approach 500 meters away from the intersection and the roadway of interest is 500 meters. This roadway is divided into 40 cells and each cell is 12.5 meters. Partial traffic states 'measured' from the two CVs are used to estimate the traffic states of all 40 cells using the observer (developed in Section 2.2). Then the traffic flow model is propagated forward in time to predict the future traffic conditions. With this real-world traffic data, the optimal control (see Chapter 3) can be evaluated in a realistic scenario for a target vehicle passing a real-world intersection. The scenario considers mixed traffic with both CVs and non-CVs on the road. The experimental validation on the HIL testbed helps validate the energy benefits of the optimal control with measured fuel consumption and emissions of the target vehicle.

Table 6-2 Fuel consumption of all evaluation scenarios

| | ***Baseline*** | ***Target-Speed Optimization*** | ***Target*** | ***Target-Ideal*** |
|---|---|---|---|---|
| Fuel Consumed (grams) | 43.2 | 39.6 | 36.1 | 33.3 |
| Energy Benefits (%) | - | 8.3 | 16.5 | 23.0 |

Table 6-2 shows the fuel consumption comparison of all evaluation scenarios. The scenarios are as followings: 'Baseline' is the performance of the third vehicle in Figure 6.11 (the immediate preceding vehicle); 'Target' is the performance of a vehicle with optimal speed and gear position control (see Chapter 3) and traffic prediction (see Chapter 2), the vehicle is emulated by the HIL testbed; 'Target-Ideal' is the performance of a vehicle with optimal speed and gear position control but is assumed to perfectly

know the future traffic; ‘Target-Speed Optimization’ is the performance of a vehicle with optimal speed control and the same shift schedule as the ‘Baseline’ vehicle.

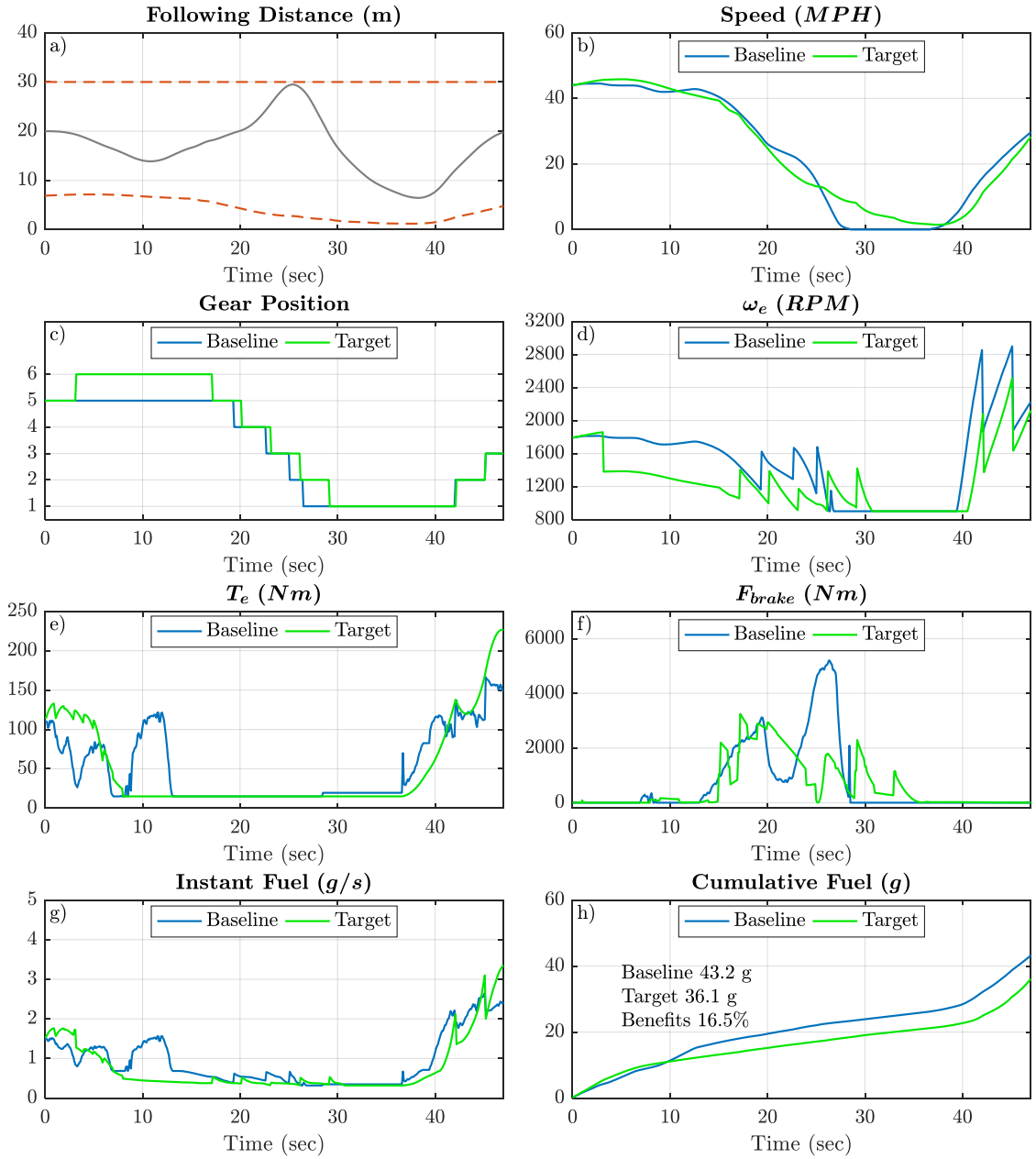


Figure 6.12 Comparison of preceding vehicle (‘Baseline’) and ‘Target’ vehicle

Figure 6.12 shows the comparison between the ‘Target’ vehicle and the preceding vehicle (‘Baseline’). The ‘Target’ vehicle receives speed and location information from preceding connected vehicles as well as signal phase and timing from the signal lights.

With co-optimization of vehicle speed and gear position, it can achieve 16.5% benefits. The ‘Target’ vehicle is able to reduce braking when approaching the intersection and accelerate smoother when leaving the intersection. The braking reduction is 13.4% (Figure 6.12f). The ‘Baseline’ vehicle has to stop at the intersection for 8 seconds and has a more dynamic speed profile. Besides benefits from the optimized vehicle speed, gear position is optimized. The ‘Target’ vehicle anticipates the future power request and stays longer at higher gears to operate the engine in more efficient operating points (e.g. gear six during 3 seconds to 18 seconds). Considering the ‘Target-Speed Optimization’ vehicle that is driven with the optimal vehicle speed of the target vehicle and the fixed shift schedule of the preceding vehicle, the fuel benefit is 8.3%. In other words, with optimization of gear position, an additional 8.2% benefit is achieved. This shows that gear position optimization contribute to almost half of the total energy benefits (16.5%) for the ‘Target’ vehicle.

Figure 6.13 shows the comparison of ‘Target-Ideal’ scenario and ‘Target’ scenario. In the ‘Target-Ideal’ scenario, with perfect future traffic information, the vehicle tends to stay longer near the upper bound of following distance which fully utilizes the following distance spacing freedom. The energy wastes from braking and idling are significantly reduced. Since the braking is reduced, the vehicle needs to accelerate less after the signal turns green which saves energy. The fuel saving is 23.0%. For the ‘Target’ scenario, even with imperfect traffic prediction, the vehicle is able to reduce waste from braking and idling. But the speed profile is more dynamic with more ups and downs (also refer to Figure 6.12b), and thus the power request is increased. Nevertheless, the controller achieves 16.5% fuel benefit which is satisfactory comparing to the ‘Target-Ideal’ scenario. For the gear position optimization, the ‘Target-Ideal’ vehicle is able to stay on higher gears longer than the ‘Target’ vehicle with prediction. This helps to operate the engine in more efficient regions and hence reduce energy consumption.

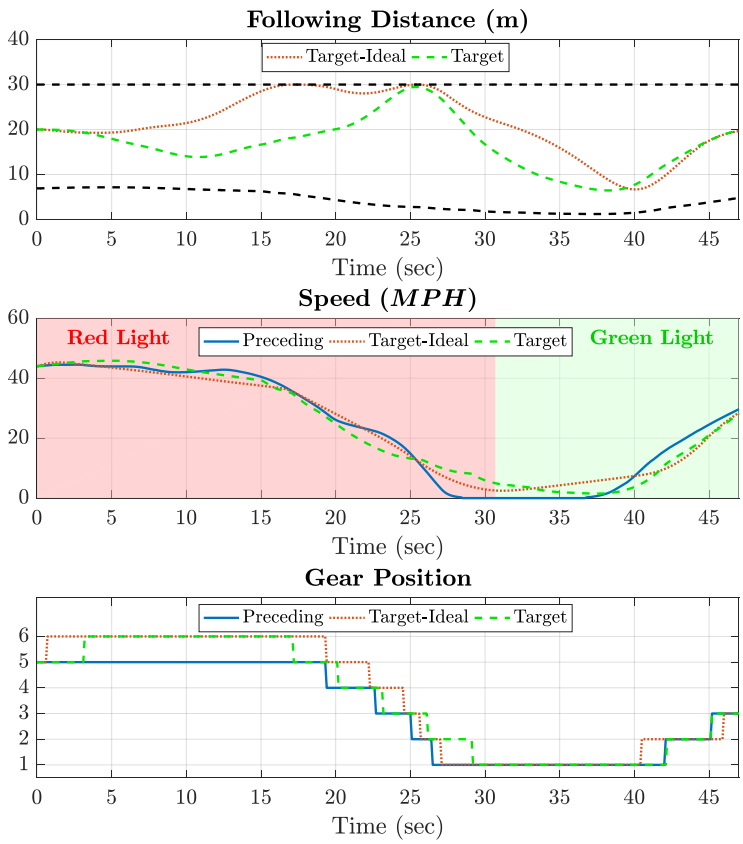


Figure 6.13 Perforamnce of 'Target-Ideal' vehicle with perfect future traffic information versus 'Target' vehicle with predicted traffic for the real-world traffic scenario

Figure 6.14 shows the powertrain dynamics of the 'Baseline' scenario and 'Target' scenario recorded on the HIL testbed. It can be seen that both the measured engine speed and engine torque match well with the reference profile. The simulated vehicle speed matches the reference vehicle profile as well. All these results validate the performance of the proposed optimal controller. The measured fuel consumption rates are shown in the figure and the total grams of consumed fuels are shown in the orange texts. The actual fuel consumption has deviations from the fuel consumption estimated from the engine fuel map, especially during transient when the engine is commanded to throttle up or throttle down rapidly. The HIL testbed is effective in measuring these transients which cannot be captured by the engine fuel map. This shows the capability of the HIL testbed. The total fuel consumptions of the HIL measurement and the engine fuel map are similar.

This is because the deviations of the fuel consumption are offset during the eco-approach. The engine fuel map tends to underestimate the fuel consumption during vehicle acceleration, and overestimate the fuel consumption during vehicle deceleration. During the eco-approach, the vehicle completes exactly one deceleration and one acceleration. This offset the inaccuracies in the engine fuel map.

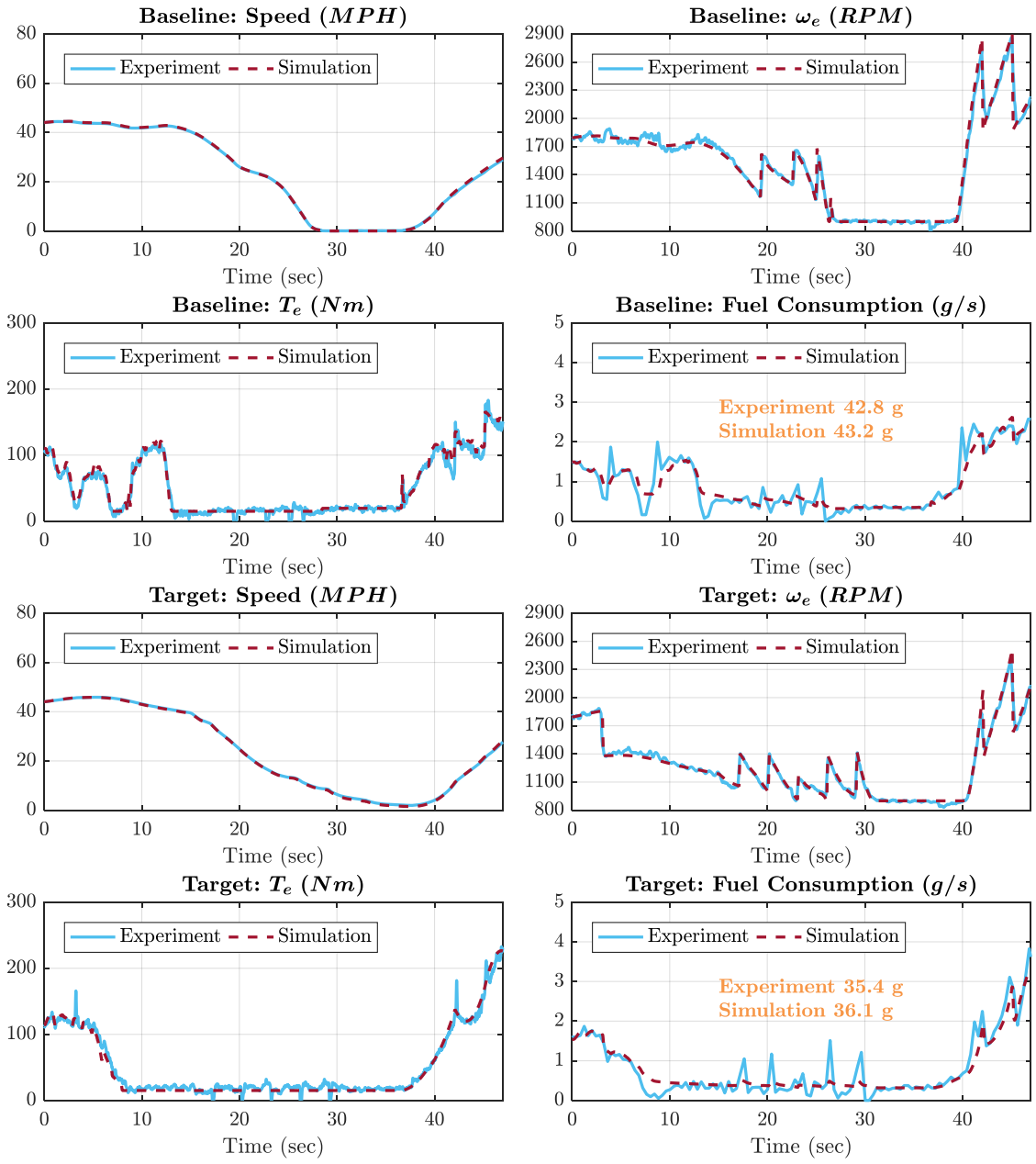


Figure 6.14 Experimental results for the real-world traffic scenario

*6.4.3.2. Real-time vehicle following*

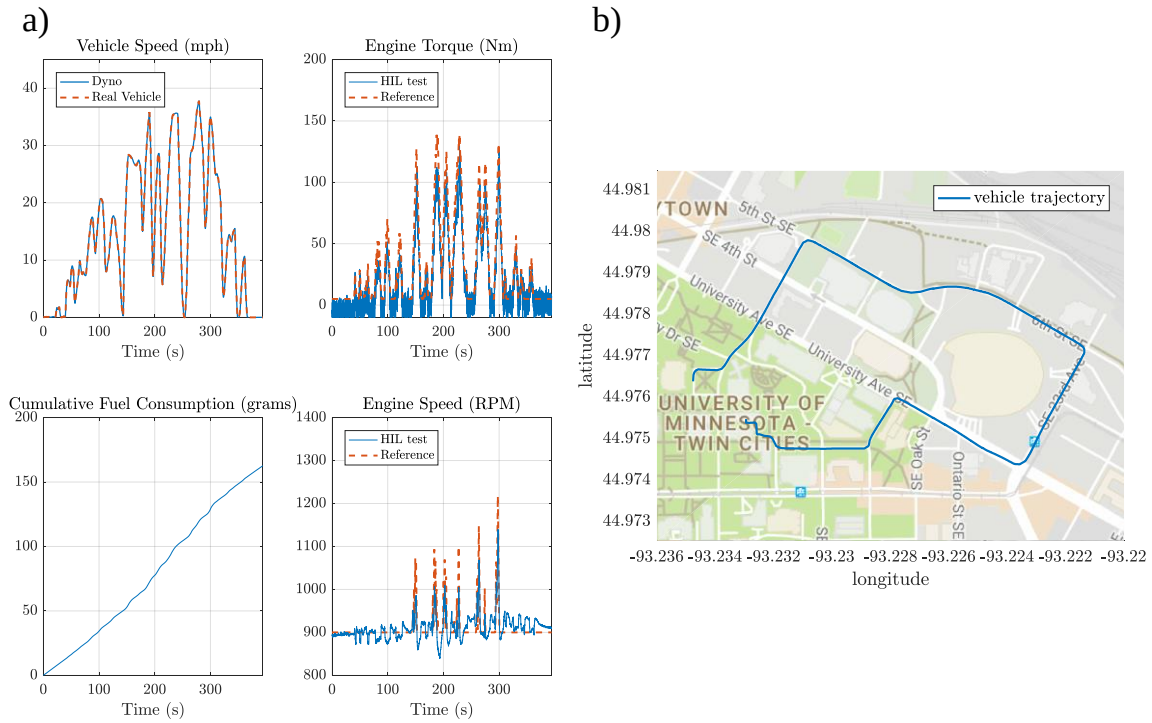


Figure 6.15 Real-time vehicle following using living lab: a) real-time vehicle following performance; b) trajectory of the on-road testing vehicle

In this application, an on-road testing vehicle was driven by a human driver around the University of Minnesota campus. The HIL testbed receives the on-road testing vehicle's speed in real-time to represent a target vehicle that follows exactly the testing vehicle. The high-level controller of the HIL testbed commands the emulated target vehicle to travel at the same speed as the on-road testing vehicle. To handle possible communication delays, at each time step, the control command will update only when there is new speed information from the on-road testing vehicle. If not, the same speed control command as the previous time step will be sent to the HIL testbed. The vehicle following performance of the HIL testbed is shown in Figure 6.15a) and the trajectory of the testing vehicle is shown in Figure 6.15b). It can be seen from the vehicle speed plot that the target vehicle speed tracks the on-road testing vehicle well. This demonstrated the real-time capability of the living lab.

## 6.5. Conclusion

In this work, the HIL testbed developed previously has been enhanced to match the performance of an actual testing vehicle. The same type of engine used in the actual vehicle was installed on the HIL testbed. All vehicle and powertrain models were calibrated using the actual vehicle testing data from the FHWA. In addition, a living lab was developed to enable the HIL testbed to interact with real traffic in real-time. After these configurations, HIL experiments were conducted for eight testing scenarios. The results show that the virtual target vehicle represented by the HIL testbed matches well with the performance of the actual testing vehicle with only about 1% error. The results significantly improve the credibility of the HIL testbed. The introducing of real-world traffic information extends the capabilities of the HIL testbed to evaluate the real-time capability and robustness of various CAV applications in realistic roadway conditions.

The research outcome provides a new, effective way to evaluate the vehicle fuel consumption and emissions for connected and autonomous vehicles (CAVs) and other types of vehicles in various roadway conditions. The capability of the living lab has demonstrated that it can handle various real traffic scenarios with no safety concerns.

# Chapter 7

# Conclusion and Future Work

## 7.1. Conclusion

In this dissertation, real-time implementable optimal control strategies are developed for energy savings of CAVs for three most common powertrain types today: internal combustion engine based vehicles (ICVs), hybrid electric vehicles (HEVs), and electric vehicles (EVs). Both the vehicle speed trajectory and powertrain operation (e.g. transmission gear position or engine-battery power-split) are optimized to maximize the energy benefits. The optimization is designed for each specific powertrain type considering impacts of powertrain operation, constraints and dynamics on the energy consumption. This ensures the optimal control law is realistic and can be potentially implemented on the actual vehicle. A systematic control framework, which combines both traffic prediction and energy optimization, is developed to implement the optimal control in the model predictive control (MPC) fashion. The traffic prediction method can be applied to scenarios where both connected and non-connected vehicles are on the road. A traffic flow model is used to describe dynamics of the traffic states (traffic density and traffic speed). Current traffic states are estimated using an observer based on real-time information communicated from connected vehicles and signal lights. Future traffic states can be predicted by propagating the traffic flow model forward in time. Uncertainties in the traffic prediction are considered during the vehicle speed optimization to ensure the performance of the optimal control strategy.

To experimentally validate the optimal control strategies, a HIL testbed developed previously has been enhanced. To increase the fidelity of the testbed, the same type of engine as the actual vehicle is installed and both vehicle and powertrain models are calibrated using actual vehicle testing data. The resulting HIL testbed matches well with

the performance of the actual testing vehicle with only about 1% error. In addition, a living lab was developed to enable the HIL testbed to interact with real traffic. The results significantly improve the credibility of the HIL testbed. The introducing of real-world traffic information extends the capabilities of the HIL testbed to evaluate the real-time capability and robustness of various CAV applications in realistic roadway conditions.

The control strategies have been evaluated for vehicles of each powertrain type in different traffic scenarios. Significant energy savings (10-20%) have been shown in experiment and/or simulation with the co-optimization. This validates the performance and potential benefits of the proposed vehicle speed and powertrain operation optimization strategies.

## 7.2. Future Work

In this dissertation, the optimal control strategies are mostly evaluated for a single lane roadway and for an individual vehicle. In reality, the roadway can be multi-lane and there can complicated traffic behaviors exist. It is of interest to extend the optimal control strategies to other CAV applications and complex traffic scenarios such as a multi-lane roadway with lane-changing. This will require an improved traffic prediction method that can model, for example, the lane-changing behaviors and predict the impacts of these behaviors on the traffic dynamics. Also, the performance and accuracy of the traffic prediction method can be potentially improved with additional information such as sensor data from perception (camera, LIDAR, etc.) and with advanced observer design (e.g. other nonlinear observers besides Kalman filter). It is also interesting to compare the traffic prediction method with data-driven approaches based on machine learning and artificial Intelligence (AI). For more complex scenarios, the performance of the optimal control can have higher dependency on the accuracy of the traffic prediction. This requires a detailed analysis on how the uncertainties of traffic prediction will affect the

optimality of the model predictive control (MPC), and how to ensure the energy benefits of the control through systematic robust or stochastic optimization.

In addition, the overall performance of the traffic network depends on not only the performance of each individual vehicle but also the entire vehicle platoon on the roadway and their interactions (e.g. as shown in [146]). There can be two potential directions: one is a systematic study to understand the impacts of CAV applications for energy savings on the traffic flow dynamics; the other one is to develop coordinated individual vehicle controller that considers the impacts on overall traffic to maximize the energy efficiency of the entire traffic. The instrumentation of multiple real-world intersections (extending the living lab) can help bring in more traffic data to facilitate these research studies.

There are other specific future works for different types of vehicles. For the optimal control of HEVs, it is of interest to conduct HIL experiment to validate the performance of the control (similar to the ICVs shown in Chapter 3). A representative HEV engine can be installed on the HIL testbed. The corresponding HEV vehicle and powertrain models can be calibrated using data from an actual vehicle or using the detailed calibrated models from Autonomies or Advisor (as in [147]). For EVs, the optimal control can be improved by introducing thermal dynamics of the battery, and considering the battery aging due to internal resistance increase.

## Bibliography


[1] US EPA, "Sources of Greenhouse Gas Emissions" [Online]. Available: https://www.epa.gov/ghgemissions/sources-greenhouse-gas-emissions. [Accessed: 16-Jul-2019].

[2] U.S. Energy Information Administration (EIA), 2017, *International Energy Outlook 2017*.

[3] U.S. DOT Bureau of Transportation Statistics, "Average Fuel Efficiency of U.S. Light Duty Vehicles" [Online]. Available: https://www.bts.gov/content/average-fuel-efficiency-us-light-duty-vehicles. [Accessed: 16-Jul-2019].

[4] United States Department of Transportation, 2015, "Connected Vehicle Applications" [Online]. Available: https://www.its.dot.gov/pilots/cv_pilot_apps.htm. [Accessed: 14-Aug-2018].

[5] Shao, Y., Mohd Zulkefli, M. A., and Sun, Z., 2017, "Vehicle and Powertrain Optimization for Autonomous and Connected Vehicles," Mech. Eng., **139**(09), pp. S19–S23.

[6] Jin, Q., Wu, G., Boriboonsomsin, K., and Barth, M. J., 2016, "Power-Based Optimal Longitudinal Control for a Connected Eco-Driving System," IEEE Trans. Intell. Transp. Syst., **17**(10), pp. 2900–2910.

[7] Hu, J., Shao, Y., Sun, Z., Wang, M., Bared, J., and Huang, P., 2016, "Integrated Optimal Eco-Driving on Rolling Terrain for Hybrid Electric Vehicle with Vehicle-Infrastructure Communication," Transp. Res. Part C Emerg. Technol., **68**, pp. 228–244.

[8] Sun, X., and Yin, Y., 2019, "Behaviorally Stable Vehicle Platooning for Energy Savings," Transp. Res. Part C Emerg. Technol., **99**, pp. 37–52.

[9] Vahidi, A., and Sciarretta, A., 2018, "Energy Saving Potentials of Connected and

Automated Vehicles," Transp. Res. Part C Emerg. Technol., **95**, pp. 822–843.

[10] Bai, S., Maguire, J., and Peng, H., 2013, *Dynamic Analysis and Control System Design*, SAE International.

[11] Sun, Z., and Zhu, G. G., 2014, *Design and Control of Automotive Propulsion Systems*, CRC press.

[12] Yang, Z., Feng, Y., Gong, X., Zhao, D., and Sun, J., 2019, "Eco-Trajectory Planning with Consideration of Queue along Congested Corridor for Hybrid Electric Vehicles," Transp. Res. Rec.

[13] Shao, Y., and Sun, Z., 2018, "Optimal Eco-Approach Control With Traffic Prediction For Connected Vehicles," *ASME 2018 Dynamic Systems and Control Conference, DSCC 2018-9059*.

[14] Ye, F., Hao, P., Qi, X., Wu, G., Boriboonsomsin, K., and Barth, M. J., 2019, "Prediction-Based Eco-Approach and Departure at Signalized Intersections with Speed Forecasting on Preceding Vehicles," IEEE Trans. Intell. Transp. Syst., **20**(4), pp. 1378–1389.

[15] Lefèvre, S., Sun, C., Bajcsy, R., and Laugier, C., 2014, "Comparison of Parametric and Non-Parametric Approaches for Vehicle Speed Prediction," *2014 American Control Conference (ACC)*, Institute of Electrical and Electronics Engineers Inc., pp. 3494–3499.

[16] Yang, H., Rakha, H., and Ala, M. V., 2017, "Eco-Cooperative Adaptive Cruise Control at Signalized Intersections Considering Queue Effects," IEEE Trans. Intell. Transp. Syst., **18**(6), pp. 1575–1585.

[17] Panwai, S., and Dia, H., 2005, "Comparative Evaluation of Microscopic Car-Following Behavior," IEEE Trans. Intell. Transp. Syst., **6**(3), pp. 314–325.

[18] Jiang, H., Hu, J., An, S., Wang, M., and Park, B. B., 2017, "Eco Approaching at an Isolated Signalized Intersection under Partially Connected and Automated Vehicles Environment," Transp. Res. Part C Emerg. Technol., **79**, pp. 290–307.

[19] Kamal, M. A. S., Hayakawa, T., and Imura, J., 2017, "Realization of Highly Anticipative Driving in a Partially Connected Vehicle Environment," *2017 IEEE 20th International Conference on Intelligent Transportation Systems (ITSC)*, IEEE, pp. 1–6.

[20] Lv, Y., Duan, Y., Kang, W., Li, Z., and Wang, F. Y., 2015, "Traffic Flow Prediction with Big Data: A Deep Learning Approach," IEEE Trans. Intell. Transp. Syst., **16**(2), pp. 865–873.

[21] Jiang, B., and Fei, Y., 2017, "Vehicle Speed Prediction by Two-Level Data Driven," IEEE Trans. Intell. Transp. Syst., **18**(7), pp. 1793–1801.

[22] Zhang, F., Xi, J., and Langari, R., 2017, "Real-Time Energy Management Strategy Based on Velocity Forecasts Using V2V and V2I Communications," IEEE Trans. Intell. Transp. Syst., **18**(2), pp. 416–430.

[23] Lighthill, M. J., and Whitham, G. B., 1955, "On Kinematic Waves II. A Theory of Traffic Flow on Long Crowded Roads," Proc. R. Soc. London. Ser. A. Math. Phys. Sci., **229**(1178), pp. 317–345.

[24] Richards, P. I., 1956, "Shock Waves on the Highway," Oper. Res.

[25] Payne, H. J., 1971, "Models of Freeway Traffic and Control," *Mathematical Models of Public Systems*, La Jolla, Calif., Simulation Councils, pp. 55–61.

[26] Aw, A., and Rascle, M., 2000, "Resurrection of 'Second Order' Models of Traffic Flow," SIAM J. Appl. Math., **60**(3), pp. 916–938.

[27] Wang, R., Work, D. B., and Sowers, R., 2014, "Multiple Model Particle Filter for Traffic Estimation and Incident Detection," IEEE Trans. Intell. Transp. Syst., **17**(12), pp. 1–10.

[28] Yuan, Y., Van Lint, J. W. C., Wilson, R. E., Van Wageningen-Kessels, F., and Hoogendoorn, S. P., 2012, "Real-Time Lagrangian Traffic State Estimator for Freeways," IEEE Trans. Intell. Transp. Syst., **13**(1), pp. 59–70.

[29] Asadi, B., and Vahidi, A., 2011, "Predictive Cruise Control: Utilizing Upcoming

Traffic Signal Information for Improving Fuel Economy and Reducing Trip Time," IEEE Trans. Control Syst. Technol., **19**(3), pp. 707–714.

[30] Rios-Torres, J., and Malikopoulos, A. A., 2017, "Automated and Cooperative Vehicle Merging at Highway On-Ramps," IEEE Trans. Intell. Transp. Syst., **18**(4), pp. 780–789.

[31] Ross, I. M., and Karpenko, M., 2012, "A Review of Pseudospectral Optimal Control: From Theory to Flight," Annu. Rev. Control, **36**(2), pp. 182–197.

[32] Gill, P. E., Murray, W., and Saunders, M. A., 2002, "SNOPT: An SQP Algorithm for Large-Scale Constrained Optimization," SIAM J. Optim., **12**(4), pp. 979–1006.

[33] Biegler, L. T., and Zavala, V. M., 2009, "Large-Scale Nonlinear Programming Using IPOPT: An Integrating Framework for Enterprise-Wide Dynamic Optimization," Comput. Chem. Eng., **33**(3), pp. 575–582.

[34] Büskens, C., and Wassel, D., 2012, "The ESA NLP Solver WORHP," Springer, pp. 85–110.

[35] Byrd, R. H., Nocedal, J., and Waltz, R. A., 2006, "Knitro: An Integrated Package for Nonlinear Optimization," Springer, pp. 35–59.

[36] Garg, D., Patterson, M., Hager, W. W., Rao, A. V., Benson, D. A., and Huntington, G. T., 2010, "A Unified Framework for the Numerical Solution of Optimal Control Problems Using Pseudospectral Methods," Automatica, **46**(11), pp. 1843–1851.

[37] Hartl, R. F., Sethi, S. P., and Vickson, R. G., 1995, "A Survey of the Maximum Principles for Optimal Control Problems with State Constraints," SIAM Rev., **37**(2), pp. 181–218.

[38] Ge, J. I., Avedisov, S. S., He, C. R., Qin, W. B., Sadeghpour, M., and Orosz, G., 2018, "Experimental Validation of Connected Automated Vehicle Design among Human-Driven Vehicles," Transp. Res. Part C Emerg. Technol., **91**, pp. 335–352.

[39] Hao, P., Wu, G., Boriboonsomsin, K., and Barth, M. J., 2019, "Eco-Approach and Departure (EAD) Application for Actuated Signals in Real-World Traffic," IEEE

Trans. Intell. Transp. Syst., **20**(1), pp. 30–40.

[40] Wang, M., Daamen, W., Hoogendoorn, S. P., and van Arem, B., 2014, "Rolling Horizon Control Framework for Driver Assistance Systems. Part I: Mathematical Formulation and Non-Cooperative Systems," Transp. Res. Part C Emerg. Technol., **40**, pp. 271–289.

[41] HomChaudhuri, B., Lin, R., and Pisu, P., 2016, "Hierarchical Control Strategies for Energy Management of Connected Hybrid Electric Vehicles in Urban Roads," Transp. Res. Part C Emerg. Technol., **62**, pp. 70–86.

[42] Guo, Y., Ma, J., Xiong, C., Li, X., Zhou, F., and Hao, W., 2019, "Joint Optimization of Vehicle Trajectories and Intersection Controllers with Connected Automated Vehicles: Combined Dynamic Programming and Shooting Heuristic Approach," Transp. Res. Part C Emerg. Technol., **98**, pp. 54–72.

[43] Li, M., Wu, X., He, X., Yu, G., and Wang, Y., 2018, "An Eco-Driving System for Electric Vehicles with Signal Control under V2X Environment," Transp. Res. Part C, **93**, pp. 335–350.

[44] Filipi, Z., Fathy, H., Hagena, J., Knafl, A., Ahlawat, R., Liu, J., Jung, D., Assanis, D., Peng, H., and Stein, J., 2006, "Engine-in-the-Loop Testing for Evaluating Hybrid Propulsion Concepts and Transient Emissions - HMMWV Case Study," SAE Tech. Pap.

[45] Hagena, J. R., Filipi, Z., and Assanis, D. N., 2006, "Transient Diesel Emissions: Analysis of Engine Operation During a Tip-In," SAE Tech. Pap.

[46] Hong, S., Assanis, D. N., and Wooldrige, M., 2002, "Multi-Dimensional Modeling of NO and Soot Emissions with Detailed Chemistry and Mixing in a Direct Injection Natural Gas Engine," SAE Tech. Pap.

[47] Patterson, M. A., Kong, S.-C., Hampson, G. J., and Reitz, R. D., 1994, "Modeling the Effects of Fuel Injection Characteristics on Diesel Engine Soot and NOx Emissions," SAE Tech. Pap.

[48] Feng, Y., Yu, C., Xu, S., Liu, H. X., and Peng, H., 2018, "An Augmented Reality Environment for Connected and Automated Vehicle Testing and Evaluation," *Transportation Research Board 97th Annual Meeting 18-04810*.

[49] Ma, J., Zhou, F., Huang, Z., Melson, C. L., James, R., and Zhang, X., 2018, "Hardware-In-The-Loop Testing Of Connected And Automated Vehicle Applications: A Use Case For Queue-Aware Signalized Intersection Approach And Departure," *Transportation Research Board 97th Annual Meeting 18-05431*.

[50] Hu, J., Shao, Y., Sun, Z., and Bared, J., 2017, "Integrated Vehicle and Powertrain Optimization for Passenger Vehicles with Vehicle-Infrastructure Communication," Transp. Res. Part C Emerg. Technol., **79**, pp. 85–102.

[51] Shao, Y., and Sun, Z., 2019, "Optimal Vehicle Speed and Gear Position Control for Connected and Autonomous Vehicles," *2019 American Control Conference (ACC)*, IEEE.

[52] Shao, Y., and Sun, Z., 2017, "Robust Eco-Cooperative Adaptive Cruise Control with Gear Shifting," *2017 American Control Conference (ACC)*, IEEE, pp. 4958–4963.

[53] Shao, Y., and Sun, Z., "Optimal Speed Control For A Connected And Autonomous Electric Vehicle Considering Battery Aging And Regenerative Braking Limits," *ASME 2019 Dynamic Systems and Control Conference, DSCC 2019-9075*.

[54] Shao, Y., Mohd Zulkefli, M. A., Sun, Z., and Huang, P., 2019, "Evaluating Connected and Autonomous Vehicles Using a Hardware-in-the-Loop Testbed and a Living Lab," Transp. Res. Part C Emerg. Technol., **102**, pp. 121–135.

[55] Mohd Zulkefli, M. A., Mukherjee, P., Sun, Z., Zheng, J., Liu, H. X., and Huang, P., 2017, "Hardware-in-the-Loop Testbed for Evaluating Connected Vehicle Applications," Transp. Res. Part C Emerg. Technol., **78**, pp. 50–62.

[56] Malikopoulos, A. A., and Zhao, L., 2019, "A Closed-Form Analytical Solution for Optimal Coordination of Connected and Automated Vehicles," *2019 American*

*Control Conference (ACC)*, pp. 3599–3604.

[57] Borek, J., Groelke, B., Earnhardt, C., and Vermillion, C., 2019, "Optimal Control of Heavy-Duty Trucks in Urban Environments Through Fused Model Predictive Control and Adaptive Cruise Control - IEEE Conference Publication," *2019 American Control Conference (ACC)*.

[58] Deng, J., Gagliardi, D., and Re, L., 2019, "Microscopic Driving Behavior Modelling at Highway Entrances Using Bayesian Network," *2019 American Control Conference (ACC)*.

[59] Bae, S., Kim, Y., Guanetti, J., Borrelli, F., and Moura, S., 2019, "Design and Implementation of Ecological Adaptive Cruise Control for Autonomous Driving with Communication to Traffic Lights - IEEE Conference Publication," *2019 American Control Conference (ACC)*.

[60] HomChaudhuri, B., and Pisu, P., 2019, "A Control Strategy for Driver Specific Driver Assistant System to Improve Fuel Economy of Connected Vehicles in Urban Roads - IEEE Conference Publication," *2019 American Control Conference (ACC)*.

[61] Yuan, Y., Van Lint, J. W. C., Wilson, R. E., Van Wageningen-Kessels, F., and Hoogendoorn, S. P., 2012, "Real-Time Lagrangian Traffic State Estimator for Freeways," IEEE Trans. Intell. Transp. Syst., **13**(1), pp. 59–70.

[62] Wang, Y., and Papageorgiou, M., 2005, "Real-Time Freeway Traffic State Estimation Based on Extended Kalman Filter: A General Approach," Transp. Res. Part B Methodol., **39**(2), pp. 141–167.

[63] Zhang, H. M. M., 2002, "A Non-Equilibrium Traffic Model Devoid of Gas-like Behavior," Transp. Res. Part B Methodol., **36**(3), pp. 275–290.

[64] Greenberg, J. M., 2002, "Extensions and Amplifications of a Traffic Model of Aw and Rascle," SIAM J. Appl. Math., **62**(3), pp. 729–745.

[65] Mammar, S., Lebacque, J.-P., and Salem, H. H., 2009, "Riemann Problem

Resolution and Godunov Scheme for the Aw-Rascle-Zhang Model," Transp. Sci., **43**(4), pp. 531–545.

[66] Greenberg, J. M., 2004, "Congestion Redux," SIAM J. Appl. Math., **64**(4), pp. 1175–1185.

[67] Fan, S., Herty, M., and Seibold, B., 2013, "Comparative Model Accuracy of a Data-Fitted Generalized Aw-Rascle-Zhang Model," Networks Heterog. Media, **9**(2), pp. 239–268.

[68] Rosales, R. R., Kasimov, A. R., Flynn, M. R., and Seibold, B., 2013, "Constructing Set-Valued Fundamental Diagrams from Jamiton Solutions in Second Order Traffic Models," Networks Heterog. Media, **8**(3), pp. 745–772.

[69] Toro, E. F., 2009, *Riemann Solvers and Numerical Methods for Fluid Dynamics: A Practical Introduction*, Springer.

[70] Helbing, D., and Treiber, M., 1999, "Numerical Simulation of Macroscopic Traffic Equations," Comput. Sci. Eng., **1**(5), pp. 89–98.

[71] Simon, D., 2006, *Optimal State Estimation: Kalman, H∞, and Nonlinear Approaches*, John Wiley & Sons, Inc.

[72] Wan, E. A., and Van Der Merwe, R., 2000, "The Unscented Kalman Filter for Nonlinear Estimation," *IEEE 2000 Adaptive Systems for Signal Processing, Communications, and Control Symposium*, pp. 153–158.

[73] He, C. R., Maurer, H., and Orosz, G., 2016, "Fuel Consumption Optimization of Heavy-Duty Vehicles With Grade, Wind, and Traffic Information," J. Comput. Nonlinear Dyn., **11**(6), p. 061011.

[74] He, C. R., Qin, W. B., Ozay, N., and Orosz, G., 2017, "Optimal Gear Shift Schedule Design for Automated Vehicles: Hybrid System Based Analytical Approach," IEEE Trans. Control Syst. Technol., **26**(6), pp. 1–13.

[75] Bengea, S., Uthaichana, K., Žefran, M., and DeCarlo, R., 2010, "Optimal Control of Switching Systems via Embedding into Continuous Optimal Control Problem,"

*The Control Systems Handbook, Second Edition*, pp. 31.1–31.23.

[76] Sager, S., Kirches, C., and Bock, H. G., 2008, "Fast Solution of Periodic Optimal Control Problems in Automobile Test-Driving with Gear Shifts," Proc. IEEE Conf. Decis. Control, pp. 1563–1568.

[77] Chen, H., Guo, L., Ding, H., Li, Y., and Gao, B., 2019, "Real-Time Predictive Cruise Control for Eco-Driving Taking into Account Traffic Constraints," IEEE Trans. Intell. Transp. Syst., **20**(8), pp. 2858–2868.

[78] Xu, S., Li, S. E., Zhang, X., Cheng, B., and Peng, H., 2015, "Fuel-Optimal Cruising Strategy for Road Vehicles with Step-Gear Mechanical Transmission," IEEE Trans. Intell. Transp. Syst., **16**(6), pp. 3496–3507.

[79] Li, S. E., Xu, S., Huang, X., Cheng, B., and Peng, H., 2015, "Eco-Departure of Connected Vehicles with V2X Communication at Signalized Intersections," IEEE Trans. Veh. Technol., **64**(12), pp. 5439–5449.

[80] Shaikh, M. S., and Caines, P. E., 2007, "On the Hybrid Optimal Control Problem: Theory and Algorithms," IEEE Trans. Automat. Contr., **52**(9), pp. 1587–1603.

[81] Riedinger, P., lung, C., and Kratz, F., 2003, "An Optimal Control Approach for Hybrid Systems," Eur. J. Control, **9**(5), pp. 449–458.

[82] Passenberg, B., and Stursberg, O., 2009, "Graph Search for Optimizing the Discrete Location Sequence in Hybrid Optimal Control," IFAC Proc. Vol., **42**(17), pp. 304–309.

[83] Achterberg, T., 2009, "SCIP: Solving Constraint Integer Programs," Math. Program. Comput., **1**(1), pp. 1–41.

[84] Tawarmalani, M., and Sahinidis, N. V., 2005, "A Polyhedral Branch-and-Cut Approach to Global Optimization," Math. Program., **103**(2), pp. 225–249.

[85] Belotti, P., Kirches, C., Leyffer, S., Linderoth, J., Luedtke, J., and Mahajan, A., 2013, "Mixed-Integer Nonlinear Optimization," Acta Numer., **22**(2013), pp. 1–131.

[86] Gurobi Optimization, L., 2018, “Gurobi Optimizer Reference Manual.”

[87] IBM ILOG CPLEX, 2018, “IBM Ilog CPLEX V12.6.1: User’s Manual for CPLEX.”

[88] “FICO® Xpress Optimization” [Online]. Available: https://www.fico.com/en/products/fico-xpress-optimization. [Accessed: 05-Jul-2019].

[89] Ross, I. M., and Fahroo, F., 2004, “Legendre Pseudospectral Approximations of Optimal Control Problems,” Springer, pp. 327–342.

[90] Rao, A. V., 2009, “A Survey of Numerical Methods for Optimal Control,” Adv. Astronaut. Sci., **135**(1), pp. 497–528.

[91] Bulmer, M. G., 1979, *Principles of Statistics*, Courier Corporation.

[92] Liberti, L., and Pantelides, C. C., 2006, “An Exact Reformulation Algorithm for Large Nonconvex NLPs Involving Bilinear Terms,” J. Glob. Optim., **36**(2), pp. 161–189.

[93] Bemporad, A., and Morari, M., 1999, “Control of Systems Integrating Logic, Dynamics, and Constraints,” Automatica, **35**(3), pp. 407–427.

[94] Beale, E. M. L., and Tomlin, J. A., 1970, “Special Facilities in a General Mathematical Programming System for Non-Convex Problems Using Ordered Sets of Variables,” Oper. Res., **69**, pp. 447–454.

[95] de Oliveira, N. M. C., and Biegler, L. T., 1994, “Constraint Handing and Stability Properties of Model-Predictive Control,” AIChE J., **40**(7), pp. 1138–1155.

[96] Elnagar, G., Kazemi, M. A., and Razzaghi, M., 1995, “The Pseudospectral Legendre Method for Discretizing Optimal Control Problems,” IEEE Trans. Automat. Contr., **40**(10), pp. 1793–1796.

[97] Darby, C., Hager, W. W., and Rao, A. V., 2011, “An Hp-Adaptive Pseudospectral Method for Solving Optimal Control Problems Christopher,” Optim. Control Appl. Methods, **32**, pp. 476–502.

[98] Herber, D. R., 2015, “Basic Implementation of Multiple-Interval Pseudospectral Methods to Solve Optimal Control Problems,” Tech. Rep.

[99] Mittelmann, H. D., 2018, “Benchmarks For Optimization Software” [Online]. Available: http://plato.asu.edu/bench.html.

[100] Ma, J., Hu, J., Leslie, E., Zhou, F., and Huang, Z., 2018, “Eco-Drive Experiment on Rolling Terrain for Fuel Consumption Optimization Summary Report (No. FHWA-HRT-18-037),” Fed. Highw. Adm. U.S. Dep. Transp., p. 49.

[101] Wang, Y., and Sun, Z., 2015, “Dynamic Analysis and Multivariable Transient Control of the Power-Split Hybrid Powertrain,” IEEE/ASME Trans. Mechatronics, **20**(6), pp. 3085–3097.

[102] Liu, J., and Peng, H., 2008, “Modeling and Control of a Power-Split Hybrid Vehicle,” IEEE Trans. Control Syst. Technol., **16**(6), pp. 1242–1251.

[103] Serrao, L., Onori, S., and Rizzoni, G., 2011, “A Comparative Analysis of Energy Management Strategies for Hybrid Electric Vehicles,” J. Dyn. Syst. Meas. Control, **133**(3), p. 031012.

[104] Musardo, C., Rizzoni, G., Guezennec, Y., and Staccia, B., 2005, “A-ECMS: An Adaptive Algorithm for Hybrid Electric Vehicle Energy Management,” Eur. J. Control, **11**(4–5), pp. 509–524.

[105] Mohd Zulkefli, M. A., Zheng, J., Sun, Z., Liu, H. X., Mohd Zulkefli, M. A., Zheng, J., Sun, Z., and Liu, H. X., 2014, “Hybrid Powertrain Optimization with Trajectory Prediction Based on Inter-Vehicle-Communication and Vehicle-Infrastructure-Integration,” Transp. Res. Part C Emerg. Technol., **45**, pp. 41–63.

[106] Kim, N., Cha, S., and Peng, H., 2011, “Optimal Control of Hybrid Electric Vehicles Based on Pontryagin’s Minimum Principle,” IEEE Trans. Control Syst. Technol., **19**(5), pp. 1279–1287.

[107] Lot, R., and Evangelou, S. A., 2013, “Green Driving Optimization of a Series

Hybrid Electric Vehicle," *52nd IEEE Conference on Decision and Control*, IEEE, pp. 2200–2207.

[108] Luo, Y., Li, S., Zhang, S., Qin, Z., and Li, K., 2017, "Green Light Optimal Speed Advisory for Hybrid Electric Vehicles," Mech. Syst. Signal Process., **87**, pp. 30–44.

[109] Wahl, H.-G., Bauer, K.-L., Gauterin, F., and Holzapfel, M., 2013, "A Real-Time Capable Enhanced Dynamic Programming Approach for Predictive Optimal Cruise Control in Hybrid Electric Vehicles," *16th International IEEE Conference on Intelligent Transportation Systems (ITSC 2013)*, IEEE, pp. 1662–1667.

[110] Vajedi, M., and Azad, N. L., 2016, "Ecological Adaptive Cruise Controller for Plug-In Hybrid Electric Vehicles Using Nonlinear Model Predictive Control," IEEE Trans. Intell. Transp. Syst., **17**(1), pp. 113–122.

[111] Park, S., and Rakha, H., 2006, "Energy and Environmental Impacts of Roadway Grades," Transp. Res. Rec., **1987**, pp. 148–160.

[112] Boriboonsomsin, K., and Barth, M., 2010, "Impacts of Road Grade on Fuel Consumption and Carbon Dioxide Emissions Evidenced by Use of Advanced Navigation Systems," Transp. Res. Rec., **2139**, pp. 21–30.

[113] Kirk, D. E., 1970, *Optimal Control Theory; an Introduction*, Prentice-Hall.

[114] Hoogendoorn, S., Hoogendoorn, R., Wang, M., and Daamen, W., 2013, "Modeling Driver, Driver Support, and Cooperative Systems with Dynamic Optimal Control," Transp. Res. Rec., **2316**, pp. 20–30.

[115] Wang, Y., Zhang, H., and Sun, Z., 2013, "Optimal Control of the Transient Emissions and the Fuel Efficiency of a Diesel Hybrid Electric Vehicle," Proc. Inst. Mech. Eng. Part D J. Automob. Eng., **227**(11), pp. 1546–1561.

[116] AASHTO, 2004, "A Policy On Geometric Design Of Highways And Street," Highw. Des. Man.

[117] FHWA, 2014, *Standard Specifications for Construction of Roads and Bridges on*

*Federal Highway Projects FP-14*.

[118] National Coordination Office for Space-Based Positioning,, Navigation, and T., "GPS Accuracy" [Online]. Available: https://www.gps.gov/systems/gps/performance/accuracy/. [Accessed: 03-Jan-2016].

[119] Wang, Y., Sun, Z., and Stelson, K. A., 2011, "Modeling, Control, and Experimental Validation of a Transient Hydrostatic Dynamometer," IEEE Trans. Control Syst. Technol., **19**(6), pp. 1578–1586.

[120] Wu, X., He, X., Yu, G., Harmandayan, A., and Wang, Y., 2015, "Energy-Optimal Speed Control for Electric Vehicles on Signalized Arterials," IEEE Trans. Intell. Transp. Syst., **16**(5), pp. 2786–2796.

[121] He, X., and Wu, X., 2018, "Eco-Driving Advisory Strategies for a Platoon of Mixed Gasoline and Electric Vehicles in a Connected Vehicle System," Transp. Res. Part D, **63**, pp. 907–922.

[122] Sciarretta, A., Guezennec, Y., Serrao, L., Rizzoni, G., and Onori, S., 2014, "Optimal Energy Management of Hybrid Electric Vehicles Including Battery Aging," Proc. 2011 Am. Control Conf., (3), pp. 2125–2130.

[123] Shen, D., Karbowski, D. A., and Rousseau, A., 2019, "Highway Eco-Driving of an Electric Vehicle Based on Minimum Principle," *2018 IEEE Vehicle Power and Propulsion Conference (VPPC)*, IEEE, pp. 1–8.

[124] Barré, A., Deguilhem, B., Grolleau, S., Gérard, M., Suard, F., and Riu, D., 2013, "A Review on Lithium-Ion Battery Ageing Mechanisms and Estimations for Automotive Applications," J. Power Sources, **241**, pp. 680–689.

[125] Tang, L., Rizzoni, G., and Onori, S., 2015, "Energy Management Strategy for HEVs Including Battery Life Optimization," IEEE Trans. Transp. Electrif., **1**(3), pp. 211–222.

[126] Ebbesen, S., Elbert, P., and Guzzella, L., 2012, "Battery State-of-Health Perceptive

Energy Management for Hybrid Electric Vehicles," IEEE Trans. Veh. Technol., **61**(7), pp. 2893–2900.

[127] Hoke, A., Brissette, A., Smith, K., Pratt, A., and Maksimovic, D., 2014, "Accounting for Lithium-Ion Battery Degradation in Electric Vehicle Charging Optimization," IEEE J. Emerg. Sel. Top. Power Electron., **2**(3), pp. 691–700.

[128] Panagiotidis, M., Delagrammatikas, G., and Assanis, D., 2019, "Development and Use of a Regenerative Braking Model for a Parallel Hybrid Electric Vehicle," *SAE Technical Paper 2000-01-0995*.

[129] Heydari, S., Fajri, P., Lotfi, N., and Falahati, B., 2018, "Influencing Factors in Low Speed Regenerative Braking Performance of Electric Vehicles," 2018 IEEE Transp. Electrif. Conf. Expo, pp. 494–499.

[130] Ehsani, M., Gao, Y., and Emadi, A., 2010, *Modern Electric, Hybrid Electric, and Fuel Cell Vehicles : Fundamentals, Theory, and Design*, CRC Press.

[131] Argonne National Laboratory, "Autonomie," https://www.autonomie.net/.

[132] Hicks-Garner, J., Wang, J., Musser, J., Verbrugge, M., Finamore, P., Soukiazian, S., Tataria, H., Liu, P., and Sherman, E., 2010, "Cycle-Life Model for Graphite-LiFePO4 Cells," J. Power Sources, **196**(8), pp. 3942–3948.

[133] Serrao, L., Onori, S., Sciarretta, A., Guezennec, Y., and Rizzoni, G., "Optimal Energy Management of Hybrid Electric Vehicles Including Battery Aging," Proc. 2011 Am. Control Conf., (3), pp. 2125–2130.

[134] Shenberger, M. J., and Antanaitis, D., 2018, "Brake System Design for Dedicated BEV Architectures," *SAE Technical Paper 2018-01-1870*.

[135] Zhang, X., Mi, C. C., and Yin, C., 2014, "Active-Charging Based Powertrain Control in Series Hybrid Electric Vehicles for Efficiency Improvement and Battery Lifetime Extension," J. Power Sources, **245**, pp. 292–300.

[136] Eshani, M., Gao, Y., Gay, S., Emadi, A., Ehsani, M., Gao, Y., and Emadi, A., 2009, *Modern Electric, Hybrid Electric, and Fuel Cell Vehicles: Fundamentals, Theory,*

*and Design*.

[137] Lohse-Busch, H., Duoba, M., Rask, E., and Meyer, M., 2012, "Advanced Powertrain Research Facility AVTA Nissan Leaf Testing and Analysis," Argonne Natl. Lab.

[138] U.S. Environmental Protection Agency, "Where the Energy Goes: Electric Cars" [Online]. Available: https://www.fueleconomy.gov/feg/atv-ev.shtml. [Accessed: 01-Apr-2019].

[139] Ma, J., Hu, J., Leslie, E., Zhou, F., Huang, P., and Bared, J., 2019, "An Eco-Drive Experiment on Rolling Terrains for Fuel Consumption Optimization with Connected Automated Vehicles," Transp. Res. Part C Emerg. Technol., **100**, pp. 125–141.

[140] General Motors, 2012, "2013 Cadillac Srx Specifications" [Online]. Available: https://media.cadillac.com/media/us/en/cadillac/vehicles/srx/2013.tab1.html. [Accessed: 14-Aug-2018].

[141] Liu, H. X., Wenteng, M., Hu, H., Wu, X., and Yu, G., 2008, "SMART-SIGNAL: Systematic Monitoring of Arterial Road Traffic Signals," IEEE Conf. Intell. Transp. Syst. Proceedings, ITSC, pp. 1061–1066.

[142] SAE, 2016, "Dedicated Short Range Communications (DSRC) Message Set Dictionary," SAE Stand. J2735.

[143] Ben-Tal, A., El Ghaoui, L., and Nemirovski, A., 2009, *Robust Optimization*, Princeton University Press.

[144] Savari Inc., 2017, "Road-Side-Unit" [Online]. Available: http://savari.net/technology/road-side-unit/. [Accessed: 17-Apr-2018].

[145] MnGeo: Minnesota Geospatial Information Office, "LiDAR Elevation Data for Minnesota" [Online]. Available: http://www.mngeo.state.mn.us/chouse/elevation/lidar.html. [Accessed: 29-Nov-2018].

[146] Oo, Y. L., Shao, Y., and Sun, Z., 2019, "Evaluating Fuel Economy of Connected and Autonomous Vehicles under Different Traffic Factors," *Transportation Research Board 98th Annual Meeting 19-05828*.

[147] Wang, Y., 2014, "Design, Control and Energy Optimization of a Rapid-Prototyping Hybrid Powertrain Research Platform," University of Minnesota, Ph.D. dissertation.